Precise absolute and relative navigation in Medium-Earth Orbits by means of Global Navigation Satellite Systems and Inter-Satellite Links

Álvaro Guindal Martínez

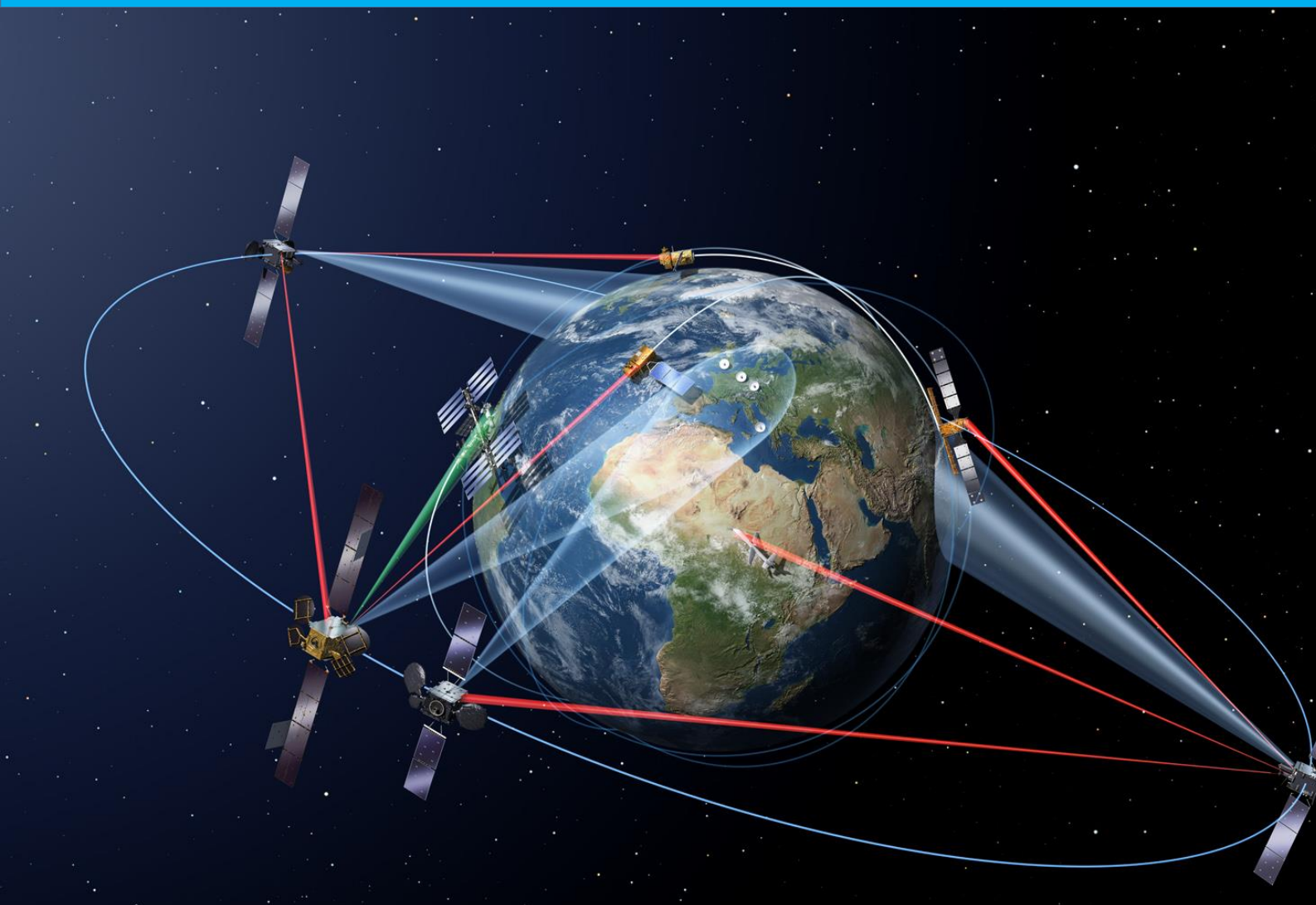

TU Delft

gmv

Precise absolute and relative navigation in Medium-Earth Orbits by means of Global Navigation Satellite Systems and Inter-Satellite Links

By

Alvaro Guindal Martinez

in partial fulfilment of the requirements for the degree of

Master of Sciences
in Aerospace Engineering

at the Delft University of Technology,
to be defended publicly on Friday March 27, 2020 at 9:30 AM.

Supervisor:	Dr. Ir. J.A.A. van den IJssel	
Thesis committee:	Dr. Ir. W. van der Wal,	TU Delft
	Dr. Ir. J.A.A. van den Ijssel,	TU Delft
	Dr. J. Guo,	TU Delft
	MSc. J. Fernández Sánchez,	GMV

Student: *Álvaro Guindal Martínez (4728319)*

Cover image: *Property of the European Space Agency (ESA)*

An electronic version of this thesis is available at http://repository.tudelft.nl/.

TU Delft

gmv INNOVATING SOLUTIONS

This page is intentionally left blank

Preface and Acknowledgements

This document is the result of a hard work 10-month period conducted at the Flight Dynamics and Operations (FDO) department of GMV at its headquarters in Madrid, Spain. The Master Thesis has been based in the growing field of POD, focusing in finding the limits and challenges of relative navigation in MEO orbits by means of ISL and GNSS observations. It also represents the last requirement to graduate from the MSc Aerospace Engineering programme at the Delft University of Technology.

Throughout this long path many people have offered and given me help and I would like to leave in writing my gratitude to each and every single one of them. First, I would like to express my deepest gratitude to my thesis supervisor at GMV, Jaime Fernandez. From the moment he gave me the opportunity to work on such a cutting-edge research topic to the final steps of the way, his support, help and valuable feedback have been key to my learning process and vital to the outcome of this thesis. Second, I would also like to express my profound gratitude to my supervisor back at the Aerospace Faculty of TU Delft, Jose van den IJssel. Her will to embark in this challenging project alongside Jaime and myself, as well as her continued monitoring and support have been of great value to me. Third, I would like to thank all my friends and especially Clara for being there in the hardest points of the way, because their affection and support have always made me carry on. Finally, I would like to thank my family and especially my parents, María José and Francisco, for always letting me make my own choices and pursue my own dreams, representing the role models that I look up to.

Álvaro Guindal Martínez
Madrid, February 2020

Abstract

The first close-up image of a black hole has been taken recently by means of a network of high-resolution telescopes situated all around the globe, also known as Event Horizon Telescope (EHT). In that regard, this Master Thesis reviews the feasibility of establishing accurate inter-satellite baselines in a two-satellite constellation of satellites placed in co-planar Medium Earth Orbits (MEO) equipped with telescopes to, amongst other applications, allow performing Very Long Baseline Interferometry (VLBI) on celestial bodies such as the supermassive black hole in the centre of our galaxy. As proven in LEO Earth-observation missions such as the Sentinels, a 3D accuracy in the absolute orbit solution of several centimetres might be achieved in post-processing when working with GNSS code and phase observations (Fernandez and Femenias, 2018). Such level of inaccuracies in the absolute orbit solution are likely to translate in the same order of magnitude to the relative positioning solution. Since the high precision standards to perform VLBI would not be met, the use of inter-satellite links in addition to GNSS tracking are assessed in this research trying to explore their main challenges and limitations.

Regarding the workflow of this study, first a thorough analysis of the visibility conditions from the GPS and Galileo constellations has been performed for the pair of MEO-placed satellites. The results have shown that the receiver antennas need to adapt a nadir orientation to maximize the number of visibility contacts from mentioned GNSS constellations. A nominal zenith-oriented receiver antenna has proven to experience a worsening of the visibility conditions with respect to what can generally be expected in LEO-placed satellites due to their proximity in altitude to the orbital regime of the GNSS constellations. Second, an assessment on the impact of different error sources in the absolute orbit accuracy has been conducted for the pair of satellites. The sensitivity analysis comprises errors that derive from realistic uncertainties in the geopotential model, GNSS orbits and clocks, satellites' solar radiation pressure model, centre of mass and antenna reference point. The results have shown that the error sources that most affect the accuracy of the absolute orbit solution are disturbance aligned with the velocity component in both centre of mass of the satellites and reference point of the receiver antennas.

Furthermore, to achieve the high standards of relative navigation, optical ISL observations with micro-meter precision level were employed. This precision level was determined by the limits of the employed software tool, as the state-of-the-art precision of these measurements is at the nano-metre level. Due to the 1D nature of the ISL observation, it has been found that they cannot be processed alone and require the GNSS code and phase observations to be processed along with them. In terms of the general workflow of this thesis, a first precise a-priori orbit of the satellites is determined with the help of code and phase GNSS observations, to be used as the starting point in the relative POD. In these processes, the system architecture of the inter-satellite ranging system has been assumed to be two-way to rule out the errors that derive from the non-synchronization of the satellites' clocks. It was also key to estimate constant sets of piece-wise empirical accelerations in the along-track component for constant time intervals to help fit the very precise ISL observations. The relative POD results have shown that the shorter the distance between the satellites, the higher the precision of the relative orbit solution in radial and along-track components, ultimately being limited by the precision of the ISL observations. The fact that the satellites are placed in co-planar orbits makes the cross-track component not be visible and probably yield conditioning problems to the LSQ matrix that result in the convergence to different local minimums. Therefore, the impact of angular separations ranging from 1 to 10 degrees on the relative POD accuracy is also investigated. The most promising results come from the case in which the relative distance between the MEO-placed satellites is low (1,000km) and an angular separation in the orbital planes of 10 degrees has been induced. In that case, the relative orbit solution is improved in all components (radial, along-track and cross-track) and placed in the few millimetre level.

Table of contents

List of figures

List of tables

Acronyms

AIUB	Astronomical Institute University of Bern
ARNS	Aeronautical Radio-Navigation Services
C_{AL}	Albedo coefficient
CDMA	Code Division Multiple Access
CHAMP	Challenging Minisatellite Payload
CLO	Close Scenario
CNES	Centre National d'Études Spatiales
CODE	Center for Orbit Determination in Europe
CR	Solar Radiation Pressure coefficient
DOI	Digital Object Identifier
ECI	Earth-Centered Inertial
EHT	Event Horizon Telescope
EIGEN	European Improved Gravity model of the Earth by New techniques
EIRP	Effective (or Equivalent) Isotropic Radiated Power
ERP	Earth Radiation Pressure
ERS	European Remote Sensing
ESA	European Space Agency
ESOC	European Space Operation Centre
FAR	Far scenario
FDMA	Frequency Division Multiple Access
FOC	Full Operatinal Capability
GAL	Galileo
GEO	Geostationary Orbit
GHOST	GPS High Precision Orbit Determination Software Tools
GIOVE	Galileo In-Orbit Validation Experimed
GLONASS	GLObalnaya NAvigatsionnaya Sputnikovaya Sistema (GLObal NAvigation SAtellite System)
GNSS	Global Navigation Satellite System
GPS	Global Positioning System
GPST	GPS Time
GRACE	Gravity Recovery And Climate Experiment
GRACE-FO	Gravity Recovery And Climate Experiment Follow-On
GRGS	Groupe de Recherche de Géodésie Spatiale
HEO	High Eccentricity Orbit
ID	Identifier
IDS	International DORIS Service
IEEE	Institute of Electrical and Electronics Engineers
IERS	International Earth Rotation Service
IGS	International GNSS Service
IGSO	Inclined Geo-Synchronous Orbit
IOV	In-Orbit Validation
IRI	International Reference Ionosphere
ISBN	International Standard Book Number
ISL	Inter Satellite Link
ITT	Invitation To Tender
JPL	Jet Propulsion Laboratory
LEO	Low Earth Orbit
LISA	Laser Interferometer Space Antenna
LSQ	Least Square Estimator
MEO	Medium Earth Orbit
MID	MID scenario
NAPEOS	NAvigation Package for Earth Orbiting Satellites
NASA	National Aeronautics and Space Agency
PCV	Phase Centre Variations
PNT	Position, Navigation and Timing

POD	Precise Orbit Determination
QZSS	Quasi-Zenith Satellite System
RAAN	Right Ascension of the Ascending Node
RINEX	Receiver INdependent EXchange
RMS	Root Mean Square
RNSS	Regional Navigation Satellite System
RQ	Research Question
RSSI	Received Signal Strength Indicator
RSW	Radial, along-track, cross-track reference body frame
RTN	Normal, tangential, normal reference body frame
SAR	Synthetic Aperture Radar
SI	Système Internationale d'unités (International System of units)
SLR	Satellite Laser Ranging
SNR	Signal-to-Noise Ratio
SPP	Single Point Positioning
SRP	Solar Radiation Pressure
SSV	Space Service Volume
STD	Standard Deviation
STM	State Transition Matrix
TAI	Temps Atomique Internationale
TN	Technical Note
TSV	Terrestrial Service Volume
TT	Terrestrial Time
US	United States
USA	United States of America
UTC	Coordinated Universal Time
VLBI	Very Long Baseline Interferometry

Symbols

N_{L_f}	Integer ambiguity
$k_{f_{rcv}}$	Instrumental delays receiver antenna
Φ_f	Apparent range (carrier phase)
P_{nm}	Associated Lagrange polynomials
k_f^{sat}	Instrumental delays transmit antenna
$\ddot{r}$	Acceleration
$\alpha_f STEC$	Ionospheric delays
ε_f	GNSS observables noise
λ_f	Signal frequency
A	Observations partials matrix
A_R	Cross-sectional area
c	Speed of light
C/N_0	Signal-to-noise ratio
C_{nm}, S_{nm}	Unnormalized geopotential coefficients
C_R	Solar Radiation Pressure coefficient
$\mathbf{e_R}$, $\mathbf{e_S}$, $\mathbf{e_W}$	Orientation of body-frame in ECI J2000
F	Force
G/T	Receive antenna gain-to-noise temperature
G_{RX}	Directivity gain receiver antenna
G_{TX}	Directivity gain transmit antenna
H	Observations partials with respect to state vector matrix
I	Signal intensity
IA	Solar intensity
J	Jacobian matrix
k_B	Boltzmann constant
k_n	Love number
L	Free-space losses
m	Mass
M	Earth's mass
M_f	Multipath effect
$\mathbf{P}_0$	Parameters initial covariance matrix
P_{TX}	Antenna transmit power
R	Earth radius
R_{AU}	One astronomical unit
R_f	Apparent range
RSW	Body-fixed reference frame components
S	Sensitivity matrix
T_r	Tropospheric delays
t_r	Transmit time
t_t	Receiving time
U	Earth's gravity potential
W	Observations covariance matrix
$\mathbf{X}_0$	Initial state vector
XYZ	ECI J2000 reference frame components
z	Observations vector
ΔS_{atm}	Atmospheric delays
$\Delta \boldsymbol{X}$	Update of state vector
ρ	Geometric range
$\omega(z)$	Laser spot size
$\boldsymbol{\varepsilon}$	Observations residuals vector
$\boldsymbol{\phi}$	State transition matrix

1

Introduction

This thesis is enclosed in the topic of Precise Orbit Determination (POD) which has been a growing field in the past couple of decades. Earth-observation missions with high orbit requirements have been the main reason for the mentioned growth of POD in the space industry. For instance, Synthetic Aperture Radar (SAR) missions provide day-and-night imagery of Earth thanks to the use of instruments that can work independently of light and heat, for which they need to meet demanding requirements in terms of orbit accuracy. Such orbit solutions are obtained with the aid of Global Navigation Satellite Systems (GNSS), since they provide measurements that allow to reconstruct an orbit with high fidelity. Additionally, and even though it is not as common as for LEO satellites, the orbit determination process with the help of GNSS observations can also be applied to satellites placed in higher orbital regimes such as MEO (Rim et Schutz, 2002). Furthermore, these orbit determination processes are considered as absolute because even though there are more than one target satellite, the GNSS observations are processed independently from one satellite to another.

On the other hand, when range measurements between the satellites in a constellation are used, the POD process is considered to be relative. In such scenario, one of the satellites in the constellation is taken as reference and the orbit solution of the rest of them are estimated with respect to the reference trajectory. In that regard, precise relative navigation is a subject that has been little explored in the field especially when the constellation of satellites are placed in higher orbital regimes as MEO. In the LEO regime, there are already existing missions such as GRACE and GRACE-Follow On that make use of these very precise range measurements between satellites to estimate physical parameters like Earth's geopotential or gravitational. However, such range measurements have generally not been used in a POD process in order to improve their relative positioning accuracy. Therefore, this study explores the use of GNSS tracking only and along with precise inter-satellite link observations to obtain accurate orbit solutions in both absolute and relative terms for a constellation of MEO-placed satellites. Particularly, the core of the research is focused in trying to give light to the challenges and limitations that arise performing relative positioning in high orbital regimes.

Regarding the structure of this chapter, the motivation of this research is presented first along with the state-of-the-art in relative navigation and their beforehand known existing problems. After that, the configuration of the constellation of MEO-placed satellites will be explained in detail, referring to both the orbit conditions and their specific physical properties. Additionally, the research's aim and a set of research questions to which answer is meant to be given throughout this thesis, are also reported. Finally, the outline of the thesis is presented, in which the contents of the remaining chapters are briefly described.

1.1 Problem statement

Being able to establish very precise inter-satellite links between satellites in the MEO regime would open the door to new missions in the scientific world. Those missions could be destined to observe Earth and its surroundings (i.e. Lunar Exploration) or could be focused in exploring outer space. In that regard, there are many physical phenomena from which our knowledge is quite limited. This is the case of the super massive black hole located in the center of our galaxy. Even though the event horizon of the black hole has already been imaged from a network of ground-based telescopes known as EHT (Doeleman, 2017), a higher resolution imaging is required to advance in the study of these objects. To achieve so, ESA has proposed to perform space-based Very Long Baseline Interferometry (VLBI) on these celestial bodies for which purpose really accurate knowledge of relative distance between satellites is required. The agency is in need of examining which are the current limits of relative navigation at medium orbital regimes to assess the feasibility of any potential mission and the different challenges that arise from it (ESTEC, 2018).

The vast majority of the constellation properties have been assumed to be the same and are in agreement with the ESA study conditions. They have all been summarized and presented in section 1.1.1 as well as a preliminary analysis of the evolution of the baseline between the satellites along time. It is important to know beforehand the range of values in which the relative distance will lie, to fully understand the magnitude of the problem.

As previously mentioned, there are already existing missions that make use of relative baselines between satellites to estimate different physical parameters. The conditions found in them are quite different from the ones found in the framework of this thesis but it is always good to review the current state-of-the art in the field to point out the new challenges to face. In that regard, in section 1.1.2 a small revision of the current techniques employed to describe the relative motion between satellites is given as well as the reasons why they cannot be applied to the MEO orbital regime. Moreover, the GRACE, GRACE-FO and LISA missions are described to fully understand their orbital conditions and mission objectives. In that regard, it is desired to give clarity to give fact that the objectives pursued in this thesis work are quite new to the field and that this research represents a step forward in exploring the limits of relative navigation in the MEO regime.

1.1.1 MEO-constellation properties

To replicate the conditions of the ESA study, the simulations carried out in the thesis will consider a constellation of 2 satellites placed in polar low-MEO orbits of 7,000 and 7,018km of altitude respectively. Such orbital conditions were translated into the corresponding set of initial state vectors and provided to us as shown below in Table 1-1. Please note that they are expressed in Keplerian elements and referenced to the epoch 01/01/2019 00:00:00 UTC.

Table 1-1. MEO constellation properties

	MEO-1	MEO-2
Semi-major axis (km)	13387	13369
Altitude (km)	7009	6991
Orbital period (hours)	4.28	4.27
Eccentricity	0	0
Inclination (deg)	90	90
RAAN (deg)	0	0
Argument of Perigee (deg)	0	0
True Anomaly (deg)	0	0
Attitude mode	Earth-pointing	Earth-pointing

Information about the physical properties of the satellites is not available from the ESA study, and therefore an assumption has to be made. In such a way, a basic cannonball box-wing model can be assumed for both satellites for which the values of area and solar radiation pressure coefficient have been sensibly chosen (Figure 1-1). Please note that the value of drag coefficient has not been listed in Table 1-2 because the drag force is considered negligible for the specified orbital conditions. Such statement follows from the literature found in Montenbruck et al (2000) and is further detailed in Chapter 4 of this document.

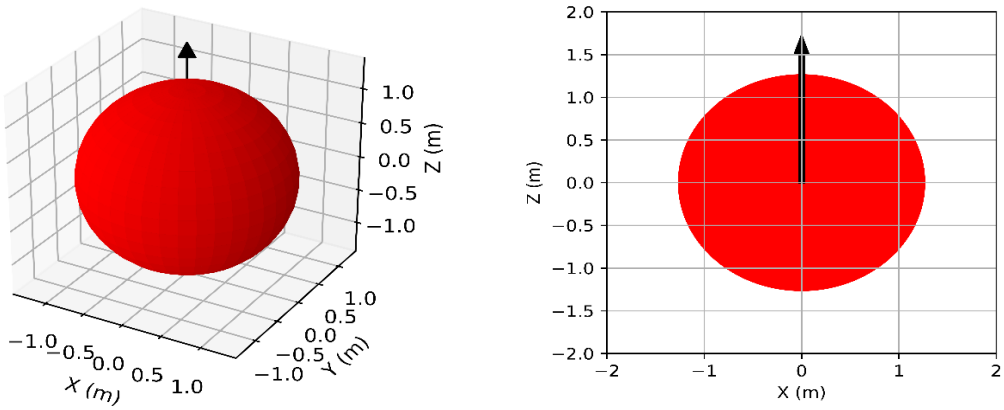

Figure 1-1. Cannonball model assumed for MEO-1 and MEO-2 satellites

Table 1-2. Physical properties of MEO-1 and MEO-2 satellites

Name	Value
Area [m^2]	5.0
Mass [kg]	1500
C_R [-]	1.0
C_{AL} [-]	1.0

Due to the fact that the baseline between the satellites plays a vital role in the relative navigation positioning accuracy, the initial state vectors of MEO-1 and MEO-2 satellites were propagated for a duration of 6 months to evaluate how the baseline changes with time. This preliminary analysis is mainly focused in determining the range in which the relative distance between the satellites lies and its behavior along time. Even though the list of perturbations considered for these simulations will be further explained in Chapter 4, they are shortly mentioned below.

- Earth potential (order and degree used: 120x120)
- Third body effect (Moon, Sun and all Solar System planets – Pluto included)
- Solar Radiation Pressure
- Solid and Ocean Tides (order and degree used: 30x30)
- Relativistic gravitation
- Albedo radiation

The results of the preliminary simulations are shown in Table 1-3 and summarized in Table 1-4 below. Please note that the results in the graph have been plotted in a logarithmic scale to better illustrate the rate of change of the distance along time that is not constant.

Table 1-3. Simulation settings

Initial propagation date	01-01-2019 00:00:00 UTC
Final propagation date	01-07-2019 00:00:00 UTC
Propagator	Multi-step 8^{th}-order Adams-Bashfort
Number of steps	720 steps/orbit
Output orbit file time step	30 s

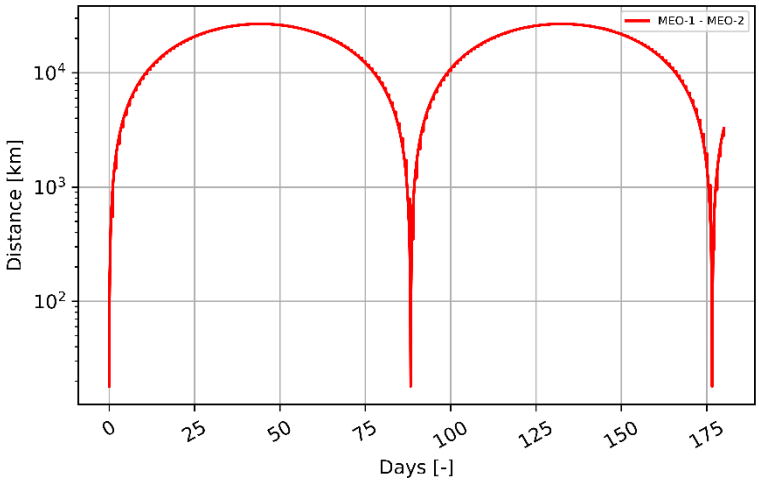

Figure 1-2. Evolution of the relative distance between the satellites

Table 1-4. Relative distance characteristics

Periodicity	176.6 days
Amplitude	26,753.668 km
Minimum distance	18 km

Due to the fact the range between the satellites is quite variable and it goes from 18 to 20,000km, different test case scenarios have been defined in that regard. In such a way, an assessment on how much does the relative distance between the satellites affect the accuracy of the relative positioning can be made. The selected dates are shown below in Table 1-5 and have been all taken from the same month (January) in which the distance already experiments a rapid increase from its minimum possible value to the maximum.

Table 1-5. Scenarios to be considered in terms of relative distance between the satellites

Case	Epoch	Relative Distance
Close	01/01/2019 12:00:00	~1000 km
Medium	11/01/2019 00:00:00	~11000 km
Far	26/01/2019 00:00:00	~22000 km

1.1.2 Relative navigation

One of the main challenges of working with a constellation of satellites is to be able to precisely predict the trajectory of any given satellite with respect to the satellite that is considered as reference (Jiang et al., 2007) (Figure 1-3). In that regard, there are a set of equations that are currently being used to define the relative motion of satellites in formation flying mode. They follow from the simplification of the general equations of motion of any Earth-orbiting satellite and applying a set of different assumptions. Generally, there are two main approaches to obtain simplified equations of the relative motion, depending on the set of assumptions taken.

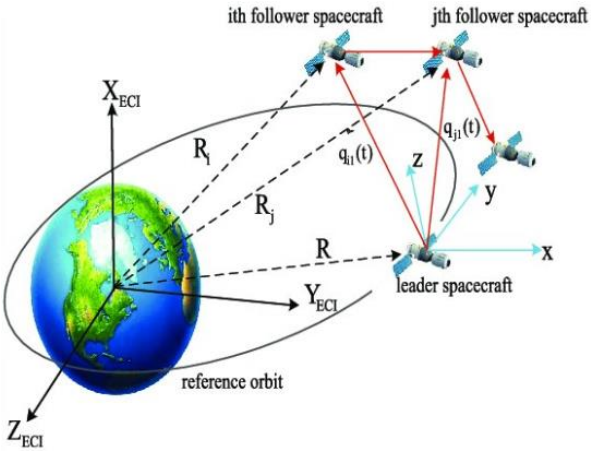

Figure 1-3. Graphic representation of a constellation of satellites in formation flying mode (Liu et al, 2018)

On one hand, Clohessy and Wiltshire linearized the Keplerian relative dynamics around a circular reference orbit, also known as Hill's equations (Lee, 2009). The reference satellite is assumed to be placed in a circular orbit meanwhile the remaining ones might be in either a circular or elliptical one. On the other hand, the equations have been linearized around an elliptical orbit assuming that the satellite is under the sole influence of the main gravitational field of the Earth and the second zonal harmonic (Dwidar et al., 2013). Both approaches assume that the satellites whose relative motion is to be described are placed in neighboring orbits (Lee, 2009). The fact that the satellites are assumed to be close to each other at all times allows, indeed, to linearize the equations of motion. Otherwise, the simplifications/assumptions taken to arrive to such analytical mathematical expressions of the relative motion are not representative of reality and cannot be applied.

The assumptions that can be taken when applying a relative POD process when the satellites are close to each other do not apply to this thesis work. The perturbations that model the motion of the satellites are assumed to be equal for small periods of time. In other words, the forces acting on the satellites cancel out with respect to each other which translates in the transition matrix being much more simplified. Nevertheless, for a constellation of satellites in formation flying configuration placed in low MEO of 7,000km high with a relative distance of thousands of kilometers, none of the approaches apply. In summary, the problem needs to be dealt with in a nominal way and no simplifications can be made in terms of their relative motion.

1.2 State-of-the-art

This section reviews the current status in the industry when it comes to the use of baseline measurements between satellites in a constellation. To do so, three missions are analyzed to understand the different functionalities of inter-satellite link ranging that are available in the industry nowadays.

1.2.1 BeiDou

Inter-satellite links are thought to be a key addition in order to achieve a modern global navigation satellite system (GNSS). Most GNSS constellations are planned to be equipped with inter-satellite technology (ISL), but currently the BeiDou-3 generation of satellites, that is expected to be operational in 2020, represents the only GNSS constellation in which this technology is to be used in the near future (Stetter et al., 2017), (Tang et al., 2016). Implementing an efficient communication and ranging system architecture by means of inter-satellite links connecting the different satellites that form the constellation is expected to be very beneficial. In the specific case of BeiDou, the autonomy gained by means of ISL will reduce the upcoming problematics of only counting with regional ground stations and monitoring systems and the maintenance costs will be lowered down considerably (Yang et al, 2019). Additionally, its navigation performance by means

of these ranging measurements between satellites has also been tested and is expected to be improved once the new generation is operational (Zhou et al., 2018).

When it comes to ranging, the method employed to estimate the distance between satellites will be a dual one-way ranging approach (both satellites emit a one-way signal). As will be explained more in detail in Chapter 3, one-way ranging is probably the less accurate approach when it comes to inter-satellite ranging. However, and since the ISL are used for communication purposes as well, the offset between the clocks of the receiving and transmitting satellites is included in the navigation message so that it can be taken into account for the range estimation along with the remaining error sources (Yang et al., 2017). Then, these dual one-way ranging observations will be processed in an orbit determination by means of a LSQ batch algorithm along with the ground observations for a 3-day arc. The addition of these inter-satellite observations has proven to attain an increase in the performance of the accuracy of the relative orbit solution of about 37 to 76% in signal-in-space range error (Yang et al., 2017).

1.2.2 GRACE & GRACE Follow-On

The Gravity Recovery and Climate Experiment (GRACE) mission has been in charge of studying the Earth's gravity field during the past 15 years (2002-2017) even though the initial designed duration was of only 5 years. As a continuation, the Gravity Recovery and Climate Experiment Follow-On (GRACE-FO) mission was launched in mid-2018 and it presents a near-identical hardware configuration to the original mission, but includes a new experimental instrument, an optical inter-satellite link (JPL, 2019).

Both missions consist of a constellation of two satellites in formation flying configuration whose relative distance is continuously monitored in order to detect the variations in the satellites distance that the Earth's gravitational field provokes as shown in Figure 1-4 (Heinzel, 2019). When there is a sudden change in the distribution of Earth's mass caused by the reduction of underground water or a set of mountains, the gravity field changes accordingly and so does the distance between the satellites. It is important to note that the distance between satellites is relatively small (200km) and that the distance variations are in the micron level, similar to the size of a blood cell (NASA, 2019). It is because of the ranging method employed, known as interferometry, that such small distance variations can be detected.

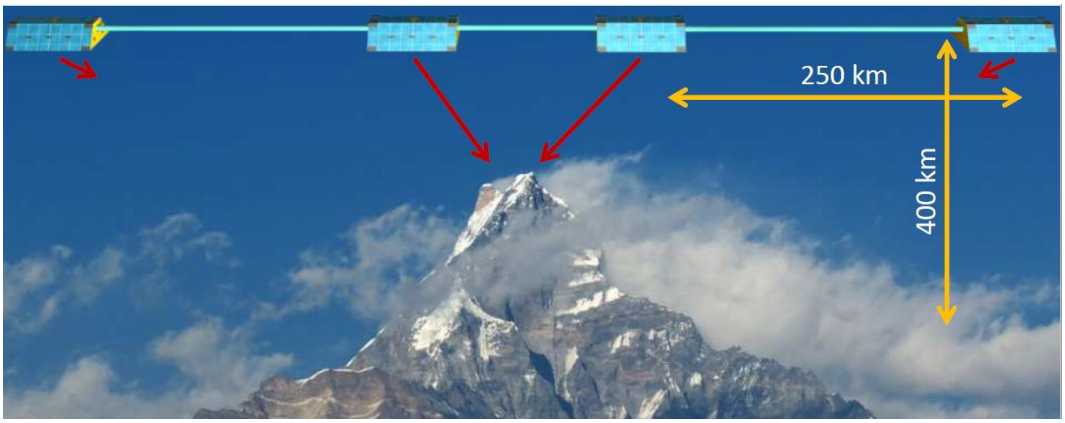

Figure 1-4. Basics of GRACE mission (Heinzel, 2019)

As can be noted, the similarities between the GRACE missions and this thesis study are quite low. First, the satellites are placed in LEO orbits and the relative distance between the satellites is regular at around 250km. On top of that, the baseline measurements are used for relative positioning, from which physical parameters are inferred. Thus, it is hard to take any of the configuration of these missions as reference for this research study since the conditions, even if inter-satellite ranging observations are used, are very unalike.

1.2.3 LISA

The Laser Interferometer Space Antenna (LISA) is a space-based wave observatory that has been proposed after the success of its previous validation mission, the LISA pathfinder mission. Its planned launch is in 2034 and it will consist of a constellation of 3 satellites placed in heliocentric orbits forming an equilateral triangle and separated by 5 million kilometers. The main challenge is to detect gravitational wave signatures that indicate distortions in the space-time. In order to do so, inter-satellite laser signals are transmitted back and forth in order to measure the variations in distance between the satellites (Danzmann, 2017). It is important to note that since the satellites are very far away from each other, the accuracy of the range estimations must be very high in order to obtain results that may be significant and useful for the greater purpose of the mission.

LISA intents to measure shifts in the relative position that are less than the diameter of a helium nucleus over a distance of a million miles – the change in distances caused by the gravitational waves are small (pm to nm) (NASA, 2019). Such high level of accuracy in distance shifts is obtained by means of an interferometric system that measures the differential optical path length modulation along the three sides of the triangular configuration defined by the satellites. The small distance variations caused by the gravitational waves can be distinguished because they are at mHz frequencies (1000 seconds timescale) (Danzmann, 2017).

In that regard, it was the LISA pathfinder mission that proved the high-accuracy of current inter-satellite link technologies. The long baseline conditions between the satellites expected in the LISA mission are in agreement with the conditions of the studied carried out in this thesis work. However, the LISA mission has not been launched yet and observations as well as results are therefore not available.

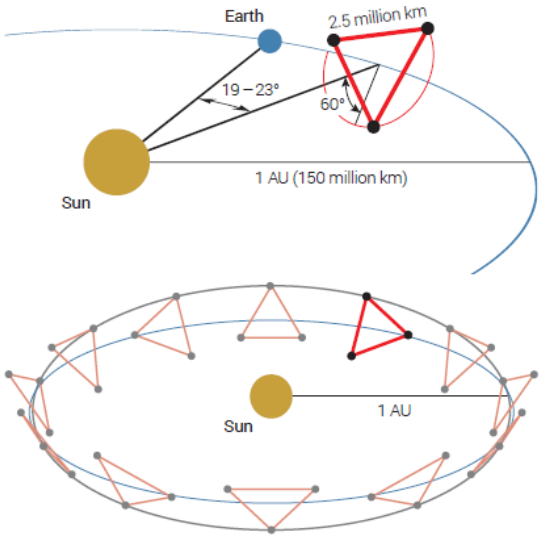

Figure 1-5. Depiction of the LISA Orbit (Danzmann, 2017)

1.3 Research proposal

In order to fully represent the proposal of the research, its main objective, a set of research questions and its framework have been presented below.

1.3.1 Research aim

This research is focused in exploring the challenges and limitations of performing relative positioning for a constellations of satellites in high orbital regimes. In that regard, the objective is to validate the hypothesis that the use of very precise inter-satellite links between a pair of MEO-

placed satellites actually improves their relative positioning in comparison with the levels of accuracy that can be achieved by means of GNSS observations only.

1.3.2 Research questions

A set of research questions in the framework of this thesis have been defined, to help identifying the most important areas of study and puts the focus on the specific goals to be achieved. They have been grouped in three main questions that have their corresponding sub-questions as they go more into detail.

RQ1 - What is the optimal antenna configuration for absolute POD for a MEO satellite using the GNSS constellations?

a. Taking into account GPS and Galileo constellations, is it good enough to assume a nominal zenith-pointing configuration or does a nadir-pointing scenario yield better results? The trade-off between both configurations should be done in terms of:
    i. Number of observations
    ii. Signal-to-noise ratio of the observations
b. Does taking into account the sides lobes of the emitter antenna of GPS/Gal satellites yield a higher number of observations? Do these observations obtained by means of the side lobes present a suitable signal-to-noise ratio?
c. If the nadir-pointing configuration is assumed, does the ionospheric delay modelling need to be updated to take into account the different path through the ionosphere?

RQ2 - What are the impacts on the accuracy of the absolute orbit solution when including realistic inaccuracies on the satellites' properties and uncertainties in the models as listed below? All these simulations are to be carried out with the inclusion of realistic noise in the observations

a. Uncertainties in the geopotential models
b. Inaccuracies in the cannonball model of the satellite
c. Uncertainties in the precise GNSS ephemeris and clocks
d. Imperfect knowledge of center of mass of satellites and antenna reference point

RQ3 - What is the impact on the relative orbit accuracy when the ISL range observations are processed along with GNSS tracking?

a. What are realistic ISL noise errors, and what is their impact on the relative POD?
b. What is the impact of the relative distance (1000km [close], 10,000km [mid-range] and 20000km [far away]) between the MEO-placed satellites?

1.4 Thesis outline

In order to give answer to the set of research questions, the relevant information has been structured in the following chapters. First, the theoretical information regarding the different GNSS constellations is presented. Then, an overview of the POD process is given. Special attention is put on the modelling of the dynamical perturbations and signal delays. Due to the big importance of relative navigation in this thesis work, a chapter is devoted to review the methodology of inter-satellite link ranging and the state-of-the-art limits of this technology. Due to the special orbit conditions in which the constellation of satellites is placed, a visibility study is performed to ensure the optimum configuration that maximizes the number of observations. Then, a set of realistic error sources are introduced in the absolute POD process step to assess their influence on the final orbit solution and whose absolute accuracy is within state-of-the-art limits. The next chapter is devoted to present the results of the POD process when including the inter-satellite measurements, focusing on the relative accuracy of the orbit solutions. Finally, there is a chapter

to summarize all conclusions drawn from the previous chapters and assess whether or not have the research questions been validated. Please note that all chapters in which results have been presented have a small subsection in which the software is validated.

2

Global Navigation Satellite Systems

Currently, there are various GNSS systems that provide global coverage for all types of users both terrestrial and airborne. Nevertheless, around 25 years ago the situation was much different and the global market was completely dominated by GPS, the American constellation (Bonnor, 2012). The Russian constellation GLONASS was developed almost in parallel to GPS but it initially thought to provide only regional coverage. As time went by and due to political motivations in order to gain independence from the USA in the field, other big economies in the world such as the European Union and China started to build their own GNSS systems. Consequently, the number of operational systems has currently grown up to four of them with the addition of Galileo (EU) and Beidou (China) that offer a wide variety of frequencies and signals. Furthermore, the increase in navigation capability also responds to the current rise of needs in positioning that many applications and ground-based users present (Someswar et al., 2013). The growth of Earth-observation missions with high orbit requirements has also motivated the creation of new GNSS systems apart from the already existing GPS.

Since the main capability of the GNSS systems is to provide coverage to all types of space and ground-based users, it is important to go through the different geometries and their specific characteristics. First of all, the Service Volume refers to the groups of regions in which a user of the GNSS systems may be found. It is mainly divided into two big sectors: Terrestrial and Space. On one hand, the Terrestrial Space Volume (TSV) refers to the users placed on Earth's surface and up to an altitude of 3,000 km. On the other hand, the Space Service Volume (SSV) comprises the range of orbits whose altitude lies in between 3,000 and 36,000km. Additionally, it is also divided into two main subregions: the one corresponding to medium altitudes (3,000km to 8,000km) and the one that covers the high and geosynchronous orbit altitudes (8,000 to 36,000km). All this information graphically is presented in Figure 2-1 left in which it can also be noted that the altitudes at which the GNSS systems are placed is generally at the 20,000km level.

Furthermore, to receive the signal of a GNSS satellite the user needs to be in sight. To be able to acquire the signals coming from the GNSS satellites, the ground stations or user satellites are equipped with antennas with a high aperture angle (generally around 150º in the direction of sight). The orientation of the receiving antenna is key to obtain a favorable geometry that allows as many connections as possible with the GNSS constellations. Depending on the region of the Space Volume in which the receiving satellite is placed, the optimum orientation of the GNSS receiver antenna may vary (Figure 2-1 right). The nominal antennas are zenith-oriented or, in other words, they look towards space. This configuration is quite suitable for ground-based stations located in the TSV and spacecraft located in the lower region of the SSV (LEO orbits and low MEO orbits).

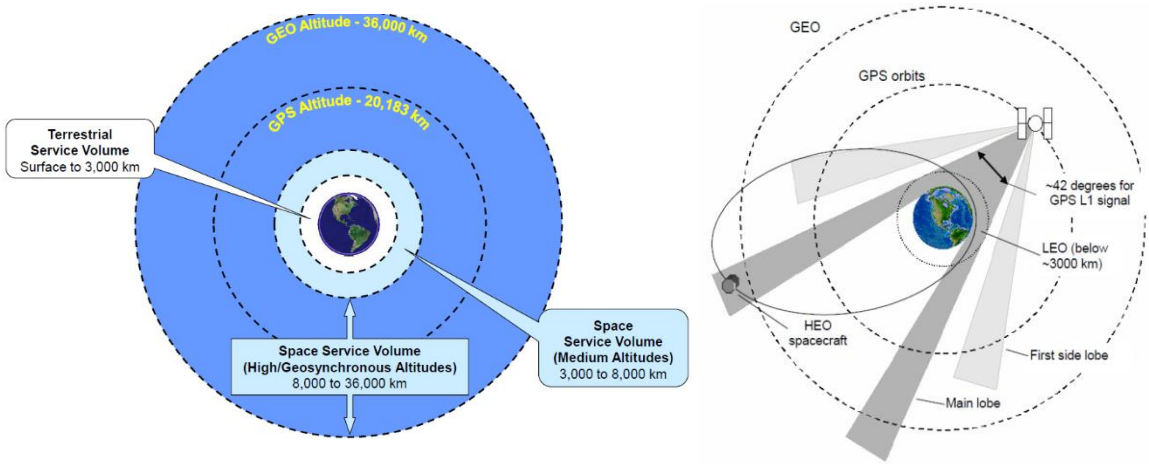

Figure 2-1. Space Service Volume (Bauer, 2015) (left), visibility geometries between GNSS and user satellites (right)

After having briefly introduced the history of the GNSS systems, section 2.1 is focused on presenting a small overview of the ones that are currently operational. Special attention is given to GPS and Galileo since they are the ones considered in the simulations, following the study requirements set by ESA. After that, in section 2.2 the GNSS signals are characterized to give the user an overview of how the range observations are calculated and which parameters play a role in such process. Additionally, the most important delays that affect the transmission of the signal are reviewed, especially applied to the specific geometry of the zenith and nadir-oriented case scenarios.

2.1 GNSS constellations

To provide ongoing world-wide positioning to any given user, GNSS satellites transmit navigation signals that are used to generate GNSS measurements, essential in the reconstruction of the trajectory of the user (Sanz, 2013). The transmission of these navigation signals is done through different bands of frequency that are particular to each of the constellations. The military signals are transmitted by means of different codes in the bands than the civilian ones. Additionally, it is important to note that almost all GNSS constellations (not BeiDou) are placed in nearly-circular orbits at altitudes of around 20,000km. Generally, they count a total number of around 25-32 satellites which are placed in different orbital planes so that there are at least 4 of them visible at any point of the Earth's surface at all times (United Nations, 2015). A small review of the main GNSS constellations is to be presented below to give the reader a glimpse of the similarities and differences of the various systems.

2.1.1 Global Positioning System (GPS)

GPS is the most used navigation system in the world. It is owned by the United States government and operated by the US Air Force. It currently presents a total of 32 satellites (31 in operation) distributed in 6 orbital planes (called A to F) at an approximate altitude of 20,200km with an inclination of 55° and separated by 60 degrees in longitude.

There are two GPS legacy code signals: the coarse/acquisition (C/A) transmitted in the carrier frequency of 1575.42MHz (L1) and the precision (P-) transmitted in the carrier frequencies of 1227.6 MHz (L2) as well as L1. The P-code signal is reserved for military use and is encrypted (Hegarty, 2012). It is important to bear in mind that the constellation is being updated quite often by the addition of new models of the satellites. Currently the operational satellites come from 3 different generations: Block IIR, Block IIR(M), Block IIF; the generation GPS III is in production and one satellite has already been launched. More information on the GPS constellation can be

found in Navipedia (2018) and Official US government GPS (2019) from which Table 2-1 found below has been based.

Table 2-1. Generations of GPS satellites (GPS, 2019)

	Legacy Satellites		Modernized Satellites		
	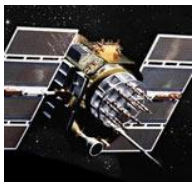	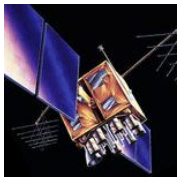	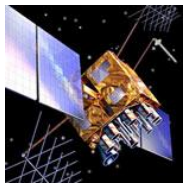	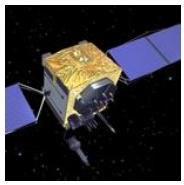	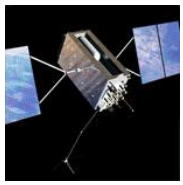
	Block IIA	**Block IIR**	**Block IIR(M)**	**Block IIF**	**GPS III**
	0 operational	12 operational	7 operational	12 operational	1 operational
Signals	- Civil users: C/A code on L1 - Military users: P(Y) code on L1 & L2	- Civil users: C/A code on L1 - Military users: P(Y) code on L1 & L2	- Civil users: C/A code on L1 & L2C on L2 - Military users: P(Y) code on L1 & L2, M code on L1 & L2	- Civil users: C/A code on L1, L2C on L2C & L5 - Military users: P(Y) code on L1 & L2, M code on L1 & L2	- Civil users: C/A code on L1, L2C on L2C, L5 & L1C on L1 - Military users: P(Y) code on L1 & L2, M code on L1 & L2
Design lifespan	7.5 years	7.5 years	7.5 years	12 years	15 years
Launching date	1990-1997	1997-2004	2005-2009	2010-2016	Started in 2019

2.1.2 Galileo

Galileo is a project supported by the European Union in an attempt to be independent from USA and Russia in terms of navigation system. It is currently being deployed in an attempt to be fully operational by 2020. At that stage, a total of 30 satellites will be available (24 in use and 6 redundant) at an altitude of 23,222km with an inclination of 56 degrees and distributed in 3 orbital planes separated by 120 degrees. As of now, 18 satellites are already in orbit and operational. The constellation will continue growing in the future with the addition of the FOC2 generation which will make the number of satellites grow up to 30 (including spares).

There are four frequency bands in which the navigation signals are transmitted. They are known as E5a (1176.45 MHz), E5b (1207.14 MHz), E6 (1278.75 MHz) and E1 (1575.42 MHz). They have all been allocated in the part of the spectrum globally reserved to radio-navigation services (RNSS), even though the E5 and E1 bands have also been included in the Aeronautical Radio-Navigation Services (ARNS) part of the spectrum (European Union, 2012 & 2019). All the information is summarized below in Table 2-2.

Table 2-2. Generations of Galileo satellites (Perez et al., 2015)

	Legacy	Current	
			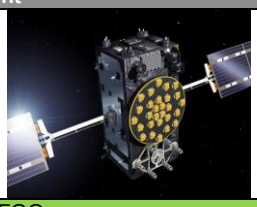
Name	GIOVE	IOV	FOC
	2 already retired	3 operational (1 not available)	19 operational (2 in non-operational orbit)
Navigation signal bands	E5a, E5b, E6 and E1	E5a, E5b, E6 and E1	E5a, E5b, E6 and E1
Launch	2005–2008	2011–2012	2014–Present
Lifespan	Over 27 months	12 years	12 years
Goal	Claim the allocated frequencies and testing	End-to-end validation of the Galileo service concept	Full operational validation and service performance.

2.1.3 GLONASS

The GLONASS constellation is operated by the Russian government and represents the second most used GNSS system in the world. Likewise GPS, it provides global coverage by means of 24 operational satellites placed in MEO orbits with an altitude of 19,130km, distributed in three different orbital planes separated by 120 degrees in longitude and with an inclination of 64.8° (Revnivykh, 2010)

Old GLONASS satellites (Glonass, Glonass-M) used Frequency Division Multiple Access (FDMA) which means that each of them communicates at slightly different frequencies. In particular, they would broadcast navigation signals in small modifications of two sub-bands of the L-band, known as L1 (1598-1605 MHz) and L2 (1242-1248 MHz). However, the new generations (Glonass-K1, Glonass-K2) use Code Division Multiple Access (CDMA) which means that they all transmit in the same frequency but with different code, likewise GPS. The sub-bands at which they transmit are L1 (1575 MHz), L2 (1248 MHz), L3 (1207 MHz) and L5 (1176 MHz) (Hegarty, 2012).

2.1.4 BeiDou

The BeiDou constellation is composed of satellites in MEO, GEO and IGSO (inclined Geosynchronous Orbit) orbits. The constellation started as a regional system back in 2012 with only 14 satellites evenly distributed in the orbits previously mentioned but its aim is to provide global coverage by 2020 with the help of 35 operational satellites. The altitude of the MEO satellites is 21,500km and the inclination of the IGSOs is 55 degrees. It is important to note that the satellites emit in 3 band frequencies (E2, E5B, E6) that overlap with the ones used by the Galileo satellites (Xie et Liu, 2013).

As explained in the state-of-the-art section of the introduction, it is important to stress that BeiDou is the only GNSS constellation to make use of ISL observations between its satellites to gain autonomy and not be as dependent on the ground-based stations. The BeiDou constellation represents the first case in which these very precise observables have been used in a POD process to improve the relative accuracy of the relative positioning in a constellation of satellites (Yang et al, 2019).

2.1.5 Miscellaneous

There are other GNSS systems that provide regional coverage to their respective regions. For instance, the Quasi Zenith Satellite System (QZSS) consists of a four-satellite constellation developed by the Japanese government that complements the coverage of the GPS constellation in the Asia-Oceania region (Zhang et al., 2018). The original idea was to place the satellites in corresponding GEO orbits so that they could stand still on top of the target region but they were finally located in quasi-zenith orbits (QZO) that have a much lower speed in the northern hemisphere (target region) than in the southern one.

Finally, NavIC stands for Navigation Indian Constellation and consists of a 7-satellite constellation that covers the Indian and surroundings region. It has been developed by the Indian government and there are plans in the near future to increase the number of satellites in operational mode and the total extension of the target region that the system covers (Ma et al., 2019).

2.2 GNSS observables

For high-precision POD of Earth-orbiting satellites, nowadays nearly all satellites rely on observations from GNSS constellations, especially GPS. It is possible to obtain measurements from ground-based stations such as radars, optical telescopes or laser ranging stations but their limited precision makes the obtained orbit solution to be not as good (Poore et al., 2016). Focusing on the type of observations that will be used in this thesis study to perform the absolute POD of the MEO satellites, they are known as pseudo-range and carrier phase observations. They are explained in more detail in section 2.2.1 below, but the main difference between them is the accuracy they provide for the orbit estimation process and how they are obtained. Once such differences have been presented and reviewed, in section 2.2.2 a small description of the different sources of delay that affect the transmission of the signal from the GNSS constellations to the user receiver satellites is given.

2.2.1 GNSS pseudo-range and carrier phase observables

The basic GPS observable used to determine the position of a given user is the travel time of a propagating signal between the phase centre of the emitter and receiver antennas. Assuming that the signal travels at the speed of light, an estimation of the range between both satellites can be easily obtained. The way to estimate the delta time of the signal travelling from one satellite to another is by means of a code that is generated by the GPS satellites and replicated in the receiver satellite. As depicted below in Figure 2-2, once the replicated code matches the generated one, the difference in time (ΔT) is recorded and multiplied by the speed of light to produce the so-called apparent range between the satellites.

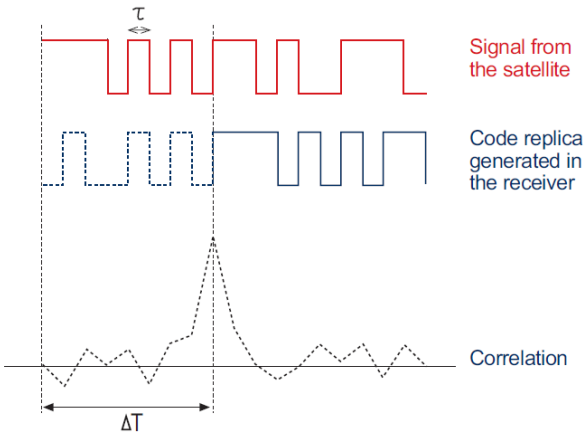

Figure 2-2. Signal travel time determination (Sanz et al., 2013)

However, this measurement only represents the apparent range between the satellites and not the true geometric one since it includes errors due to a diverse set of factors. The main one refers to the travelling time of the signal is obtained by means of the difference between two clocks in two different clock scales. A synchronization error in these clocks leads to a mis-estimation of the real range between the satellites. There are a number of other errors that also affect the travelling of the signal that are included below in Equation 2.1 (Sanz et al. 2013). They are reviewed in more detail in the following section.

$$R_{P_f} = \rho + c(dt_{rcv} - d_t^{sat}) + Tr + \alpha_f STEC + K_{P_f,rcv} - K_{P_f}^{sat} + M_{P_f} + \varepsilon_{P_f} \quad (2.1)$$

in which

- R_{P_f} is the apparent range between the satellites
- ρ represents the geometric range between the GNSS and user satellites [m]
- c is the speed of light [m/s]
- $dt_{rcv}\ and\ d_t^{sat}$ represent the clock offsets of the transmitter and receiver satellites in the GNSS time scale [s]

- Tr are the tropospheric delay errors [m]
- $\alpha_f STEC$ represents the ionospheric delay suffered by the signal in the frequency in which it has been transmitted [m]
- $K_{P_{f,rcv}}\ and\ K_{P_f}^{sat}$ represent the emitter and receiver instrumental delays [m]
- M_{P_f} refers to the multipath effects that cause the signal to travel more distance than it should nominally do [m]
- ε_{P_f} pseudorange noise [m]

It is important to note that depending on which frequency this signal is transmitted, the chip code will present a different longitude that generally lies in the [30, 293m] range for the GPS constellation. The error in the precision of these type of pseudodistances is placed at the 1% level of the longitude of the signal, which therefore translates in a [0.3, 3m] in the precision of this type of observables (Sanchez Sobrino, 2010).

There is also another type of observable known as carrier phase whose precision is much higher (noise at mm level) than the code observables in the estimation of the apparent range between the satellites. These measurements represent the difference in phase of the received signal from the GNSS satellite and the internally generated phase by the oscillator of the receiver. They are ambiguous by a total number of wavelengths (λN), a value that changes every time the connection between the GNSS and user satellite is lost and then re-established. The short wavelength presented in these signals (19cm (1575.42MHz), 24cm (1227.60MHz)) allows for the high precision in the apparent range estimation. These observables are obtained as shown in Equation 2.2 and Figure 2-3 provides a graphical representation of the concept of these measurements (Sanz et al., 2013).

$$\Phi_{L_f} = \rho + c(dt_{rcv} - d_t^{sat}) + Tr - \alpha_f STEC + k_{L_f,rcv} - k_{L_f}^{sat} + \lambda_{L_f} N_{L_f} + \lambda_{L_f}\omega + \mathrm{m_{L_f}} + \varepsilon_{L_f} \qquad (2.2)$$

in which the new terms are

- λ_{L_f} represents the frequency of the signal [Hz]
- N_{L_f} is known as integer ambiguity
- $k_{L_f,rcv}\ and\ k_{L_f}^{sat}$ correspond to receiver and GNSS satellite instrumental delays at the corresponding frequency [m]
- $\lambda_{L_f}\omega$ estimates the wind-up of the signal due to circular polarization [m]
- $\mathrm{m_{L_f}}$ carrier phase multipath [m]
- ε_{L_f} carrier phase noise [m]

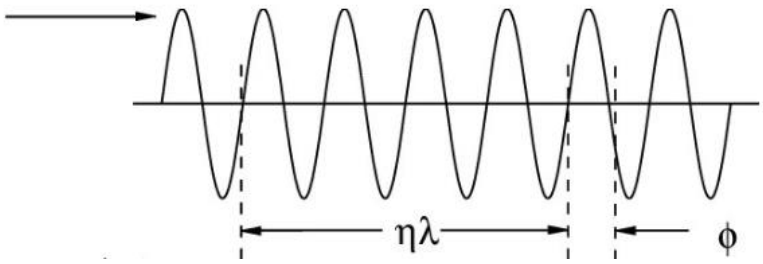

Figure 2-3. Carrier-phase observables (How et Lawson, 1996)

2.2.2 Signal delays

The travelling of a signal from a GNSS satellite to the target spacecraft is affected by a set of delays that need to be known as accurately as possible. If they are well-modelled or eliminated (in case of ionospheric delay), a good correction of the range observations can be obtained.

Tropospheric effects

First of all, the troposphere is the lowest region of the atmosphere that goes from the surface of Earth up to an average 13km. Due to the low range of altitudes that is considered as troposphere, generally the only signals that are considered as affected by the troposphere are the space-to-ground or space-to-space ones in which there is radio occultation (Sokolovskiy, 2003). Since previously mentioned in this report, the user satellites in this case will be placed in MEO orbits. For nominal zenith pointing antennas in MEO, GNSS tracking is not affected by tropospheric effects.

If proven in the visibility analysis (Chapter 5) that the optimum antenna configuration for the MEO satellites to maximize the observations is the nadir-pointing one, the signal will travel very close to Earth's surface and could even cross the troposphere. In order to avoid considering such delays, a grazing altitude of at least 100km has been set to filter out the signals that at some point in their travel path enter in the troposphere.

Phase wind-up

This delay is caused by the electromagnetic nature of circularly polarized waves, such as the ones used in GNSS signals. It is important to note that it only affects the high-accuracy phase measurement observations and not the pseudo-range observables (Sanz et al., 2013). The modelling of this effect can be done by means of the expressions found in Wu et al. (1993). In such a way, the carrier-phase measurements can be corrected to eliminate this source of error.

Antenna Phase Center Offset & Variation

Generally, the phase center of an antenna does not correspond with its geometric center. In fact, this phase center position is affected by not only the corresponding elevation and azimuth but also by the frequency in which the signal is to be transmitted (Teunissen and Montenbruck, 2017). There are simple models in which it is assumed that the offset only takes place in the vertical axis of the antenna but in order to obtain high-accuracy observations, more complex models for both GNSS and transmitter antennas need to be applied (available in IGS PCV website).

Instrumental delays

These delay sources englobe hardware such as cables, antennas and different filters equipped in both GNSS satellites and receivers. These instrumental delays need to be considered since they affect all types of observables, both code and phase (Sanz et al., 2013) (Teunissen and Montenbruck, 2017). The GNSS transmitter antennas and ground stations maps are available at IGS website (IGS, 2020), and the LEO PCV maps are generally estimated in flight. In this project it is just considered for the transmitting satellite (GNSS) since in the receiver it is assumed to be absorbed in the receiver clock estimates.

Ionospheric delay

The ionosphere is the region of the atmosphere that extends from around 80 to over 2,000km. In this region of the atmosphere, and as its name indicates, ionized particles may be found as a result of solar X-rays, cosmic rays and energetic particles. Generally, it is divided into different layers that are identified as D, E, F1 and F2 from bottom to top (Jin et al., 2014). As described in Teunissen and Montenbruck (2017), the ionosphere does not present a homogeneous density of electrons throughout its different layers. The fact that the electron density is not constant makes the refractive index of the medium to vary as well. Consequently, the signal will suffer a repetitive bending which makes the path longer in comparison with the nominal case that is a straight line. Since the ionosphere is a dispersive medium it is dependent on frequency. Hence, a dual-frequency combination is generally used to eliminate the first-order effects which represent the 99% of the total error. The higher order effects whose contribution is the remaining 1%, present a delay with an order of magnitude of a few mm (Zelmas, 2011).

However, when a perturbed signal has only been transferred in one frequency, the GRAPHIC combination of pseudo-range and carrier-phase observations to eliminate the first-order ionosphere errors. However, the ionosphere delay can also be corrected by means of a model or estimating it. In that regard, there are already existing models such as NeQuick (Leitinger et al., 2005) and Klobuchar (Gao et Liu, 2002) that have been developed to serve such purposes. Their only main drawback for the purpose of this thesis work is that in all those models the signal is assumed to follow a path similar to the one depicted in Figure 2-4 below. Following that geometry, it can be noticed that it is assumed that the signal traverses the ionosphere in a vertical way. In other words, the signal is going down the different layers of the ionosphere and getting closer to Earth's surface at all times (no matter whether the receiver is ground-based or airborne). Nevertheless, this approach is only possible when the receiver is adopting a zenith-looking orientation which means that the antenna is directed towards free-space. Thus, the signal comes directly from the higher orbital regime in which the GNSS satellites are placed.

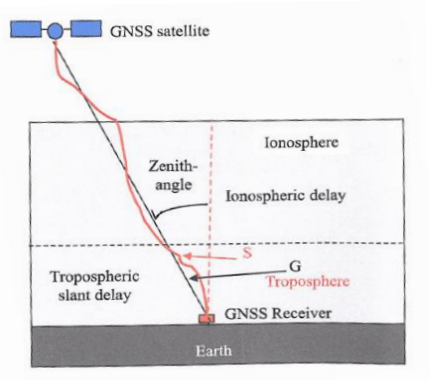

Figure 2-4. Delay caused by the ionosphere to a GNSS signal following a nominal path

However, if due to the need to optimize the visibility of GNSS, the receiver antenna adapts a nadir-looking orientation the path followed by the signal is much different. As can be seen from Figure 2-5 below, it gets gradually closer to Earth, traversing at some point layers in the ionosphere. Yet, once a minimum is achieved, the signal continues its path towards the target satellite, diverging from Earth's surface and going up in the different ionosphere layers. Please note that even though the receiver satellite in this case is listed as LEO, the very same physical phenomena if it was placed in higher orbital regimes like MEO.

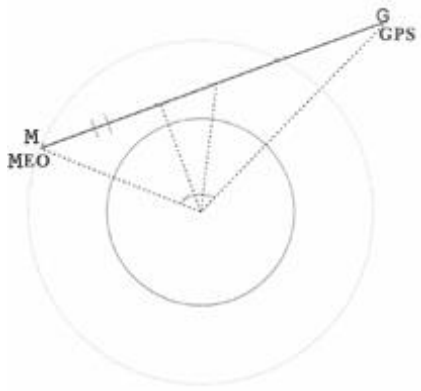

Figure 2-5. Nadir-pointing geometry

The problem with this geometry is that the already existing ionosphere models do not provide with a precise estimation of the delay for a signal that travels past Earth's ionosphere transversally. In general terms, efforts in research should be devoted to develop the most complete ionospheric model to be able to simulate and estimate in a representative way the delays found under these orbit conditions.

3

Inter-Satellite Links

Relative orbit determination refers to the process in which the trajectory of a satellite is estimated with respect to the reference orbit of another one. To obtain a very precise relative positioning, observations expressing the range between the satellites with high accuracy need to be available. In that regard, there are current state-of-the-art measurements known as inter-satellite links that have proven to provide ranges between satellites in a constellation up to the nanometer level (Amanor, 2018). Nevertheless, their main drawback is that they are one-dimensional (1D) and do not provide information of the distance between the satellites in all orbit components. For this reason, it is very important to figure out how to include them in the overall POD process to be able to take advantage of their very precise information of the relative positioning of both satellites. Additionally, these links can also be used for communication purposes as it is expected to happen with the new generation of satellites of the BeiDou constellation, to help gain more autonomous navigation and reduce dependence on ground stations (Yang et al, 2019) (Shah, 2017); Galileo 2nd generation is also studying the inclusion of inter-satellite links (Kur and Kalarus, 2018). For the means of this project, the ISL observations will only be used to find an improvement in the relative orbit accuracy in post-processing.

This chapter focuses on presenting an overview of the architecture of the ISL system that will be considered for the means of this project, for which ESA did not mention a preferred method yet. Special attention is given to the reasons behind the choices made amongst the different set of possibilities available. This generally concerns the selection of an optical signal (laser) over a radio one and also that a two-way system architecture was chosen instead of a one-way approach. Furthermore, the different properties that characterize the propagation of an optical signal in free-space are reviewed, along with the variables that play an important role in the process.

3.1 General ranging methods

There are different approaches to estimate the range between a pair of cooperative satellites in a constellation (Alawieh, 2016). Indeed, and as it can be seen in Figure 3-1, at the most upper level the methods can be divided into direct and indirect. As presented in the introduction of this chapter, the nature of inter-satellite links remains on the fact of a signal being transmitted from one satellite to another, which can be used for ranging and/or communication purposes. In such a way, it can be deduced that no indirect ranging method could actually be referred to as inter-satellite link. Consequently, the possible methods left are divided into one-way and two-way ranging. The main difference between the two options relies on whether or not does the signal

travel from the transmitter to the emitter satellite end-to-end (one-way) or if it the signal goes back to the transmitter satellite after having been reflected in the receiver one (two-way).

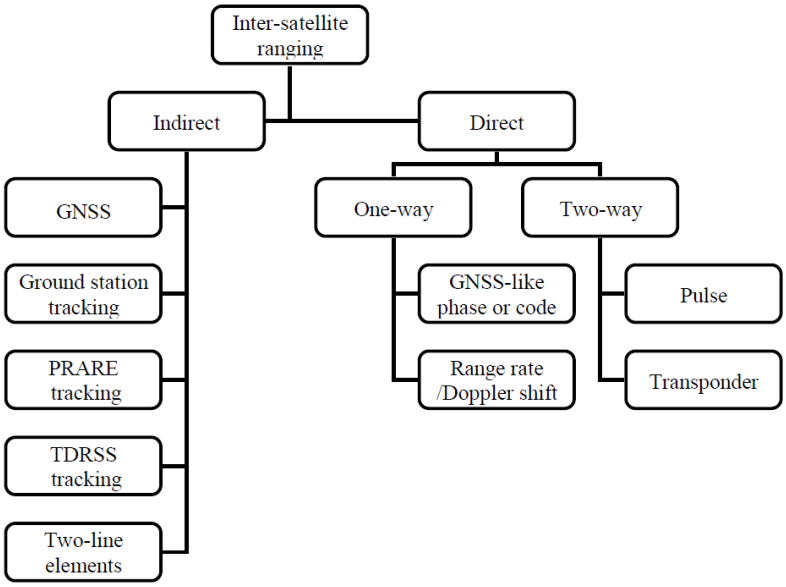

Figure 3-1. Ranging options (Sun et al., 2010)

Within the one-way and two-way approaches, there are a different set of possibilities that include GNSS-like phase and code, Doppler shift or pulse methods amongst others. Some of these approaches are only available if the signal is transmitted in a specific band frequency. In this regard, there are two main possibilities when it comes to the signal transmission as stated in Sun (2010): the optical (3 PHz – 3 THz) and radio band frequencies (300 kHz – 3 Hz).

Radio-frequency signals represent a more consolidated technology for communications rather than for ranging purposes. The huge experience that exists for radio transmission in space-to-ground scenarios makes it an easier approach for space-to-space information transmissions as well (Raineri, 2016). One of the main advantages of the radio-frequency systems is that they present omnidirectional coverage, which makes it a really good fit for communications purposes. However, the long wavelength of the radio-band frequency makes this type of signals not completely suitable to achieve very precise ranging measurements. Contrarily, the optical band-frequency presents a range of wavelengths that go from 100nm to 100μm. These are quite low values in the electromagnetic spectrum, in fact only surpassed by the ionizing radiation which englobes X-rays, Gamma rays and ultraviolet radiation. Because of that, state-of-the-art missions that make use of inter-satellite links for scientific purposes actually use optical laser range measurements to monitor the change of relative distance between the satellites (Heinzel, 2019) (Zhou et al., 2018). As briefly explained in Chapter 1, this is the case of the LISA mission in which changes in the relative distance of satellites separated by several millions of kilometers are monitored to the nanometer level, which is only achievable by the use very precise observables in the infrared optical band frequency (ESA LISA, 2019).

Taking all this information into account, it is safe to say that an optical systems seems to be the best fit for the needs of this project. In this regard, in the following section the one-way and two-way ranging methods that make use of optical laser signals are reviewed, stressing their best advantages and reasoning the selected option used in the simulations of this thesis study.

3.2 One-way and two-way range configurations

Regarding the one-way and two-way methods shown in Figure 3-1 above, not all of them present the same level of precision in the ranging observable due to the different methodology used in each of the proposed options. For instance, the Received Signal Strength Indicator (RSSI) approach converts the difference in power between the transmitted and received signal to estimate the range between the corresponding satellites (Doppler shift method in Figure 3-1). This method is widely used because of its simplicity, but its accuracy is compromised when the distance to be estimated is high due to a weak signal-to-noise ratio (Alawieh, 2016). Thus, if modelling very precise observation like ISL are, it is not an advisable method to employ.

It is also possible to apply a GNSS-like method to estimate the relative distance between two satellites in a constellation. In this case, the method would be one-way ranging and it would involve a signal travelling from one satellite (master spacecraft in Figure 3-2) to another in which the time it takes to reach the receiver satellite (remote spacecraft in Figure 3-2) would be multiplied by the speed of light to estimate the range between the satellites. The advantage this approach presents relies on the fact that an optical signal with a much lower wavelength is used in this case. Therefore, and even though the methodology concept is equal to the one applied for code observables in the GNSS constellations (shown in Chapter 2), the accuracy of the measurement in this case would be higher. The main disadvantage of this methodology is the need to achieve a very high synchronization of the clocks of both satellites in order to obtain precise ranging estimations. Nevertheless, if proven possible to have almost identical synchronized clocks, this one-way ranging should produce very high quality distance observations. The mathematical formulation to apply this ranging approach is expressed below in Equation 3.1.

$$R_t\,(t_t) = c(t_r - t_t) \tag{3.1}$$

where

t_t	transmission time in the transmitter clock scale [s]
t_r	receiving time in the receiver clock scale [s]
c	speed of light [m/s]
R_t	apparent range at transmission time [m]

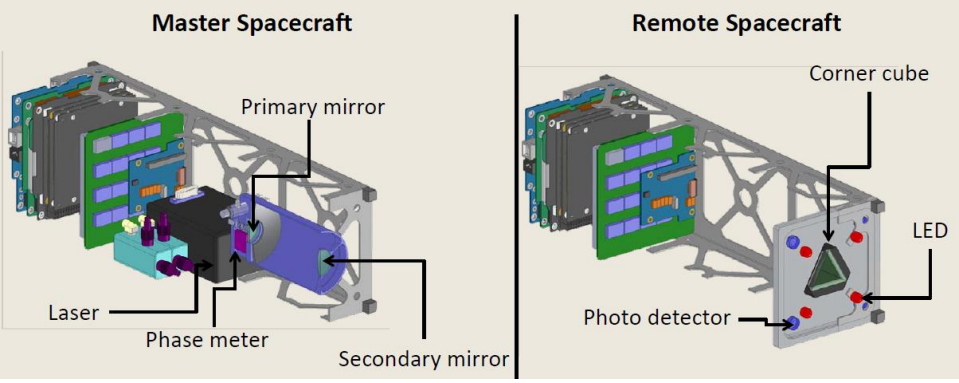

Figure 3-2. Transmitter and receiver satellites representation (Balakrishnan, 2013)

Following a very similar approach, a two-way ranging approach can be adopted if installing a mirror in the receiver satellite (remote spacecraft in Figure 3-2) that can refract the signal back to the transmitter satellite (master spacecraft in Figure 3-2) in which the travelling time is recorded. The biggest advantage of this method is that its precision no longer depends on the synchronization of the clocks of both satellites. Both the transmission and receiving time of the signal is measured in the same time scale, the one of the transmitting satellite, and therefore it is a reliable and adequate solution for inter-satellite ranging (Alawieh, 2016). As previously mentioned, the high accuracy of the range estimation would follow from an accurate calculation of the signal travelling time that is possible due to a very low wavelength in the optical laser

frequency band. The mathematical way to estimate the range between the satellites in this approach is as shown in Equation 3.2.

$$R_t\,(t_t) = \frac{1}{2}c(t_r - t_t) \tag{3.2}$$

where

t_t	transmission time in the transmitter clock scale [s]
t_r	receiving time in the transmitter clock scale [s]
c	speed of light [m/s]
R_t	apparent range at transmission time [m]

Following the simplified sketch of a two-way range system architecture shown in Figure 3-3 below, the total range estimated in this ranging method can be expressed by the additions of the different section lengths shown in the mathematical expression of Equation 3.3 (Sheard et al., 2012).

$$R_f(t) = \frac{1}{2}[x_1(t) + L_{12}(t) + y_2(t) + L_{21}(t) + x_2(t) + y_1(t)] \tag{3.3}$$

in which

- R_f represents the apparent relative range between the satellites [m]
- x_1 represents the signal path from its generation spotlight out of the transmitter spacecraft [m]
- L_{12} represents the first transmission of the signal in free space. From transmitter to receiver satellite [m]
- y_2 is the distance from the outside part of the receiver satellite to the reflecting mirror [m]
- x_2 represents the signal path from the reflecting mirror out of the receiver spacecraft [m]
- L_{21} represents the second transmission of the signal in free space. From receiver to transmitter satellite [m]
- y_1 is the distance from the outside part of the transmitter satellite back to its spotlight source [m]

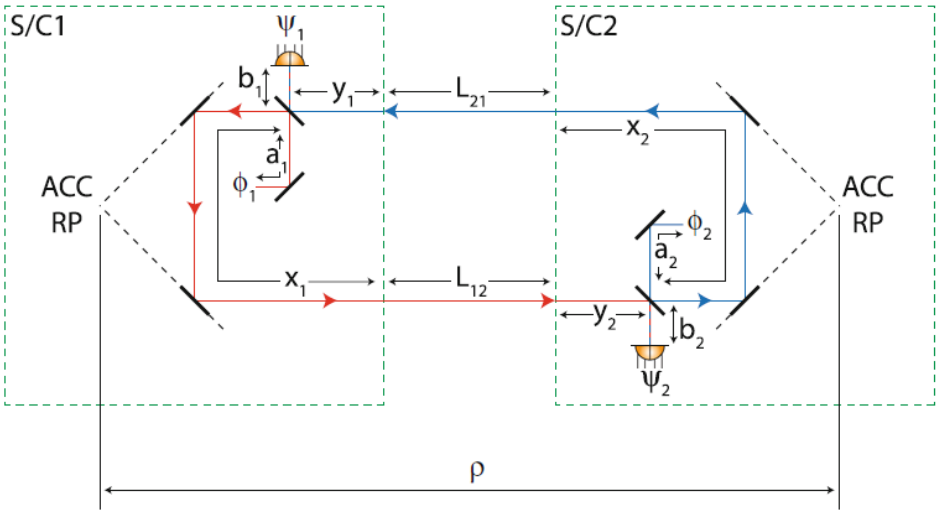

Figure 3-3. Two-way ranging (Sheard et al., 2012)

In the NAPEOS software used for means of this thesis work (ESA, 2009), the way to simulate the range estimations would be by adding white Gaussian noise to the real relative distance between

the satellites (provided by the considered real orbits of the satellites). Due to the fact that a two-way range is assumed, no clock correction had to be included and the level of noise was set at the level as close as possible of the current state-of-the-art ISL ranging observations (micrometer level). As it will be explained in the relative POD results (Chapter 7), it has been quite difficult to fit this relative distance observations into the LSQ algorithms due to conditioning problems. Thus, in other terms, the noise level for the range ISL observations was not placed at the state-of-the art level (few nanometers) but a couple of orders of magnitude higher due to the software limitations.

$$R_f = \rho + \varepsilon_f \tag{3.4}$$

in which R_f represents the ISL range observation in meters, ρ the true geometric distance between the satellites in meters and ε_f the white Gaussian noise to include instrument characteristics as well as the ones inherent to the transmission of the signal in free-space.

Finally, it is important to mention that there is a very precise method known as interferometry that has been considered to be implemented in state-of-the-art missions like LISA and is thought to be the most accurate way of estimating the range between the satellites. It has not been considered for this thesis study since the status of the software would not allow to such complex modelling but it is worth mentioning the most important features of the technique. The main idea behind interferometry is to lock the laser frequency in the transmitter satellite and send it towards the receiver satellite. Then, the frequency in the receiver satellite is not locked and therefore once it receives the signal, it transmits it back towards the transmitter satellite. The heterodyne signal of the superposition of the reference locked signal of the transmitter satellite and the one received back from the receiver satellite represents the double of the Doppler shift of the relative motion between the satellites (Dahl et al., 2016). Moreover, due to the fact that the frequency of a laser signal is quite high, these variations in Doppler shift are very sensitive which translates in very high accurate measurements on the changes of relative distance between satellites. This is because it measures the interference signal that results from the superposition (also known as interference pattern) of a local reference signal and the received signal from a target satellite (Darbeheshti, 2017). The full system architecture is shown below in Figure 3-4.

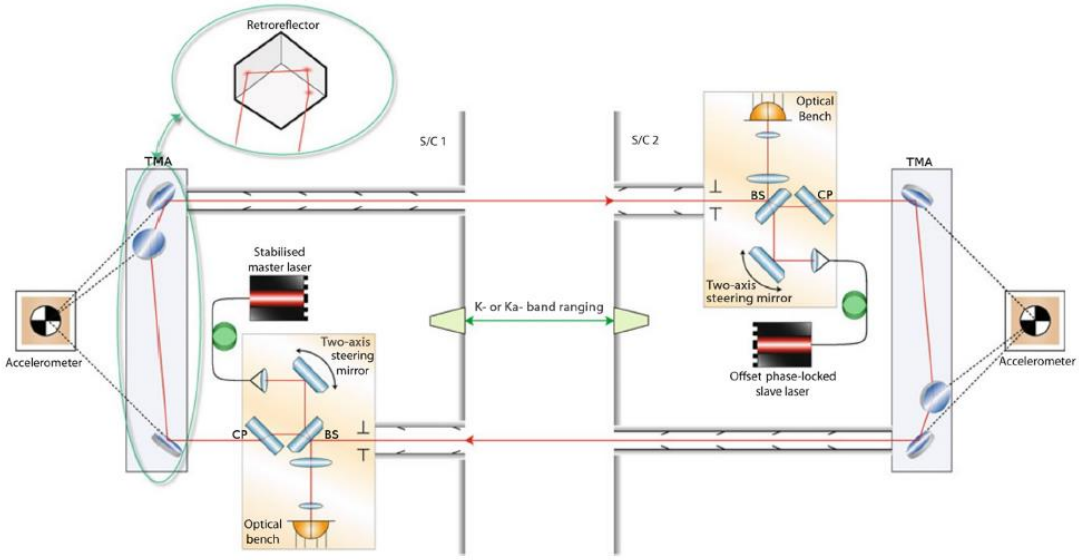

Figure 3-4. Laser ranging interferometry system layout (Sheard et al., 2012)

3.3 Signal delays

When a signal is transmitted from one satellite to another in free-space, it is affected by many errors that need to be accounted for. Moreover, these errors can be classified in two different types: the ones inherent to the hardware instruments used in the transmission/reception of the signal (antennas, clocks, etc) and the ones that directly delay the transmission of the signal (Montenbruck et al., 2000). For the purpose of this thesis, the hardware errors of the ISL systems can be considered the same as the instrumental delays presented for the GNSS constellations (see section 2.2.2). On the other hand, it is vital to explain the particular errors and delays that affect the transmission of an optical or radio signal that is being transmitted from one satellite to another. In such a way, a signal will suffer a power loss due to its propagation in free-space and may also be affected by the ionosphere (depending on the geometry of the case) (Dirkx, 2015).

First of all, it has to be taken into account that Satellite Laser Ranging (SLR) systems use laser pulses that have a Gaussian-like shape intensity profile. Therefore, the spatial signal intensity of the beam in the far field is dependent on the signal intensity at the waist, distance covered and wavelength (Dirkx, 2015).

$$I(r,z) = I_0 \left(\frac{\omega_0}{\omega(z)}\right) e^{\left(-2\frac{r^2}{\omega(z)^2}\right)} \tag{3.5}$$

$$\omega(z) \approx \frac{\lambda z}{\pi \omega_0} \tag{3.6}$$

where
r: off-axis distance [r]
I_0: signal internsity at the waist [dB] (defined as z=0 here)
λ: wavelength of laser pulse [m]
$\omega(z)$: laser spot size [m]
ω_0: Gaussian beam radius at waist [m]

Atmospheric delay is one of the main challenges for obtaining precise range observations between satellites. The effect of the atmosphere in the signal is reflected in a range correction (Dirkx, 2015). Please note that the first term is known as excess path delay and the one in brackets as geometric delay. The refractive index of the atmosphere is denoted as n in Equation 3.7.

$$\Delta s_{atm} = \int_{ray} (n-1) ds + \left(\int_{ray} ds - \int_{vac} ds \right) \tag{3.7}$$

However, the fact that a laser inter-satellite link signal is affected or not by the Earth's atmosphere depends on the geometry of their relative position with respect to Earth. Especially for the case of MEO-placed satellites with upward looking antennas, the laser signal emitted from one satellite to another will most likely not go through any of the layers of Earth's atmosphere. If it did, it would probably cross across the highest layers of the atmosphere, such as the ionosphere that does not affect the optical signals. As shown in Degnan (2011) and Sosnica et al. (2015), the optical signals are 70 times less sensitive than GNSS signals to the ionospheric delay, which then reduces greatly the severity of the problem. Finally, if the signal travelled through the troposphere it would have to be corrected for the diffraction caused. However, the ESA study on which this work is based, states that the inter-satellite ranging measurements will not take place continuously but only in favorable times/positions. Hence, it can be assumed that for the purpose of this work, there will be no need to actually model the laser atmospheric delays. In any case, a minimum grazing altitude in the simulation of the signals of 100km was selected in order to rule out the signals that could at some point travel across Earth's troposphere. Additionally, as mentioned before, the ionosphere does not affect the optical signal in a severe way.

4

Precise Orbit Determination

Precise Orbit Determination refers to the process in which the orbit of a user satellite is reconstructed with high fidelity. To achieve this, observations of the target satellite are taken from either ground stations on Earth or a set of constellations of satellites known as Global Navigation Satellite Systems (GNSS) placed in medium-MEO orbits (Montenbruck et al., 2000). This is especially important in missions with high-orbit requirements like Synthetic Aperture Radar (SAR) and altimetry missions but its demand and range of applications are growing at a fast pace in recent times.

In general terms, there are two main approaches to this problem: kinematic and dynamic. The main difference between them is that the kinematic approach, also known as geometric, does not make use of the corresponding dynamical model that determines the motion of any Earth-orbiting satellite. Because of that, the kinematic method is only able to estimate the position at a specific instant in time in which there are a minimum number of GNSS satellites in sight, which means that the orbit solution is discretized. For a dynamical approach, the orbit solution is continuous and is generally the result of a trade-off between the weight of the observations and the weight of the dynamical model. In this case, an initial state vector that optimizes the fit of the observations is estimated and the full orbit is obtained by means of propagation. The state vector does not only contain values of position and velocity but also a set of model parameters. Depending on the specifics of the scenario, these parameters can be fixed or estimated following the minimization of the residuals in the least-squares or Kalman filter algorithm. The different perturbations that affect and govern the movement of the satellites in their orbits have to be known to best extent possible to improve the accuracy of the determined trajectory.

The objective of this chapter is to review all aspects that are important and that affect any POD process. First, and since the high-precision approaches to POD make use of a dynamical approach, the different perturbations that govern the motion of any Earth-orbiting satellite are reviewed. The models that are currently state-of-the-art in the industry to represent such forces and that are used in this project are presented as well as the reasons why some of them can be neglected due to the specific orbit conditions considered for this thesis work. Second, the least square algorithm used to perform the POD processes in this study is reviewed. Its main properties and advantages are stressed and an introduction to the mathematical formulation behind it is presented. Third, the inaccuracies in both force models and satellite physical properties that affect the accuracy of the resulting orbit estimation are presented to help understand that limiting those inaccuracies can greatly reduce the error of the estimation. Finally, the inclusion of inter-satellite links in the general POD process is introduced since relative navigation is the main core of this thesis work.

4.1 Reference frames

Throughout the work performed in this master thesis, different coordinate systems have been employed depending on the nature of the variables and mathematical procedures in questions. They generally divide into two main groups: Earth-centered, whose origin is located in Earth's center of mass and body-centered, in which the origin is placed in the center of mass of a particular user satellite. In this section the most relevant and representative reference frames are presented, which are the Earth-centered J2000 ECI and the body-frame RSW coordinate systems.

4.1.1 J2000 ECI

The J2000 reference frame is one of the most commonly used inertial reference frames for POD of LEO satellites. It is defined with the alignment of the x-axis with Earth's Mean Equator and Equinox at 12:00 TT on the 1st January 2000, the z-axis is aligned with the Celestial North Pole and the y-axis is oriented in a way to complete the trihedral (Tapley, 2004). This reference frame is very useful in orbit determination since even though it is quasi-inertial (Earth still rotates around the Sun), the dynamics of the satellite can be expressed in a much easier and simpler way.

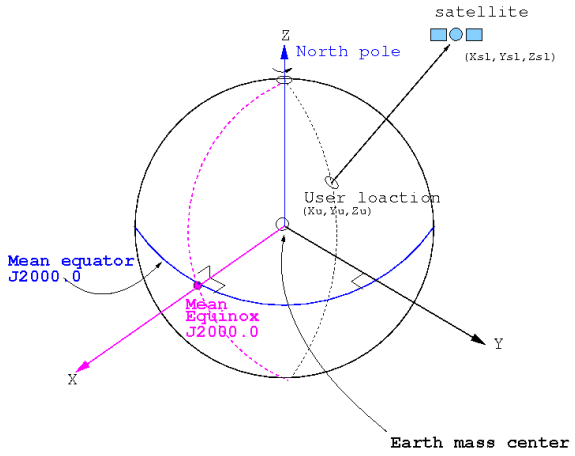

Figure 4-1. J2000 ECI reference frame (Navipedia, 2020)

4.1.2 RSW

As will be later explained in detail, dynamic POD processes present model errors and uncertainties that are absorbed by the so-called empirical accelerations. It is also important to state that they do not absorb observation noise. In order to be able to tune these fictional impulses in a more sensible way and to understand fully their impact on the dynamics of the satellite, they are generally estimated in the well-known RSW body-frame. As shown below in Figure 4-2, in this body-frame the radial component (R axis) is defined to be always pointing towards Earth's center of mass along the vector that connects it with the satellite's center of mass. The along-track component (S axis) is defined normal to the radial component (Equation 4.1)4.14.1, and therefore not always aligned with the velocity component of the satellite (except for a circular orbit). Finally, the cross-track component (W axis) is normal to the orbital plane completing the trihedral (Chen et al., 2016). Please note that the RTN body-frame could also be used, and even though very similar to the RSW frame, the definition of the axes alignment is not the same – also depicted in Figure 4-2.

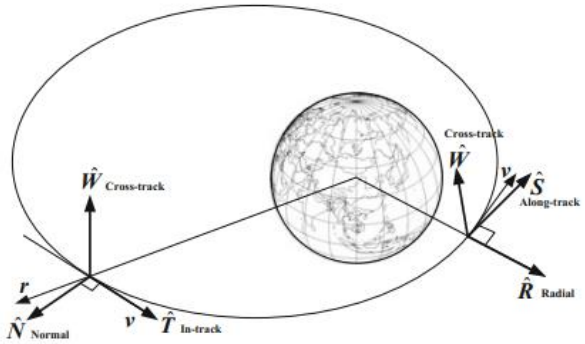

Figure 4-2. RSW and RTN body-centered reference frames (Chen et al., 2016)

$$\hat{\boldsymbol{R}} = \frac{\boldsymbol{r}}{|\boldsymbol{r}|} \qquad \hat{\boldsymbol{W}} = \frac{\boldsymbol{r} \times \boldsymbol{v}}{|\boldsymbol{r} \times \boldsymbol{v}|} \qquad \hat{\boldsymbol{S}} = \hat{\boldsymbol{W}} \times \hat{\boldsymbol{R}} \tag{4.1}$$

4.2 Dynamical model

Following the laws of Newtonian physics, the acceleration exerted on a body placed in position r and velocity v that is under the influence of a mass m can be expressed by the following differential equation (Montenbruck, 2010).

$$U = F(t, r, v)/m \tag{4.2}$$

For a nominal Earth-orbiting satellite, the total force that it experiences is a combination of the following set of forces: central body gravitational acceleration ($-\mu/r^2\ \hat{r}$), irregularities in Earth's gravity field ($\ddot{r}_{eg}$), third-body gravitational accelerations ($\ddot{r}_{3b}$), Earth's tidal effects ($\ddot{r}_t$), solar radiation pressure ($\ddot{r}_{srp}$), drag caused by Earth's atmosphere and aerodynamic forces ($\ddot{r}_a$), general relativity ($\ddot{r}_{gr}$) and Earth's infrared and albedo radiation ($\ddot{r}_{erp}$) (Doornbos, 2012).

$$\ddot{r} = -\frac{\mu}{r^2}\hat{r} + \ddot{r}_{eg} + \ddot{r}_{3b} + \ddot{r}_t + \ddot{r}_{gr} + \ddot{r}_a + \ddot{r}_{srp} + \ddot{r}_{erp} + \ddot{r}_{other} \tag{4.3}$$

4.2.1 Earth Gravity

For this thesis work, Earth Gravity is considered the main driving force for any Earth orbiting satellite to the extent that all other perturbations affecting the motion of the satellites are considered of first order expansion about this one (ESA, 2009). Since Earth is not a perfect sphere and its mass distribution is not homogeneous, in order to define the acceleration of any orbiting body, the following complex mathematical formulation must be employed to describe the Earth's gravity field (Montenbruck et al., 2000).

$$U = \frac{GM}{r}\sum_{n=0}^{\infty}\sum_{m=0}^{n}\frac{R^n}{r^n}P_{nm}\sin(\theta)\,(C_{nm}\cos m\lambda + S_{nm}\sin m\lambda) \tag{4.4}$$

where

U	Earth's gravity potential
G	Gravitational constant
M	Earth's mass
R	Earth's radius
r	Distance to Earth center of mass
n	Degree
m	Order
P_{nm}	Associated Lagrange polynomial

C_{nm}, S_{nm}	Coefficients
λ	Latitude
θ	Longitude

4.2.2 Third body

Even though an Earth-orbiting satellite is mainly attracted by the Earth's gravity, it is, to a lesser extent, also attracted by other celestial bodies that orbit in proximity to Earth. For instance, the constellation of satellites that will be subject of study of this project will not only be attracted by Earth's gravity field but also by the Moon's, the Sun and all planets that are part of the Solar System, including Pluto (ESA, 2009). The influence of these third bodies is modelled by means of the following formulation (Montenbruck et al., 2000).

$$\ddot{\vec{r}} = \sum_{k=1}^{n} \mu_k \left[\frac{\overrightarrow{r_k} - \vec{r}}{|\overrightarrow{r_k} - \vec{r}|^3} - \frac{\overrightarrow{r_k}}{|\overrightarrow{r_k}|^3} \right] \tag{4.5}$$

where

$\ddot{r}$	Acceleration of the satellite
μ_k	Gravitational parameter of body k
r_k	Distance from the k body to Earth
r	Distance from the satellite to Earth
n	Total number of bodies

4.2.3 Solar radiation pressure

A satellite in free-space exposed to Sun's radiation will experience acceleration due to the reflection and absorption of photons. The magnitude of the force exerted by the Sun's radiation on the satellites will depend on the solar flux (energy that passes through an area for a given instant in time) and the cross-sectional area of the satellite as described in Montenbruck et al. (2000). This acceleration is generally the sum of the photons coming from the Sun directly and the ones reflected by Earth. However, in this case Earth Radiation Pressure (ERP) is much smaller than Solar Radiation Pressure (SRP) since ERP only affects satellites close to Earth and therefore it is neglected for this thesis work.

There are several available models that can be followed to estimate this perturbing force. However, in this project the main model that is employed to estimate this perturbing force is known as IERS Solar Radiation Pressure (ESA, 2009). Following the mathematical background found in McCarthy et al. (2003), the solar radiation acceleration induced in the orbiting satellites may be expressed as follows. The generic model from IERS will be used considering constant area and conical shadow model (umbra and penumbra) with Earth, Moon and Sun radii. Please note that both K and Cr factors are scalar whose value depends on the solar radiation intensity, mass and cross-sectional area of the satellite.

$$\ddot{\vec{r}} = K^* C_R \frac{\vec{R}}{R} \tag{4.6}$$

$$K^* = \frac{I_{AU}}{c} \left(\frac{R_{AU}}{R} \right)^2 \frac{A_R}{m} \tag{4.7}$$

where

C_R	Solar radiation coefficient (scale factor)
$\vec{R}, R$	Heliocentric radius vector (and its norm) of the satellite
I_{AU}	Solar intensity of radiation at one astronomical unit
R_{AU}	One astronomical unit
A_R	Cross sectional area (as seen from the Sun)
m	Satellite mass
c	Speed of light

4.2.4 Solid and Ocean Tides

The fact that the Earth is not perfectly rigid makes that it temporary deforms under the gravitational influence of any third body: Sun and Moon mainly (ESA, 2009). Additionally, it is important to note that the tidal variation on the Earth surface consists of two terms: direct and indirect. The direct one relates to the small periodic deformations of the solid body of the Earth whereas the indirect one contemplates the different response that the oceans present (Kansowa et al., 2010). When it comes to modelling the Solid Earth tides, the changes induced by this effect are taken into account by means of variations in the geopotential coefficients C_{nm} and S_{nm}. Such modifications in the coefficients are expressed in terms of the k Love number (McCarthy et al., 2003).

$$\Delta U = \frac{\mu_\oplus}{r}\sum_{l=2}^{\infty}\sum_{k=1}^{l}\left(\frac{R_\oplus}{r}\right)^l P_{lk}(\sin\phi)\left[\Delta C_{lk}\cos m\lambda + \Delta S_{lk}\sin m\lambda\right] \tag{4.8}$$

with

$$\Delta C_{nk} = k_n(2-\delta_{0k})\frac{(n-k)!}{(n+k)!}\sum_{j=1,2}\frac{M_j}{M_T}\left(\frac{R_\oplus}{r_j}\right)P_{nk}(\sin\phi_j)\cos k(\lambda_j-\phi) \tag{4.9}$$

$$\Delta S_{nk} = k_n(2-\delta_{0k})\frac{(n-k)!}{(n+k)!}\sum_{j=1,2}\frac{M_j}{M_T}\left(\frac{R_\oplus}{r_j}\right)P_{nk}(\sin\phi_j)\sin k(\lambda_j-\phi) \tag{4.10}$$

where
k_n is the Love number for degree n
ϕ is the phase due to the inelasticity of the Earth

Regarding the ocean tides, their dynamical effects are also modelled and taken into account by means of variations in the geopotential coefficients. However, in this case the geopotential coefficients modifications are incorporated by periodic variations in the normalized Stokes' coefficients. In general terms, it is safe to say that the temporary variations in the mass distribution of the Earth are accounted for in the geopotential which will then influence the gravitational influence on the satellite.

$$\Delta U = 4\pi G R_\oplus \rho_w \sum_{l=2}^{\infty}\sum_{m=0}^{l}\sum_{s}\frac{1+k_l'}{2nl+1}\left(\frac{R_\oplus}{r}\right)^{n+1}\left(A_{s,l,m}\cos m\lambda + B_{s,l,m}\sin m\lambda\right) \tag{4.11}$$

4.2.5 Relativistic effects

When accurately modelling the motion of an orbiting satellite around a heavy body like Earth, relativistic effects need to be considered due to the curvature in the time-space. The complex mathematical formulation can be found in McCarthy (2003) in which it can be noted that both corrections of the geodesic precession by de Sitter and the frame-dragging precession by Lense and Thirring are neglected. The simplified contribution to the acceleration of the satellite can be expressed following the mathematical expression found below.

$$\ddot{\vec{r}} = -\frac{\mu}{c^2 r^3}\left\{\left[4\frac{\mu}{r} - (\vec{r}\times\dot{\vec{r}})\right]\dot{\vec{r}} + 4(\vec{r}\cdot\dot{\vec{r}})\dot{\vec{r}}\right\} \tag{4.12}$$

where

r	Position vector
v	Velocity vector

4.2.6 Atmospheric Drag

As its name indicates, some Earth-orbiting satellites experience a drag force due to the interaction with the atmosphere. This force is exerted in the opposite direction of the motion of the satellite therefore decelerating it. However, as can be found in Montenbruck et al. (2000), it is not easy to

estimate this perturbation because some parameters are very difficult to model. On one hand, the physical properties of the atmosphere are highly variable – especially regarding the density of the upper part. On the other hand, a high knowledge of the interaction of the particles with the different surfaces of the satellite is required and that is something also quite hard to model. The different mathematical formulation to be used in order to model the atmospheric drag can be found in Carrou (1995). In Otten (2008) it is mentioned that even though the altitude of 8,000km is high and therefore the density is low the atmospheric drag must be taken into account. Nevertheless, the atmospheric density decreases exponentially with altitude so for altitudes over 1,000km the atmospheric drag will be considered negligible as shown in Montenbruck et al. (2000).

4.2.7 Dynamical model uncertainties

As previously presented in this chapter, the trajectory described by any Earth-orbiting satellite is determined by the forces exerted on it. The correct modelling of such forces ensures an accurate prediction (propagation) and/or determination (POD) of the satellite's orbit. The main difference between orbit propagation and orbit determination is whether or not there are observations available (Figure 4-3). If no observations are available, the position and velocity of the satellite are integrated along time by considering the forces exerted on the satellite. Generally, due to the inaccuracies of the force models, the longer the prediction time range the higher the error. Contrarily if there are observations available, and even though the existing uncertainties in the models, the final trajectory will in some way fit the observations and be closer to reality.

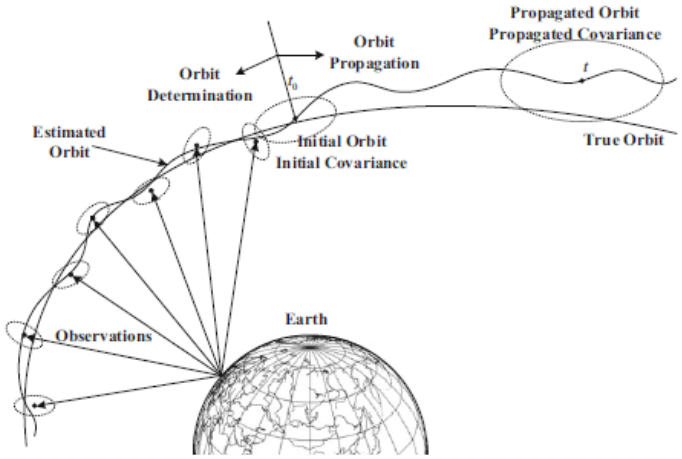

Figure 4-3. Difference in concept between orbit determination (left hand-side) and orbit propagation (right hand-side) (Chen et al., 2017)

If no observations are available, the only thing that can be done is to predict the trajectory of the satellite at later epochs. To do so, starting from an initial state vector, the position and velocity are integrated in small time steps until the position at the final epoch has been obtained. The accuracy of the prediction then completely relies on the accuracy of the force models used. If very precise force models are available, the resulting orbit will likely be quite representative of reality even though not even current models are perfect. However, if the available models are not state-of-the art, the form and orientation of the estimated orbit will divert much from the real one. Examples of the mentioned force models are the gravity potential and SRP. On top of that, there are also physical properties of the satellite whose accurate knowledge is vital to obtain a realistic estimation of its trajectory. For instance, the cross-sectional area and centre of mass directly influence the radiation and Earth's gravitation force exerted on the satellite. Finally, the ephemeris and clock data from the GNSS constellations also present uncertainties that will affect the reconstruction of observations (they depend on user and GNSS satellites positions) in the POD process and hence the modelled orbits of the MEO-placed satellites.

Empirical accelerations

The inherent inaccuracies in the force models, ephemeris and observation data as well as the uncertainties in the parametrization of the satellite's physical properties, make it advisable to include some stochastic parameters in the orbit determination process to compensate them (Wang, 2015). Generally, they take the form of empirical accelerations, which can be thought as fictional instantaneous velocity pulses added to the spacecraft, for constant sub-intervals of time. These accelerations are included in the state vector, along with the rest of model parameters, and give the least-squares algorithm more degrees of freedom to adjust the integrated orbit to the set of given observations. In geopotential missions such as CHAMP and GRACE, the use of empirical accelerations in the POD process is vital to achieve the high orbit accuracy requirements that they present (Visser et al., 2007). They are defined in the current RSW body-frame of the satellite explained in section 4.1.

When it comes to the mathematical formulation of these fictional accelerations and how to include them in the overall LSQ process, the information found in Wang (2015) can be followed but there are different parametrizations that can be used. For an observation arc in the range $[t_0, t_f]$, it is divided into piece-wise sub-intervals of the same time length. In each of those sub-intervals, a different set of empirical accelerations $a_i = (a_R, a_T, a_N)^T$ are considered, defined in the current RSW body-frame of the satellite; therefore, applied in the radial, along-track and cross-track components. Therefore, the equation of motion is quite similar to what is presented below in Equation 4.13. Please note that for the orbit integration process, the empirical accelerations have to be converted to the J2000 ECI reference frame so that they can be added to the rest of forces exerted on the satellite whereas in the state vector of the LSQ algorithm, they are expressed in the body-frame of the corresponding satellite.

$$\ddot{\boldsymbol{r}} = \boldsymbol{a}(t, r, v,) + \left(a_{R_i} \cdot \boldsymbol{e_R}(t) + a_{S_i} \cdot \boldsymbol{e_S}(t) + \ a_{W_i} \cdot \boldsymbol{e_W}(t)\right)^T \tag{4.13}$$

where $[e_R(t), e_S(t), e_W(t)]^T$ represents the orientation of the RSW body-frame of the satellite in the J2000 ECI system at time t, i represents the sub-interval in which these accelerations are being applied and $[a_R, a_S, a_W]$ represent the magnitude of the empirical accelerations at the mentioned sub-interval in each of the body-frame components.

An example of the final result of the estimation of piece-wise empirical accelerations is shown below in Figure 4-4. These graphs have been taken from Jaggi et al. (2005) and they show the graphical output of the empirical accelerations in the along-track component of the CHAMP satellite. It gives the reader an idea of the nominal duration of the sub-intervals in which the accelerations are estimated which generally lies between 10-15 minutes; longer intervals would decrease the accuracy of the determination and shorter ones would leave so many degrees of freedom to fit the observations that the resulting orbit would be not realistic. Please be aware that the duration is dependent on the parametrization of the empirical accelerations. When 1-CPR accelerations are estimated, the duration is generally longer. Additionally, it can be seen that the order of magnitude of these residual accelerations are in the nm/s^2 level which enlightens the fact that they just serve the purpose of helping refine the resulting orbit. It is also important to bear in mind that for that in this specific case, the estimation of the acceleration residuals seem to be more critic in both along-track and cross-track. The first one can be related to the mismodeling of the drag force which is exerted in the direction of movement (along-track) and the second one is due to the inaccuracy in the modelling of the solar radiation pressure force (Wang, 2015). As it will be later proven, for MEO-placed satellites and since drag is neglected, the main reason why empirical accelerations are required in along-track components are related to errors in the user satellite receiver clock as well as inaccuracies in the geopotential model and GNSS orbits and clocks. The reason behind the residuals in the cross-track component are still the radiation pressure from the Sun, whose influence is bigger in higher altitudes.

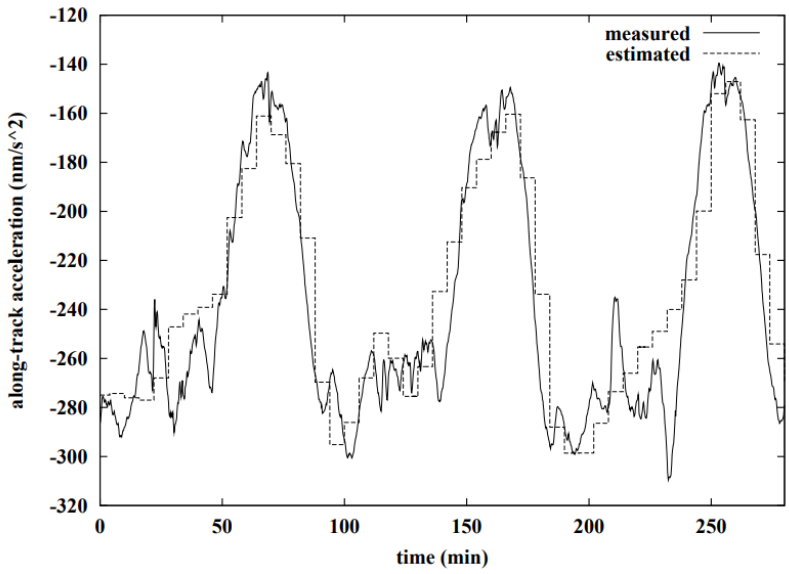

Figure 4-4. Example of piecewise empirical accelerations in along-track component estimated every 6 minutes for CHAMP satellite (Jaggi et al., 2005)

Finally, it is important to mention that the influence of the empirical accelerations on the final orbit solution is also taken into account by the least-squares algorithm to update the a-priori values (generally set null) until the optimum values have been found. Due to the fact that the state transition matrix only accounts for the partial derivatives of the initial position and velocity, the rest of parameters of the state vector (model parameters) have their influence quantified in the so-called sensitivity matrix. Thus, in the specific of this case, and for the processes in which empirical accelerations are considered, the extended state vector and sensitivity matrix is built-up in the following way.

$$X_0 = \begin{bmatrix} x_0 & y_0 & z_0 & \dot{x_0} & \dot{y_0} & \dot{z_0} & C_R & a_{R_1} & a_{S_1} & a_{W_1} & \cdots & a_{R_n} & a_{S_n} & a_{W_n} \end{bmatrix}^T \tag{4.14}$$

$$\boldsymbol{S} = \begin{bmatrix} \frac{\partial x}{\partial C_R} & \frac{\partial y}{\partial C_R} & \frac{\partial z}{\partial C_R} & \frac{\partial \dot{x}}{\partial C_R} & \frac{\partial \dot{y}}{\partial C_R} & \frac{\partial \dot{z}}{\partial C_R} \\ \frac{\partial x}{\partial a_{R_1}} & \frac{\partial y}{\partial a_{S_1}} & \frac{\partial z}{\partial a_{W_1}} & \frac{\partial \dot{x}}{\partial a_{R_1}} & \frac{\partial \dot{y}}{\partial a_{S_1}} & \frac{\partial \dot{z}}{\partial a_{W_1}} \\ \vdots & \vdots & \vdots & \vdots & \vdots & \vdots \\ \frac{\partial x}{\partial a_{R_n}} & \frac{\partial y}{\partial a_{S_n}} & \frac{\partial z}{\partial a_{W_n}} & \frac{\partial \dot{x}}{\partial a_{R_n}} & \frac{\partial \dot{y}}{\partial a_{S_n}} & \frac{\partial \dot{z}}{\partial a_{W_n}} \end{bmatrix}^T \tag{4.15}$$

where n represents the total number of sub-intervals in which the observation arc has been divided.

4.3 Batch least-squares algorithm in POD

It is important to understand that this section is not focused in doing a literature review on the characteristics of the different algorithms that can be used in an orbit determination process. Instead, the goal is to review the specific algorithm used in the NAPEOS software, the tool in which the simulations of this work have been carried out. Therefore, it is important to stress that the different properties and characteristics presented in the following sections only apply to the current specific case.

There is not a unique mathematical approach to the determination process of a satellite's trajectory. Indeed, there are two main algorithms used in any process in which a set of parameters that optimize a given cost function are estimated. In the highest possible level, since they both present various ramifications from the main algorithms, the two methods that can be found are

known as Least-squares and Kalman filter. The main difference between them is how they treat the data: since the Least-squares algorithm process all the data in batch, the Kalman filter does it sequentially.

As taken from Montenbruck (2010) and ESA (2019), the least-square methods are the ones that obtain the best estimate of an a-priori state vector by minimizing the square of the difference between a set of real observations and the expected value obtained by means of an observation model. When referring to the state vector ($\boldsymbol{X}_0$), not only are the position and velocity of the satellite included but also a set of physical parameters such as the drag coefficient, solar radiation coefficient, albedo coefficient, etc. Depending on the specifics of the problem, some of these parameters will be estimated, fixed or even not considered, however only the ones being estimated will be included in the state vector. Additionally, the covariance matrix of the parameters in the state vector is also displayed below ($\boldsymbol{P}_0$). It can be seen that σ_{ii} expresses the a-priori covariance of a determined parameter, meanwhile σ_{ij} refers to the a-priori covariance of two different parameters, showing how much they are correlated or are independent from one another.

$$\boldsymbol{X}_0 = \begin{bmatrix} x_0 \\ y_0 \\ z_0 \\ \dot{x}_0 \\ \dot{y}_0 \\ \dot{z}_0 \\ C_R \end{bmatrix} \qquad \boldsymbol{P}_0 = \begin{bmatrix} \sigma_{11}^2 & \sigma_{12}^2 & \cdots & \sigma_{17}^2 \\ \sigma_{21}^2 & \sigma_{22}^2 & \cdots & \sigma_{27}^2 \\ \vdots & \vdots & \ddots & \vdots \\ \sigma_{71}^2 & \sigma_{72}^2 & \dots & \sigma_{77}^2 \end{bmatrix} \tag{4.16}$$

On the other hand, the observations are stored in a column-vector as it is displayed below (***z***). In this vector, all observations available are properly stored with the ones referring to earlier epochs going first and in groups. For instance, all pseudorange (code) observations from the first epoch are stored first, followed by all phase measurements and, if applicable, all inter-satellite link ranging observations. Then, the same is done for the second epoch, up until the last one. The a-priori accuracy of each of the observations is represented in the weight matrix (observation a-priori covariance matrix, ***W***). Such matrix is diagonal because it is assumed that the observations are not correlated.

$$\boldsymbol{z} = \begin{bmatrix} z_1 \\ z_2 \\ \vdots \\ z_m \end{bmatrix} \qquad \boldsymbol{W} = \begin{bmatrix} \sigma_1^2 & 0 & \cdots & 0 \\ 0 & \sigma_2^2 & \cdots & 0 \\ \vdots & \vdots & \ddots & \vdots \\ 0 & 0 & \dots & \sigma_n^2 \end{bmatrix} \tag{4.17}$$

As previously said the main goal of a least-squares algorithm in orbit determination is to minimize the sum of the weighted of the observations residuals. Such residuals arise from the differences between the real or simulated observations and the observations modelled following the geometry between the GNSS and user satellites. In such a way, the estimated residuals are a function of the state vector of the user satellite in each of the epochs. Thus, the residuals observation vector is expressed as follows.

$$\boldsymbol{\varepsilon} = \begin{bmatrix} z_1 - f_1\left(\hat{X}(t_1)\right) \\ z_2 - f_2\left(\hat{X}(t_2)\right) \\ \vdots \\ z_m - f_m\left(\hat{X}(t_m)\right) \end{bmatrix} \tag{4.18}$$

From these definition of observation residuals, the loss function can be derived, also known as Jacobian matrix. Minimizing this cost function ensures that the fit of the observations will be optimized, therefore improving the accuracy of determined orbit trajectory. Please note that Ψ refers to uncertainties in the estimation of the a-priori covariance values of the variables in the state vector. Additionally, ΔX_0 refers to the differences with respect to the a-priori state vector and the update one – therefore it is null in the first iteration.

$$\boldsymbol{J} = \boldsymbol{\varepsilon}^T \cdot \boldsymbol{W}^{-1} \cdot \boldsymbol{\varepsilon} + \boldsymbol{\Psi} = \boldsymbol{\varepsilon}^T \cdot \boldsymbol{W}^{-1} \cdot \boldsymbol{\varepsilon} + \Delta \boldsymbol{X}_0^T \cdot \boldsymbol{P}_0^{-1} \cdot \Delta \boldsymbol{X}_0 \tag{4.19}$$

As explained in ESA (2019), the least-squares algorithm is iterative and keeps on re-estimating the state vector variables until convergence is reached (observation residuals can no longer be minimized). Skipping all the mathematical formulation found in Montenbruck (2000), the state vector is continuously being updated as shown in Equation 4.20 below. These equations are known as Normal Equations.

$$\Delta \boldsymbol{X}^{lsq} = (\boldsymbol{P}_0^{-1} + \boldsymbol{A}^T \cdot \boldsymbol{W} \cdot \boldsymbol{A})^{-1} \cdot \left(\mathbf{P}_0 \Delta \boldsymbol{X}_0^{apr} + \boldsymbol{A}^T \boldsymbol{W} \Delta \boldsymbol{z}\right) \tag{4.20}$$

In which:

$\Delta \boldsymbol{X}_0^{lsq}$: update of state vector after solving normal equations
$\Delta \boldsymbol{X}_0^{apr}$: difference between current state vector and the a-priori estimation
$\boldsymbol{P}_0$: Covariance matrix of the a-priori state vector estimations
A: observations partials matrix
$\boldsymbol{Q}_0$: observations weight matrix (covariance matrix of observations)
$\Delta \boldsymbol{z}$: residual observation matrix

From the equation above, the only term that has not been previously introduced is known as "observation partials matrix". In other words, these matrix provides the change in the estimation of the modelled observations with respect to each of the state variables. Since the real observations are fixed, if knowing how the estimated observations change with respect to the state vector, the behaviour of the observations residuals can be predicted. All this information is obtained by means of partial derivatives as shown below. Please note that α refer to the state variables that are not dynamical, i.e. solar radiation pressure coefficient. Other examples of these variables can be the drag coefficient or the albedo coefficient.

$$\boldsymbol{A} = \begin{bmatrix} \frac{\partial f_1}{\partial x_0} & \frac{\partial f_1}{\partial y_0} & \frac{\partial f_1}{\partial z_0} & \frac{\partial f_1}{\partial \dot{x}_0} & \frac{\partial f_1}{\partial \dot{y}_0} & \frac{\partial f_1}{\partial \dot{z}_0} & \frac{\partial f_1}{\partial \alpha_1} & \cdots & \frac{\partial f_1}{\partial \alpha_k} \\ \frac{\partial f_2}{\partial x_0} & \frac{\partial f_2}{\partial y_0} & \frac{\partial f_2}{\partial z_0} & \frac{\partial f_2}{\partial \dot{x}_0} & \frac{\partial f_2}{\partial \dot{y}_0} & \frac{\partial f_2}{\partial \dot{z}_0} & \frac{\partial f_2}{\partial \alpha_1} & \cdots & \frac{\partial f_2}{\partial \alpha_k} \\ \vdots & \vdots & \vdots & \vdots & \vdots & \vdots & \vdots & \cdots & \vdots \\ \frac{\partial f_m}{\partial x_0} & \frac{\partial f_m}{\partial y_0} & \frac{\partial f_m}{\partial z_0} & \frac{\partial f_m}{\partial \dot{x}_0} & \frac{\partial f_m}{\partial \dot{y}_0} & \frac{\partial f_m}{\partial \dot{z}_0} & \frac{\partial f_m}{\partial \alpha_1} & \cdots & \frac{\partial f_m}{\partial \alpha_k} \end{bmatrix} \tag{4.21}$$

The partial derivatives shown above in Equation 4.21 can be quite time-consuming to obtain or completely straight-forward, since some of them are null. The calculations are highly dependent on the nature of the variable with respect to which the derivative is taken. In the specific case of this master thesis, the way to determine the A matrix is by decomposing into the following matrices as shown in Montenbruck (2000).

$$\boldsymbol{A} = \boldsymbol{H} * [\boldsymbol{\phi}, \boldsymbol{S}] \tag{4.22}$$

- **H: Partials of the measurements with respect to the state vector**
  It represents the dependence of a modelled observation with respect to the dynamic variables in the state vector (position, velocity). The modelled observations follow from the definition of range between the GNSS and user satellites. Please note that since the modelled range observations are estimated kinematically making use of basic geometry rules, the partial derivatives with respect to velocity are null.

$$\boldsymbol{H}(t) = \left(\frac{\partial \boldsymbol{\varepsilon}}{\partial \boldsymbol{X}}\right) \tag{4.23}$$

$$\boldsymbol{H}(t) = \left(\frac{\partial \boldsymbol{f}(t)}{\partial \boldsymbol{X}}\right) = \left(\frac{x - X_s}{R}, \frac{y - Y_s}{R}, \frac{z - Z_s}{R}, 0, 0, 0\right) \tag{4.24}$$

where $\boldsymbol{\varepsilon}$ refer to the observations residuals $\boldsymbol{\varepsilon} = \boldsymbol{z} - f(\boldsymbol{X}(t))$, x,y,z as the coordinate positions of the user satellite and Xs, Ys, Zs as the coordinate positions of the GNSS satellite.

- **$\boldsymbol{\phi}$: State Transition Matrix**
  It is formed by the partial derivatives of the state vector (position, velocity) at a specific epoch with respect to the initial state vector. In other words, it measures the impact that a change in the initial state vector would have in the form and orientation of the orbit at a later epoch. It is important to state that in order to obtain these coefficients the variational equations need to be numerically integrated (Montenbruck, 2000).

$$\boldsymbol{\phi} = \begin{bmatrix} \frac{\partial x}{\partial x_0} & \frac{\partial x}{\partial y_0} & \frac{\partial x}{\partial z_0} & \frac{\partial x}{\partial \dot{x}_0} & \frac{\partial x}{\partial \dot{y}_0} & \frac{\partial x}{\partial \dot{z}_0} \\ \frac{\partial y}{\partial x_0} & \frac{\partial y}{\partial y_0} & \frac{\partial y}{\partial z_0} & \frac{\partial y}{\partial \dot{x}_0} & \frac{\partial y}{\partial \dot{y}_0} & \frac{\partial y}{\partial \dot{z}_0} \\ \frac{\partial z}{\partial x_0} & \frac{\partial z}{\partial y_0} & \frac{\partial z}{\partial z_0} & \frac{\partial z}{\partial \dot{x}_0} & \frac{\partial z}{\partial \dot{y}_0} & \frac{\partial z}{\partial \dot{z}_0} \\ \frac{\partial \dot{x}}{\partial x_0} & \frac{\partial \dot{x}}{\partial y_0} & \frac{\partial \dot{x}}{\partial z_0} & \frac{\partial \dot{x}}{\partial \dot{x}_0} & \frac{\partial \dot{x}}{\partial \dot{y}_0} & \frac{\partial \dot{x}}{\partial \dot{z}_0} \\ \frac{\partial \dot{y}}{\partial x_0} & \frac{\partial \dot{y}}{\partial y_0} & \frac{\partial \dot{y}}{\partial z_0} & \frac{\partial \dot{y}}{\partial \dot{x}_0} & \frac{\partial \dot{y}}{\partial \dot{y}_0} & \frac{\partial \dot{y}}{\partial \dot{z}_0} \\ \frac{\partial \dot{z}}{\partial x_0} & \frac{\partial \dot{z}}{\partial y_0} & \frac{\partial \dot{z}}{\partial z_0} & \frac{\partial \dot{z}}{\partial \dot{x}_0} & \frac{\partial \dot{z}}{\partial \dot{y}_0} & \frac{\partial \dot{z}}{\partial \dot{z}_0} \end{bmatrix} \tag{4.25}$$

- **S: Sensitivity Matrix**
  Not only do the initial orbit conditions influence its form and orientation at later epochs but also some model parameters that determine the forces that act on the satellite. In order to quantify such influence, the Sensitivity matrix, similarly to STM, expresses the dependence of the position and velocity of the satellite at some instant in time with respect to its physical parameters. In this case, the only model parameter that is being estimated is the solar radiation pressure coefficient but as previously explained there can be others.

$$\boldsymbol{S} = \left[\frac{\partial x}{\partial C_R} \quad \frac{\partial y}{\partial C_R} \quad \frac{\partial z}{\partial C_R} \quad \frac{\partial \dot{x}}{\partial C_R} \quad \frac{\partial \dot{y}}{\partial C_R} \quad \frac{\partial \dot{z}}{\partial C_R}\right]^T \tag{4.26}$$

Combining all these mathematical expressions in the correct way builds up the normal equations of a batch least-squares algorithm as shown in Equation 4.19 above. Additionally, the following workflow provides an overview of the different steps needed in a LSQ algorithm.

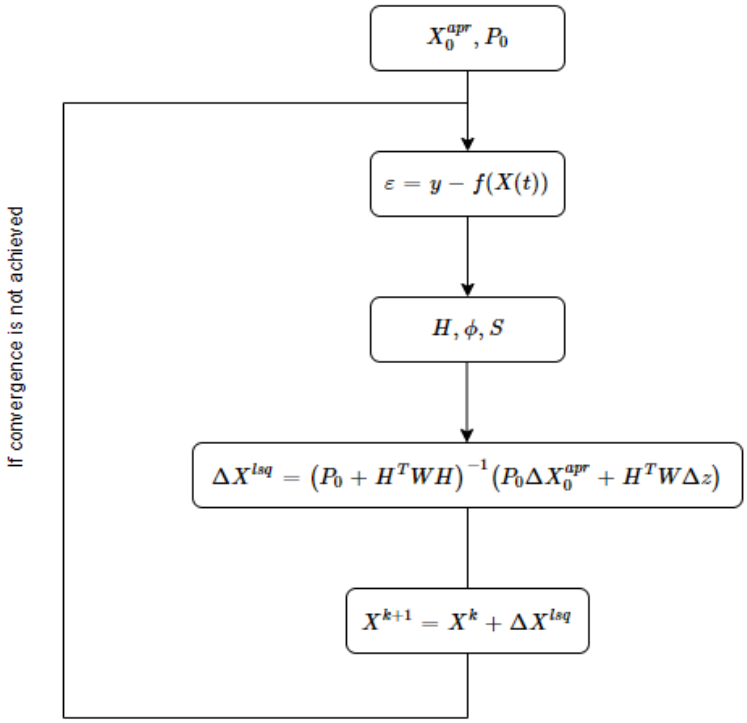

Figure 4-5. LSQ workflow

It is important to bear in mind that due to the fact that all the partial derivatives are solved by numerical integration, the algorithm might not be stable at all times. To avoid meaningless time-consuming simulations, a correct tuning of the algorithm is recommended. For instance, even though theoretically the cost function should decrease with each iteration, sometimes there is an iteration in which it can slightly increase to then keep on going down. Thus, it is advisable to set the maximum number of consecutive divergence simulation to be between 2 and 3 and not just one. Additionally, the convergence limits should be set wisely to avoid extra simulations that only add noise to the estimation of the optimum state vector and model parameters. Please note that more information on the configuration used can be found in the results Chapters 6 & 7 and Annex B in which the most representative programs of NAPEOS are reviewed.

4.4 Methodology

The main goal of this section is to provide an overview of the methodology implemented and followed in this thesis work. It mainly concerns the setting, building-up of the POD process that have been carried but there also some previous and post steps that need to be taken as well. The sections in which the methodology has been divided are mainly four: generation of reference orbits and clocks, generation of observations, absolute POD and relative POD. Even though, they will be further explained in detail, the flowchart in Figure 4-6 reviews their main functionalities, the connection between them and the order in which they have to be executed.

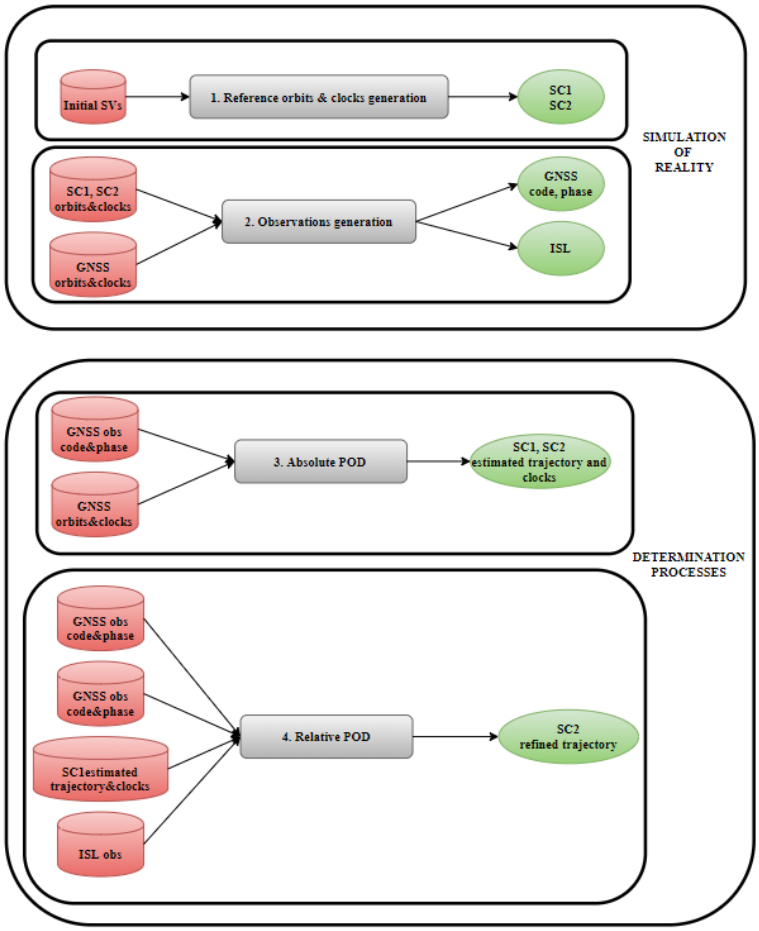

Figure 4-6. Upper-level thesis work flowchart

4.4.1 Generation of reference orbits and clocks

Due to the fact that this thesis is based on a study and not a current existing ESA mission, there is no real ephemeris or clock information. Therefore, the first main task was mainly involving the generation of orbits and clocks for both of the satellites in the constellation that can be taken as reference for the sake of this project. It is very important to mention that these orbits and clocks are generated to the best of the ability of the NAPEOS software tool and, even though they are not real data, they are assumed to represent reality.

To be able to simulate what will be assumed as real orbits of the MEO-1 and the MEO-2 satellites, 2 state vectors corresponding to a specific epoch (instant in time) were provided to us. From those initial state vectors that were propagated for a total of 180 days, three different 24-hrs orbit arcs for each of the satellites were generated to serve as reference for the set of case scenarios (1,000km, 10,000km, 20,000km) in which the POD processes will be applied. The full dynamical model used in the generation of the 6 reference orbits is shown below in Table 4-1. Please note that the most updated and modern dynamical models available were used to represent each of the forces exerted on the satellite. A detailed explanation of the dynamical model used in NAPEOS can be found in (ESA, 2009) and (Fernandez, 2019) that validates all of the information provided below.

Table 4-1. Dynamical model used in the generation of MEO reference orbits

Full Dynamical Model	
Gravity field	EIGEN.GRGS.RL04.qmp (120x120)
Gravity field (time-varying)	Drift/annual/semi-annual piece-wise linear terms up to 50x50
Third body	Sun & Moon, plus all planets in Solar System including Pluto
Precession/Nutation	IERS 2010 conventions

Pole Model	IERS 2010 conventions
Polar Motion and UT1	IERS C04 08
Atmospheric model	Considered neglected – N/A
Solar Radiation Pressure	IERS Conventions 2003 – constant area, C_R fixed to 1.0
Ocean tide model	EOT11a up to 30x30
Atmospheric tides	Ray-Ponte, 2003
Solid tide model	IERS 2003 conventions
Geoid surface	ESOC ERS-1
Reference frame	J2000 ECI
Propagator	Multi-step 8th-order Adams Bashfort

Once the orbits of MEO-1 and MEO-2 that will be taken as reference have been generated, the clocks of the transponders have to be simulated as well. The configuration used in the generation of the clocks is the same for the two satellites in all three case scenarios (three different starting dates). Thus, they would all be exactly the same if it was not for the white Gaussian noise that is added in the clocks generation process, as found in real data. It is important to mention that different seeds for the random white noise generator were used in each of the 6 clock generation processes, which therefore results in different non-ideal simulated clocks.

Table 4-2. Modelling used in the generation of the reference clocks of the MEO satellites

Receiver Clock Model	
Clock characteristics	Hydrogen
Initial second [sec]	0.0
Initial drift [sec/sec]	0.0
Frequency drift [sec/sec^2]	0.0

4.4.2 Generation of GNSS and ISL observations

In the same way that the reference orbits and clocks have to be generated, the GNSS and ISL observations are simulated. For the generation of the GNSS measurements, the inputs needed are the orbits and clocks of the MEO-1 and MEO-2 (previously generated) and the orbits and clocks of the constellations of satellites that are to be considered, GPS and Galileo in this case. The configuration used in the generation of the GNSS signals is summarized in Table 4-3 below. No ionosphere modelling has been considered in the simulation of the GNSS signals since by using the ionospheric-free combination the remainder of the error is very small. The only error considered in the measurements was white Gaussian noise. The final noise observation weights for pseudorange and carrier-phase have been included but the mathematical formulation followed in the software tool to estimate them is presented afterwards. Please note that this is the nominal configuration of the simulation and it stands unless otherwise stated.

Table 4-3. GNSS signals generation configuration

GPS/Galileo measurements		
GPS/Galileo data source		AIUB (CODE product: multi-constellation mgex)
GPS/Galileo ephemeris data		24-hr arc per file / every 5 mins
GPS/Galileo clock		24-hr arc per file / every 30 secs
Relativity correction		applied (IERS 2010)
Observations sampling / arc		30 s / 24-hr
Band-frequencies	GPS	C/A, L2C
	Galileo	E1, E5a
Observations		Iono-free – only Gaussian White noise included
Noise weight (ionospheric-free combination)		$\sigma_{code} = 1\,m$ (pseudo-range) / $\sigma_{phase} = 10\,mm$ (carrier-phase) (see mathematical formulation below)
Grazing altitude		100km
Signal-to-noise ratio cut-off		30 dB

Antenna Phase Centre Correction	applied
Antenna wind-up correction	applied
MEO satellite reference	
Center of mass (R,S,W)	$(0.75, 0.0, 0.0)$ m in satellite body-frame
Attitude model	Earth-pointing mode
Antenna reference point (R,S,W)	$(1.0, 0.0, 0.0)$ m in satellite body-frame
Antenna orientation (Euler Angles)	Nadir-oriented (0º, 180º, 0º)
MEO ephemeris and clock data	Ideally simulated orbits and clocks

The methodology followed to estimate the noise sigma of both the code and phase GNSS observations is the following one. Once these sigmas have been computed, using different seeds the noise is randomly introduced in the different set of observations following a Gaussian normal distribution.

$$\sigma_{PR} = \frac{c}{f}\sqrt{\frac{B \cdot d}{2C/N_o}\left(1 + \frac{2}{T_i C/N_o}\right)} \tag{4.27}$$

$$\sigma_{CP} = \frac{1}{2\pi}\sqrt{\frac{B}{C/N_o}\left(1 + \frac{1}{2T_i C/N_o}\right)} \tag{4.28}$$

where:

- *B* is the noise bandwidth of the filter loop (Hz)
- *d* is the correlation spacing (chips)
- *C/No* is the carrier to noise ratio (-)
- T_i is the integration time of the receiver (ms)
- *f* is the band frequency (Hz)
- *c* speed of light (m/s)

In theory, the values of these variables change depending on the band frequency in which the signal is transmitted and hence between the GNSS constellations as well. However, when it comes to NAPEOS, only one set of values can be provided and the ones corresponding to the C/A GPS frequency band have been used for code and L1 for phase observations (Table 4-4). Finally, the way to compute the corresponding carrier-to-noise ratio can be found in Chapter 5 in which the visibility results are presented.

Table 4-4. GNSS observations noise sigma generation modelling parameters

	Code range	**Carrier range**
	CA	L1
f (MHz)	1.023	1575.42
B (Hz)	0.5	0.5
T (ms)	10	10
d (chips)	0.14	-

Apart from GNSS observations, the ISL ranging measurements from one satellite to another also need to be simulated. This process is much simpler than the one in which the GNSS signals are generated because there are less variables involved. Under the assumption of a two-way range system in which the signal is transmitted by satellite 1 and travels back and forth after being reflected by satellite 2, the clock errors are ruled out of the equation and only free-space losses propagation need to be taken into account. Therefore, the way NAPEOS models these very precise ranging observations is by estimating the norm of the distance (1D) between the satellites at each of the available epochs and add white Gaussian noise to these measurements following

the state-of-the-art precision of these type of observations. According to (NASA LISA, 2019) the accuracy can get to the nanometer level but because of software limitations it was finally set at the micrometer level. The configuration followed in the modelling of these observations is shown below in Table 4-5.

Table 4-5. ISL observations modelling configuration

ISL measurements	
MEO ephemeris data	Reference ideal orbits obtained by propagation
Observation sampling / arc	1 s / 24 hr
Observations	Range – only Gaussian White noise included
Noise weight	$1\ \mu m = 10^{-6}\ m$
Minimum grazing altitude	100 km
Minimum cut-off elevation	-90 degrees

4.4.3 Absolute Orbit Determination

In order to perform a POD process, the main requirement is to have available the corresponding set of GNSS observations. In this simulation study, the propagated orbits of the MEO satellites will be taken as reference to assess the accuracy of the POD. This POD process is commonly known as absolute, since the only available measurements are between the user satellites and the GNSS constellations but there is no observation available to understand the behaviour of the relative distance between them.

The inputs needed to perform the absolute POD process are the RINEX observation files of the MEO-1 and MEO-2 satellites as well as the GNSS ephemeris and clocks and the outputs will be the orbit files and clock estimations (Figure 4-6). Additionally, and as explained in section 4.3 of this report, every POD process presents uncertainties in both dynamic models and the characterization of the satellite. Even though it has been explained previously that such inaccuracies can be overcome by the estimation of empirical accelerations, in these simulation they will not be considered, which is supported by two main reasons. First, the absolute resulting accuracies are state-of-the-art, so the inclusion of empirical accelerations would lead to unrealistic precisions in the orbit solution. Second, it is an important part of this research to assess the raw impact of individual inaccuracies and their combination in the final orbit solution.

The modelling and parametrization of the configuration of the absolute POD processes undertaken in this thesis work is outlined below in Table 4-6. Please note that highlighted in red are the parameters that present a change with respect to was used in the generation of the reference MEO orbits and shown in Table 4-1. More details will be presented in Chapter 6.

Table 4-6. Configuration of absolute POD process

Orbit determination parameters	
MEO state vectors	Position, Velocity, C_R (7 variables estimated per satellite)
MEO clocks	Estimated per epoch, every 30 s
GPS/Galileo ephemeris & clocks source	CNES (GRGS products – multi GNSS)
GPS/Galileo orbits	Fixed
GPS/Galileo clocks	Fixed
Phase ambiguity	Estimated as float per pass
Determination arc	24-hr
Observations	
Pseudo-range weight sigma	1.5 m
Carrier-phase weight sigma	10 mm
Minimum grazing altitude	100 km
Corrections applied	Center of mass, Antenna Phase Center, Antenna Phase Wind-up
Dynamical Model	

Gravity field		EIGEN-6S2ext.coef (120x120)
Solar Radiation Pressure		IERS Conventions 2003 –C_R fixed, change in cross-sectional area (difference of 0.1 m^2)
Rest of perturbations		Same as in Table 4-1
Satellite reference		
Centre of mass (R,S,W)	MEO-1	$(0.76, 0.02, -0.01)$ m
	MEO-2	$(0.74, -0.02, 0.01)$ m
Attitude model		Earth-pointing mode
Antenna reference point (R,S,W)	MEO-1	$(0.95, 0.0, 0.03)$
	MEO-2	$(1.05, 0.01, -0.03)$ m
Antenna orientation (Euler Angles)		Nadir-oriented (0º, 180º, 0º)

4.4.4 Relative Orbit Determination

After the trajectories of both MEO-1 and MEO-2 satellites have been estimated by means of their respective absolute POD processes, the last step of the process aims to improve the relative accuracy that follows from the obtained orbit solutions. This part of the research is quite innovative and therefore the methodology available was not copious. However, for the means of this thesis work the following approach has proven to yield sensible and good results, which is the reason why it was ultimately implemented.

First, it is very important to emphasize that the estimated orbits and clocks of one of the satellites, known here as MEO-1, are fixed during the relative POD process. In such a way, it is desired to make use of the high precision of the ISL observations to refine the estimated trajectory of MEO-2 and therefore improve the relative accuracy between the two satellites. On top of that, in the relative POD process, not only will the ISL observations be considered but also the code and phase GNSS measurements (previously used in the absolute POD). The fact that the GNSS measurements are also used is because since the ISL observations are 1D and do not provide information in all 3 axes, processing them alone was making the LSQ to be undetermined. Therefore, the inclusion of the code and carrier-phase observations serves the purpose of providing the algorithm more degrees of freedom to fit the very high-precision ISL observations. Since the ISL measurements are assumed to be two-way range no clocks errors need to be estimated but since they are processed along with the GNSS measurements, they are fixed to the values obtained in the absolute processing.

The uncertainties included in the absolute POD (red-highlighted in Table 4-6) are still present in this relative orbit determination process but, in this case, and in order to help fit the very precise ranging observations between the satellites, constant piece-wise empirical accelerations need to be estimated.

Table 4-7. Relative POD modelling configuration

Orbit determination parameters	
MEO-1 orbit	Fixed to estimated absolute POD results
MEO-1 clocks	Fixed to estimated absolute POD results
MEO-2 state vector	Position, Velocity, C_R, sets of empirical accelerations (re-estimated)
MEO-2 clocks	Fixed to estimated absolute POD results
Emp accelerations no. of intervals	96
Emp accelerations interval length	15.0 min
Emp accelerations reference frame	RSW
GPS/Galileo ephemeris & clocks source	CNES (GRGS products – multi GNSS)
GPS/Galileo orbits	Fixed
GPS/Galileo clocks	Fixed
Determination arc	24-hr
Observations	

Pseudo-range weight sigma		1.5 m
Carrier-phase weight sigma		10 mm
ISL weight sigma		1 μm
Minimum grazing altitude		100 km
Corrections applied		Center of mass, Antenna Phase Center, Antenna Phase Wind-up
Dynamical Model		
Gravity field		EIGEN-6S2ext.coef (120x120)
Solar Radiation Pressure		IERS Conventions 2003 –C_R fixed, change in cross-sectional area
Rest of perturbations		Same as in Table 4-1
Satellite reference		
Centre of mass (R,S,W)	MEO-1	$(0.76, 0.02, -0.01)$ m
	MEO-2	$(0.74, -0.02, 0.01)$ m
Attitude model		Earth-pointing mode
Antenna reference point (R,S,W)	MEO-1	$(0.95, 0.0, 0.03)$
	MEO-2	$(1.05, 0.01, -0.03)$
Antenna orientation (Euler Angles)		Nadir-oriented (0º, 180º, 0º)

The output of the relative orbit processing is a newly refined estimation of the orbit of the MEO-2 satellite with ideally an improved relative positioning with respect to the estimated trajectory of MEO-1.

5

Results: Visibility study

In real-life missions, GNSS observations are generally used for orbit determination of satellites placed in low-Earth orbits (LEO). In these cases and due to the geometry of the problem, the user spacecrafts are equipped with a receiver antenna that is oriented towards free-space (zenith). The selection of this orientation of the antenna is based on the fact that the difference in height of the LEO-placed satellites with respect to the GNSS constellations is quite high. Thus, this allows for a good visibility of a sufficient number of satellites at all times. However, the requirements of the study on which this thesis is based states that the satellites shall be placed in MEO orbits of nearly 7,000km altitude. This means that they will be closer to the GNSS constellations which translates in a worsening of the visibility conditions for the mentioned zenith orientation.

Thus, the main goal of this chapter is to determine which orientation of the receiver antenna provides the highest number of GNSS observations for a MEO-placed satellite. Additionally, there are some other features that play a role in the visibility conditions which have been analysed to determine which is the configuration that most optimizes the high-quality visibility conditions of both GPS and Galileo constellations.

5.1 Antenna model parameters

The visibility study has been carried out by means of a simulation study using the simulated MEO and GNSS orbits described in the previous chapter. Before presenting the results obtaind from the analysis, an overview of the different configuration used to generate such results is required. Especially important is to clearly define the antenna gain patterns of both the GNSS constellations and receiver antennas of the user satellites that were used in the simulations of the GNSS observables. Those antenna models determine in high degree the signal-to-noise ratio of the simulated observations, even though they are also influenced by other parameters like the relative position of the satellites and the path of the signal. The method employed to compute the signal-to-noise ratio is of high interest, because in these visibility study simulations this ratio has been used as a way to estimate the quality of the measurements. In fact, when generating the GNSS observables, any observation with a computed signal-to-noise ratio lower than 30 dB would be filtered out and not used. Such threshold value was chosen following the narrative found in Fernandez (2017) and it was done to ensure that all observations taken into account for the visibility analysis were of enough quality.

The expression that is employed to estimate the relationship between the signal and the noise is given below.

$$\frac{C}{N_0} = EIRP - L + \frac{G}{T} - k_B \tag{5.1}$$

where:

- C/N_0: carrier-to-noise ratio [dBW]
- EIRP: isotopically radiated power of the transmit antenna, including the directivity gain of the antenna [dB]
- L: free-space propagation losses [dB]
- G/T: receive antenna gain-to-noise temperature
- k_B: Boltzmann constant [$k_B = -228.6\ \mathrm{dB/HzK}$]

From the set of parameters listed above, it can be deducted that the carrier-to-noise ratio is mainly dependent on the properties of both the emitter and receiver antenna, along with some losses that come from the propagation of the signal in free-space and a constant. In this section of the chapter, the properties of the GPS and Galileo antennas will be described first to explain how to properly model their radiated power. Then, the impact of the receive antenna on the mentioned ratio will also be assessed following the modelling that has been chosen to represent the gain pattern of a typical antenna equipped in a MEO-placed satellite. First, the radiation power of the transmit antenna has been defined as shown in Equation 5.2 below.

$$EIRP = P_{TX} + G_{TX} \tag{5.2}$$

where P_{TX} is transmit power in dBW and G_{TX} is the directivity gain in dBW of both GPS and Galileo antennas.

Table 5-1.Properties of GPS & Gal emitter antennas (GMV, 2017)

	Maximum Directivity Gain (dBW)	Transmit power (dBW)
GPS C/A	15.0	26.8
GPS P1	15.0	26.8
GPS P2	15.0	19.7
GAL E1	16.5	35.6
GAL E5a	16.5	32.8

It is important to note that the directivity gain is not constant throughout the whole emission spectrum of the antenna. Thus, the effective isotropic radiated power of the emitter antenna will depend upon its gain pattern which also varies for different GNSS constellations, different blocks of systems and band frequencies (Fernandez, 2017). An example supporting such statement is the emission pattern of the antenna in the GPS Block IIR satellites in the L1 frequency shown in Figure 5-1 below.

Generally, an emission pattern presents one main lobe and the so-called secondary lobes that can differ in number from type of antenna to another. It can be noted how the main lobe presents a much higher signal-to-noise ratio (directivity) than the side lobes. This means that the emitted signal is still relatively powerful in the spectrum of directions that slightly deviate from the ideal one. Nevertheless, it can be seen how for high-aperture angles the signal appears to be much noisier and less powerful. Please note that the curves appearing on Figure 5-1 correspond to gain patterns for different antenna boresight angles (0-360 degrees). They are represented in the legend from 0 to 350 degrees with a gap of 10 degrees between them.

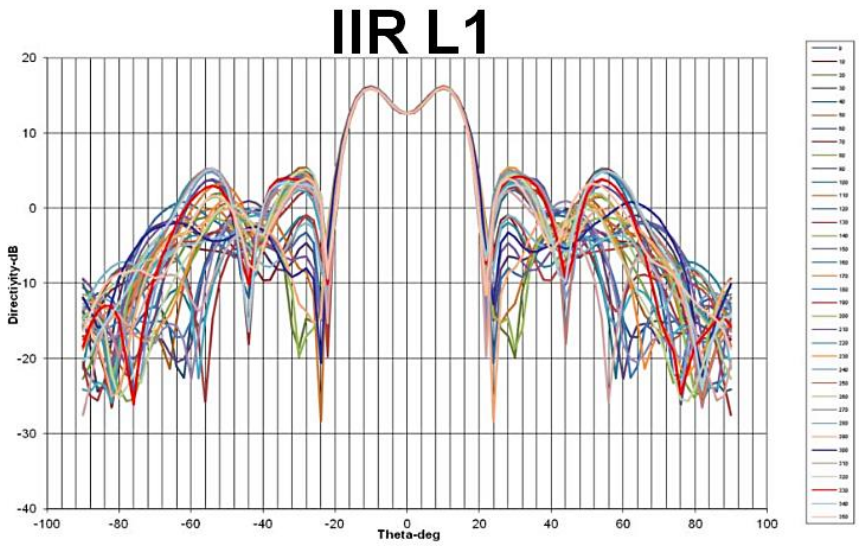

Figure 5-1. Example of an antenna pattern (from GPS L1 in a Block IIR Satellite) (Bauer, 2015)

In the software, the directivity gain patterns of the GNSS antennas have been modelled in order to reproduce to the best possible extent the real patterns of the corresponding GPS and Galileo in the given band frequencies. Please note from the graphs below that represent the way they have been modelled in the NAPEOS source code, that such patterns are an addition of 3 different functions (a constant one and 2 parabolas).

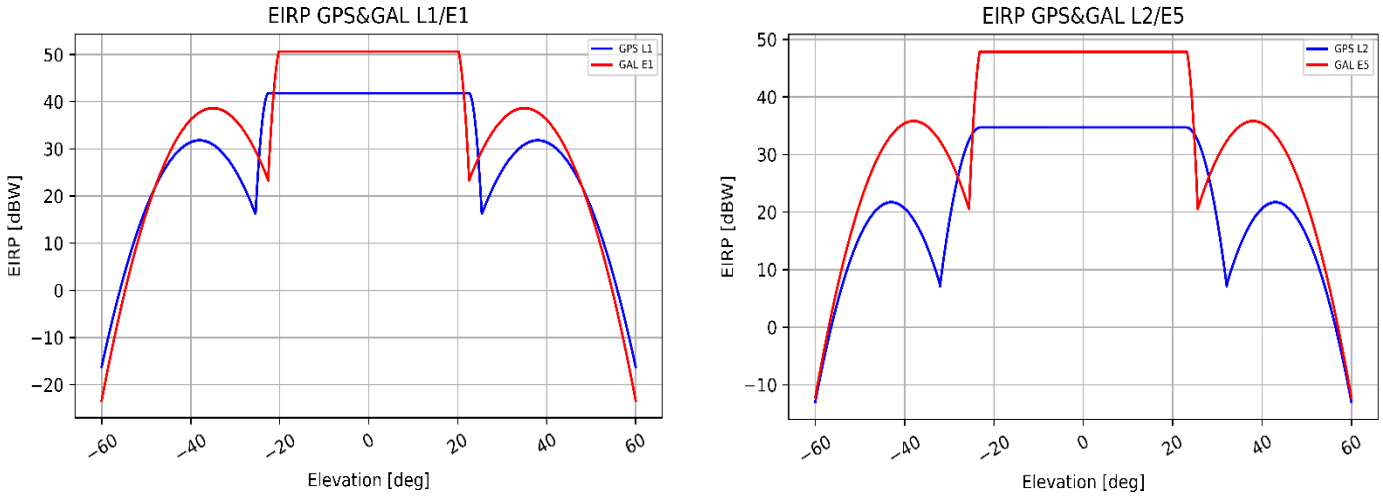

Figure 5-2. Modelled directivity gains of the GPS&GAL antennas in L1/E1 L2/E5 band frequencies

On the other hand, the gain-to-noise temperature term that appears in Equation 5.3 refers to the receive antenna. It is computed in a similar way as for the GNSS transmit antenna but in this case G_{RX} represents the receive antenna directivity gain and T the system noise temperature.

$$\frac{G}{T} = G_{RX} - T \tag{5.3}$$

It is important to bear in mind which model is being used to characterize the gain pattern of the receive antennas equipped in both satellites. As may be seen in Figure 5-3 below, generally the antennas for satellites in the LEO orbital regimes are somewhat different than those employed in GEO. For the visibility results to be presented in further sections, a LEO receiver antenna was selected for simplicity reasons. This model assumes a much smoother transition from the main to the side lobes and even though the directivity gain is lower in the zenith, it is much higher for larger elevation angles. This is supposed to be very beneficial for high orbital regimes where the

visibility of GNSS constellations is not as good as in a nominal LEO case for low elevation angles (-30 to 30deg).

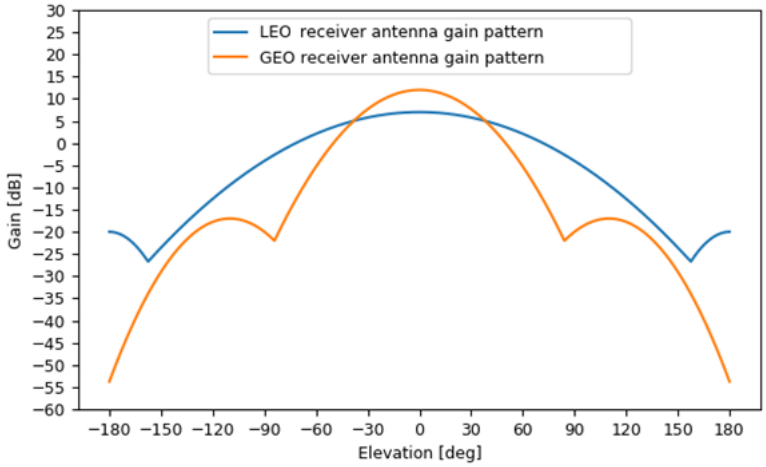

Figure 5-3.Different receiver antennas gain patterns

Regarding the losses in Equation 5.1, they come from the propagation of the signal in free-space. They might be calculated by means of the expression found below in which L_{FS} indicates the excess power loss, d represents the distance between antennas, f_c corresponds to the frequency of the signal, η is the efficiency of the antenna and c is the speed of light.

$$L_{FS} = 10\log_{10}\left[\eta\left(\frac{\pi d f_c}{c}\right)^2\right] \tag{5.4}$$

Finally, in order to include the Boltzmann constant in the same units (dBW) as the other variables in Equation 5.1, a simple conversion shall be performed. As shown in Mohr et al. (2008), the Boltzmann constant in SI units is $k_B = 1.38 \cdot 10^{-23}\, JK^{-1}$.

$$k_B = 10\log_{10}(1.38 \cdot 10^{-23}) = -228.6\ dB/HzK \tag{5.5}$$

5.2 Results

The main goal of this chapter is to perform a thorough analysis of the visibility conditions of the MEO-placed constellation of satellites to determine the optimum GNSS antenna configuration. The analysis is meant to be done in absolute terms. In this case, just one of the satellites (MEO-1) has been selected in one of the defined dates in Table 1-5 (01-01-2019 12:00:00). The results obtained in those specific conditions are representative to the other satellite and the other dates due to the fact that the analysis is done in absolute terms and not influenced by the relative distance between the satellites. The attitude mode of the satellite has been assumed as Earth-pointing, which means that it rotates along its flight component at a rate equal to the average orbital period.

In order to find the configuration that provides the highest number of observations, a nominal case was created to serve as starting point in the simulations. In this main configuration, only the main lobes of the GNSS transmit antennas were taken into account. Therefore, a Field of View (FoV) of 23.0 degrees has been considered following the modelled gain patterns presented in Figure 5-2. Moreover, a nominal value of 100km for the grazing altitude was assumed in order to filter out the signals that travel through the troposphere. The variables that remain constant throughout all simulations are the field of view of the MEO receive antennas and the carrier-to-noise ratio threshold to filter out noisy observations.

- MEO antennas FoV: 90 degrees
- Minimum C/N_0: 30 dB

Finally, the different configurations that have been object of study are the receive antenna orientation, higher emission spectrum of the GNSS transmit antenna and grazing altitude.

5.2.1 Orientation of the receiver antenna

For this thesis work, four different orientations of the antenna have been analysed: zenith, nadir, flight-vector and orbit normal. Following the reference of the satellite body frame shown in the left hand-side of Figure 5-4 below, such orientations of the antenna can be expressed as a function of the XYZ inertial reference frame.

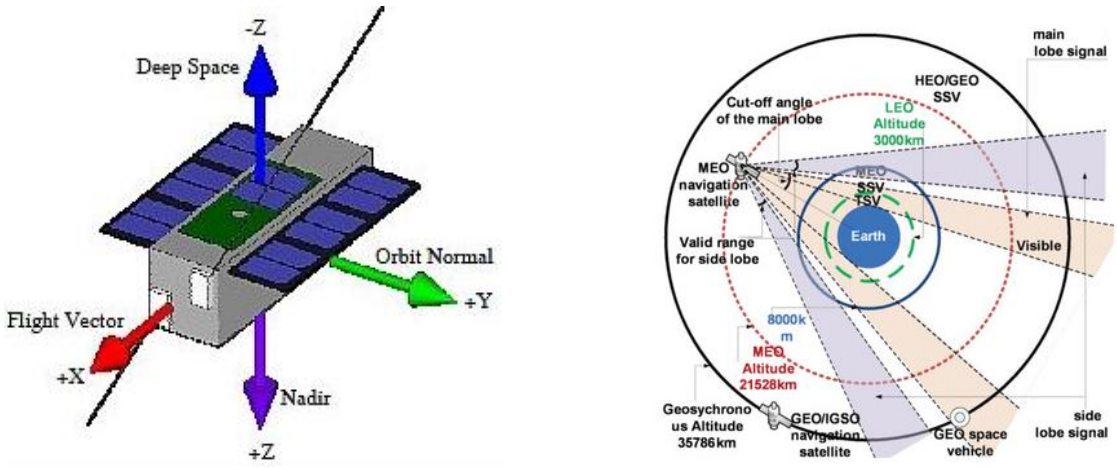

Figure 5-4. Antenna orientation possibilities (left), SSV visibility for a MEO-placed satellite (right)

In order to obtain a clearer presentation of the visibility results, the number of contacts for each of the antenna orientations have been simulated for one orbit revolution, even though the results for the whole 24 hours have also been included. They have been plotted along time in Figure 5-5 below in which the average number of visibility contacts are listed in the legend between brackets.

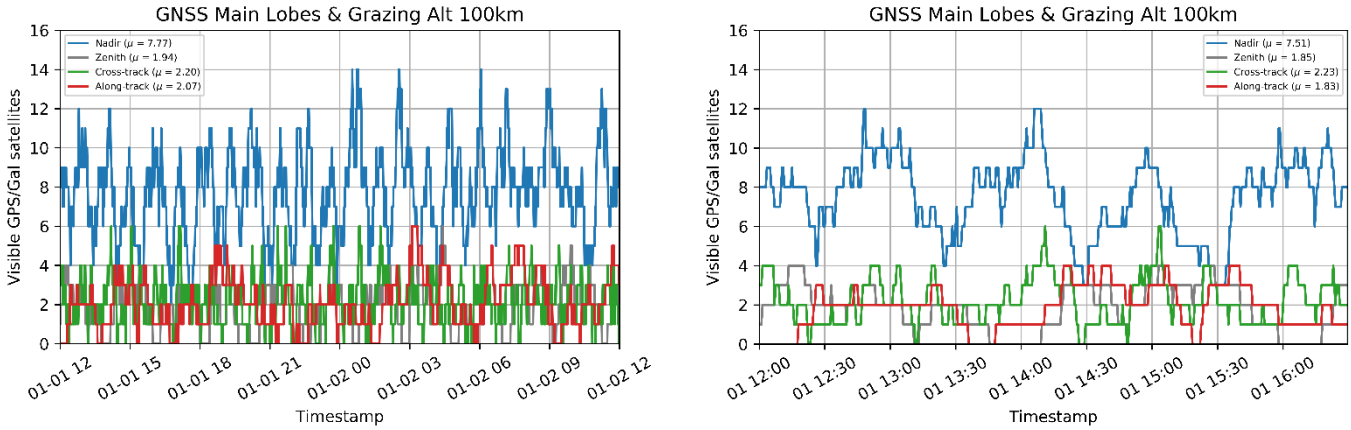

Figure 5-5. Visibility contacts for the 24hrs (left) and 4hrs (right) time periods in nominal configuration

First, it can be seen that the number of contacts for the zenith orientation are very low. As expected, the visibility for this orientation is worsened for MEO-placed satellites because of their proximity in altitude to the GNSS constellations. However, the fact that the nadir orientation is the one that yields a higher number of observations means that the best option is to look towards the Earth. In this case, even though part of the field of view is blocked by our planet, the region of space in sight from the receiver satellite standpoint is wider and more favourable to contain GNSS constellations (right-hand side of Figure 5-4). Regarding the antenna orientations in the flight vector and orbit normal directions, it is very clear from the graph that they are not good options. In these two cases, the average contacts are around 2, very similar to the zenith-pointing contacts but far from the 7.5 seen for the nadir orientation. All these conclusions are supported by the

summary of results presented in Table 5-2 in which it can be seen that a nadir oriented antenna provides visibility of at least 4 GPS and Galileo satellites during almost the entirety of the 24 hour-period. For that configuration, the maximum gap in time in which there are less than 4 GNSS satellites in sight is only 18 minutes (a dynamic orbit solution can still be obtained for those epochs).

Table 5-2. Visibility statistics for the nominal configuration

	Mean [-]	≥ 4 obs. [% of 24hrs]	Max. gap duration [min]
Nadir	7.77	97.67	17.5
Zenith	1.94	8.99	580.5
Cross-track	2.20	13.47	252.0
Along-track	2.07	14.51	469.0

5.2.2 Main & side lobes of GPS/Galileo transmit antennas

The signal power transmitted by an antenna is not the same in all directions as shown in Figure 5-1 and Figure 5-2 previously; for high-aperture angles (side lobes) the signal appears to be much noisier and less powerful. Thus, the goal of this section is to determine the impact on the visibility conditions when the side lobes of GPS and Galileo antennas are considered. The aperture angle of the emitter antenna when considering side lobes is of 60º. Additionally, it is important to bear in mind that a threshold of 30dB has been set in the carrier-to-noise ratio of the observations, which will serve as a strict filter to cancel out the too noisy measurements obtained by means of the side lobes.

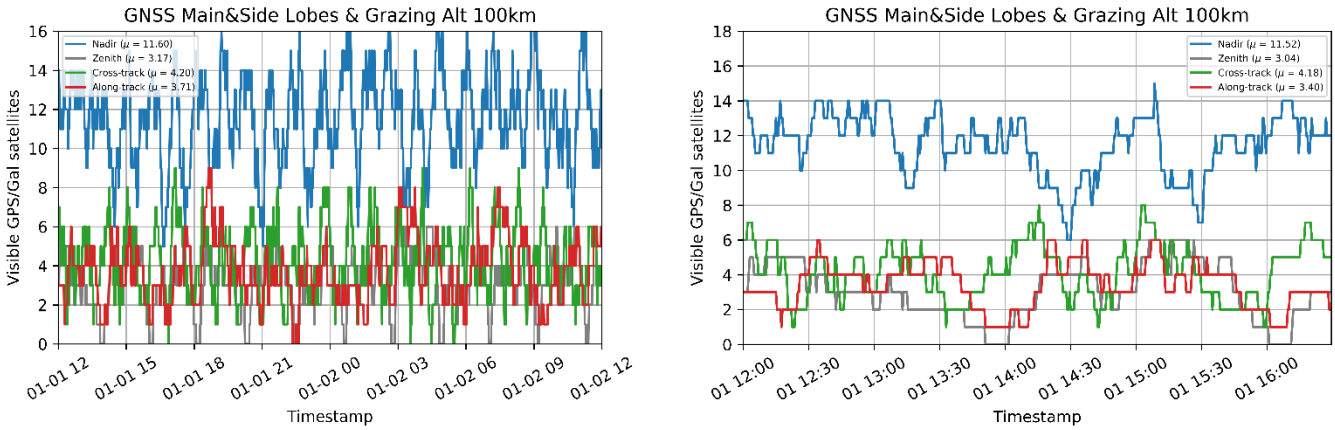

Figure 5-6. Visibility contacts for the 24hrs (left) and 4hrs (right) time periods when considering side lobes of the GNSS antennas

From both Table 5-3 and Figure 5-6 it can be seen that there has been an increase on the number of contacts in all orientations. For a nadir-pointing receiver antenna, the increment has been higher (~4) than for the other orientations (~2). Moreover, with the consideration of the side lobes, there are at least four GPS/Galileo satellites in sight for the whole 24-hour period; there is continuous visibility. For the other orientations, even though the number of observations have also increased, the visibility conditions are still significantly worse. Only in the cross-track component the contacts mean is higher than 4 but with huge time gaps that go up to around 2 hours in which there are not more than 3 satellites in sight. It can be concluded that it is advisable to consider both main and side lobes of the GNSS antennas, especially if having a strict threshold for the carrier-to-noise ratio which erases the less powerful and noisy signals that might arise from this configuration.

Table 5-3. Visibility statistics when considering side lobes of the GNSS antennas

	Mean [-]	≥ 4 obs. [% of 24hrs]	Max. gap duration [min]
Nadir	11.60	100.00	0.0
Zenith	3.17	44.26	142.5
Cross-track	4.20	62.86	47.0
Along-track	3.71	51.65	118.5

5.2.3 Grazing altitude

Especially in a nadir-pointing antenna configuration but also applicable to cross-track and along-track orientations, the signal will travel from one side of the Earth to another as shown in Figure 5-7 below. The specific path will depend on the relative position of the GNSS and user satellites, in which the signal will gradually get closer and then further away from our planet. To ensure that no signal can get nearby Earth's surface at any point during the transmission, a minimum grazing altitude has been set. Depending on the chosen value for the minimum distance, different errors that generally affect the signal will not be present. For this thesis work, two different case scenarios have been considered: 100 and 1,000km.

The nominal configuration assumes a grazing altitude of 100km, which filters out any signal affected by the delay caused by the particles found in the different layers of the troposphere. However, the troposphere is not the only region of the atmosphere that affects the transmission of a GNSS signal. The ionosphere, which extends up to 1,000km in height, is also responsible for diffracting the signal. Such diffraction translates into the signal travelling a longer path and in the case of the ionospheric delay it is very hard to eliminate it completely. There is an analytical method, known as ionosphere-free combination of dual-frequency observations, that helps filtering out 99.9% of the ionospheric error of any observation available in two different frequencies. However, in other cases such as 1F observations in which it can be very hard to obtain a precise estimation of the ionospheric error. To account for such cases, it has been analysed how much would the loss be in visibility contacts if the grazing altitude was increased from 100km to 1,000km. Under these circumstances all observations can be considered to be free from the error that the ionosphere induces in the signal.

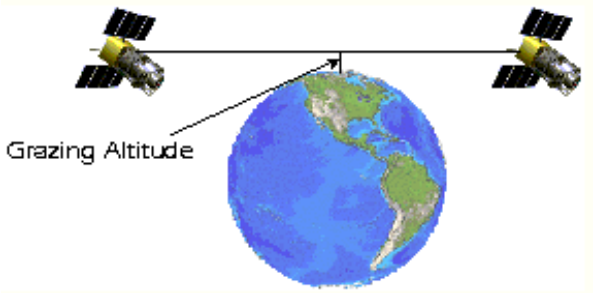

Figure 5-7. Concept of grazing altitude

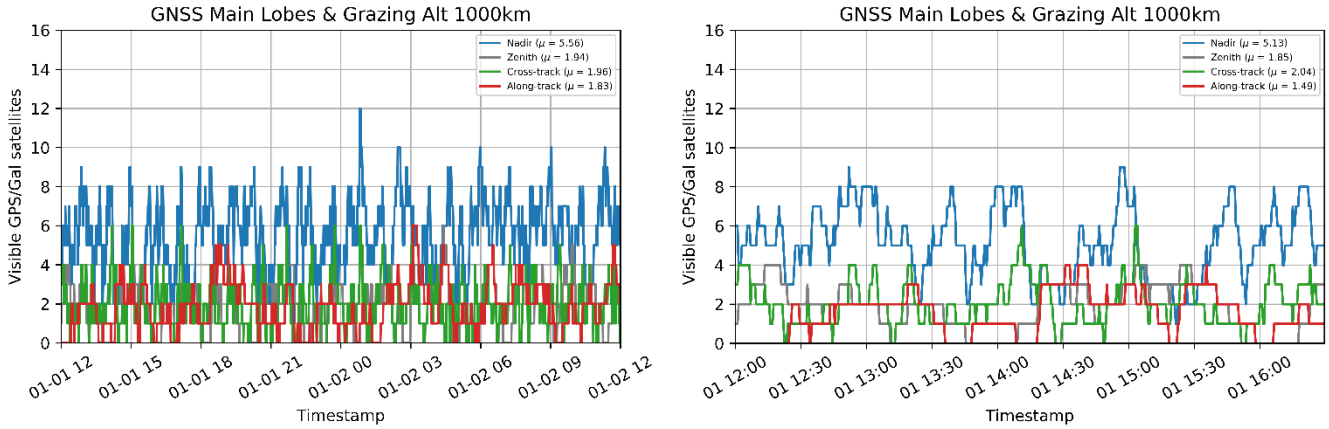

Figure 5-8. Visibility contacts for the 24hrs (left) and 4hrs (right) time periods for a grazing altitude of 1,000km

Table 5-4. Visibility statistics for a grazing altitude of 1,000km

	Mean [-]	≥ 4 obs. [% of 24hrs]	Max. gap duration [min]
Nadir	5.56	85.46	31.0
Zenith	1.83	8.99	580.5
Cross-track	1.96	9.68	252.0
Along-track	1.94	9.20	475.0

The results of the simulations are shown in Figure 5-8 and Table 5-4 above. As expected, the number of visibility contacts has decreased in general terms with the nadir orientation being the one that has been more affected. Due to the geometry of such case scenario, the signal travels from one side of Earth to the other and therefore it often traverses the ionosphere. Because of that, the mean of observations has gone down to 5.5 and so has the percentage coverage that is now situated in around 85%; the maximum data gap duration has also increased. On the other hand, the zenith-orientation has not been affected by this change in configuration since the satellite is always looking towards free-space. In our case, being at 7000km altitude, and using 90º of maximum co-elevation, the received signal using zenith-pointing cannot cross the ionosphere, no matter how much is the beam width of the emitter increased. Finally, for the along-track and cross-track orientations the decrease in number of observations and percentage of coverage has gone down but not dramatically. For these orientations, the signal travels in perpendicular planes to the one previously shown in Figure 5-7 and only for certain geometries of the relative position between the satellites will the signal get close to Earth.

5.2.4 Optimum configuration

As proven in previous sections of this chapter, the antenna orientation that yields a higher number of visibility contacts with the GPS and Galileo satellites is nadir. Additionally, if considering a high aperture angles in the emission spectrum of the GNSS antennas the visibility conditions are improved since the number of high-quality observations is increased. For the grazing altitude, it is advisable to set it at 100km to avoid tropospheric effects which are hard to model precisely. In cases in which the visibility conditions are very favourable, increasing the value of the grazing altitude up to 1,000km could be a viable option. It is also important to mention that this analysis has been carried out assuming that the MEO antennas only are able to receive signals in one direction. However, if there was the possibility to equip the satellite with omnidirectional antennas, the following results would be obtained. It can be noted in Figure 5-9 below that the visibility contacts are exactly the same for an omnidirectional antenna (nadir, zenith, along, cross) as for the combination of 2 unidirectional antennas oriented towards nadir and zenith. Therefore, it can be concluded that the final effect is similar to including just two antennas, which has proven to be the best approach. Please bear in mind that omnidirectional and multiple antennas have only been considered for means of this visibility study but will not be used for further analysis.

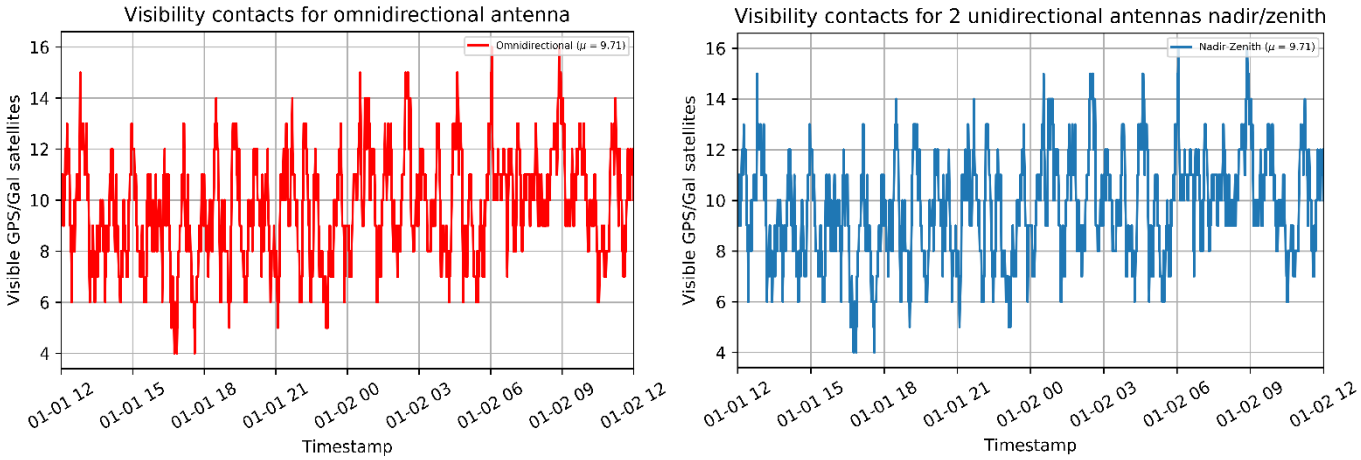

Figure 5-9. Difference in visibility contacts for an omnidirectional antenna and a nadir/zenith one

5.2.5 Relative visibility

In the past sections of the chapter, the visibility has been studied in absolute terms. However it is also important to examine the conditions of relative visibility for the three different scenarios previously defined. The idea is to be able to determine how many GPS and Galileo satellites are in sight for both MEO-1 and MEO-2 when they are close, in mid-range and far away. If the number of common GNSS satellites was high as generally happens to satellites in close formation flying, the double differences technique could be applied to the measurements to cancel out the carrier-phase ambiguity fixing. It would translate into a more accurate relative positioning (Guo, 2019). The configuration of these simulations includes one nadir-pointing antenna, a grazing altitude of 100km and an emitter antenna aperture angle of 60º to consider side lobes.

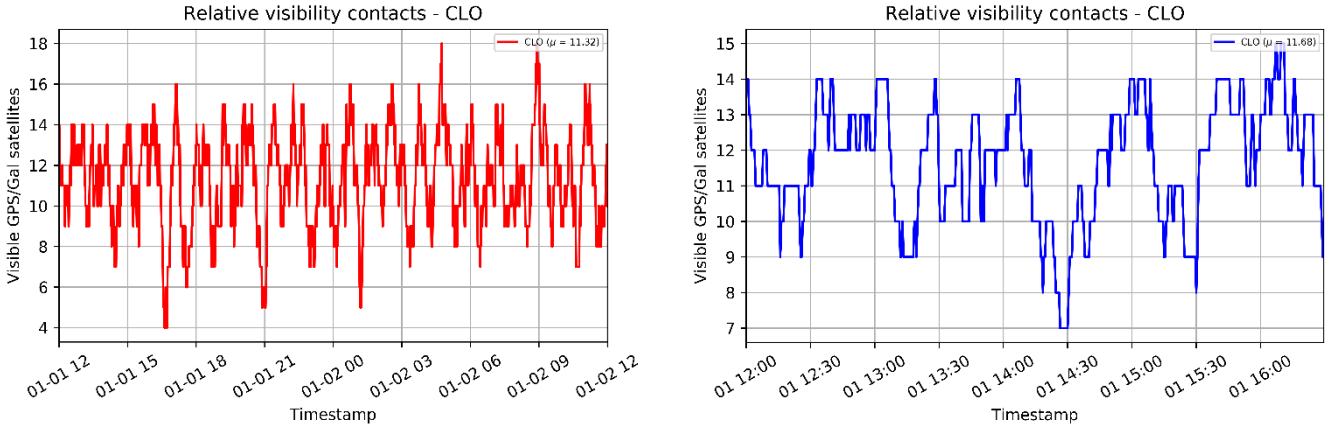

Figure 5-10. Relative visibility contacts CLO scenario

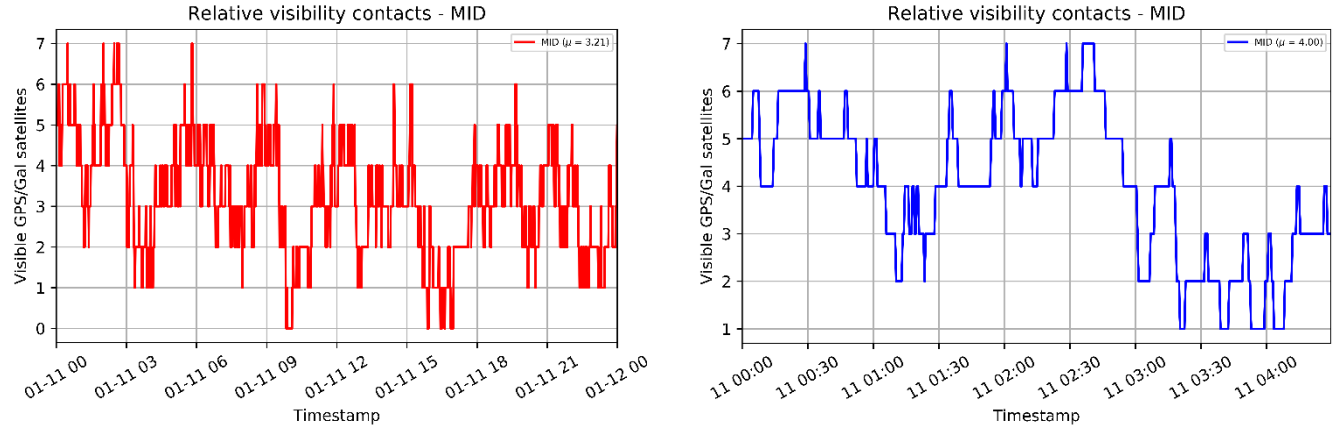

Figure 5-11. Relative visibility contacts MID scenario

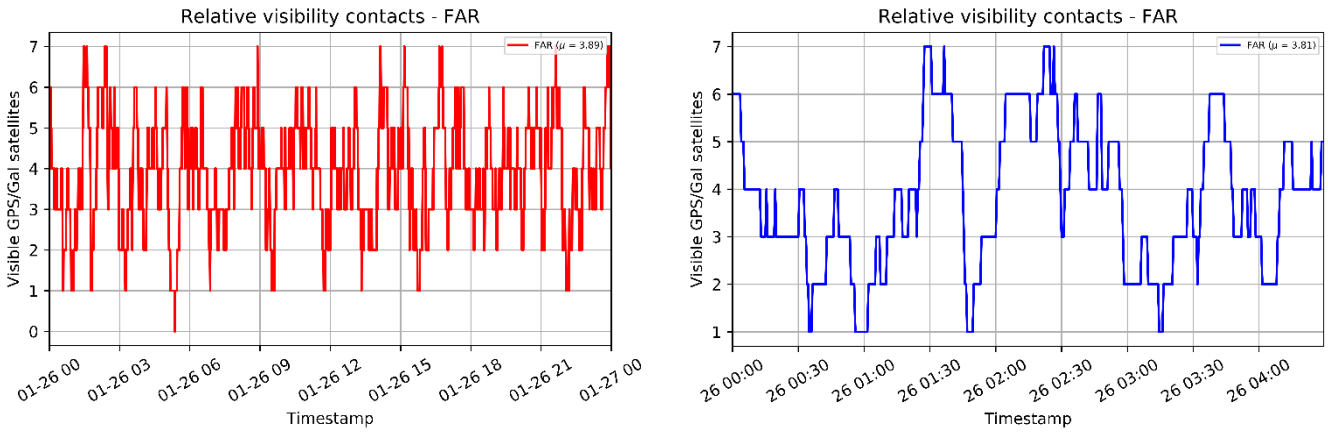

Figure 5-12. Relative visibility contacts FAR scenario

As could be expected, the number of common contacts is much higher when the satellites are close to each other (1,000km) since they share most part of their field of view (Figure 5-10). However, when the distance between them is in the range of 10,000km to 20,000km the relative visibility conditions are much worsened. The mean of common contacts goes down from 11 to around 3 (Figure 5-11 and Figure 5-12). Therefore, it has been proven that it is impossible to benefit from the advantages of implement double differences on the measurements of the 2 satellites when their relative distance is beyond 10,000km.

6

Results: Absolute POD

In this chapter the absolute POD results are presented and analysed. First, the validation of the software will be performed by means of error-free simulations of all three defined case scenarios in which the goal is to obtain orbit solutions of both MEO satellites that are as similar as possible to the propagated ones, considered as reality. Then, different realistic sources of error will be generated in order to assess their impact on the absolute orbit solution. In order to perform a thorough study, several sets of Monte-Carlo simulations have been performed for each of the examined sources of error to provide the reader with a more global analysis. Finally, the sources of error examined are set to a sensible and realistic value or model (depending on their nature) and the absolute orbit solution that follow from such configuration are presented and analysed. These perturbed orbits will be the starting points for the relative orbit determinations that will be reviewed in Chapter 7 of this document.

6.1 Validation

The validation results of the absolute POD processes is presented in this section. The main objective is to assess the correct functioning of the software when performing an orbit determination process of a MEO-placed satellite by means of observations from GNSS constellations (GPS and Galileo in this specific case). The NAPEOS software is routinely used and already properly validated so the focus is set at the generation of the simulated GNSS observations. The final goal is to obtain reconstructed orbits that are as representative as possible of reality. Thus, the idea is to run a complete error-free absolute POD simulations in all three specified case scenarios (CLO, MID, FAR) and for both MEO1 and MEO2 satellites and compare the resulting orbits with the propagated ones, which for the purpose of this project they represent the real satellite's trajectories. Hence, the configuration used in validation test cases is presented in Table 6-1 below.

Table 6-1. Specifics of ideal configuration – referenced to body frame

Orbit determination parameters	
MEO state vectors	Position, Velocity, C_R (7 variables estimated per satellite)
MEO clocks	Estimated per epoch, every 30 s
GPS/Galileo ephemeris & clocks source	AIUB (CODE products – multi GNSS)
GPS/Galileo orbits	Fixed
GPS/Galileo clocks	Fixed
Phase ambiguity	Estimated
Determination arc	24-hr
Observations	

Pseudo-range weight sigma		0 (error-free)
Carrier-phase weight sigma		0 (error-free)
Minimum grazing altitude		100 km
Corrections applied		Center of mass, Antenna Phase Center, Antenna Phase Wind-up
Dynamical Model		
Gravity field		EIGEN.GRGS.RL04.qmp (120x120)
Solar Radiation Pressure		IERS Conventions 2003 –C_R fixed, cross-sectional area
Rest of perturbations		Same as in Table 4-1
Satellite reference		
Centre of mass (R,S,W)	MEO-1	$(0.75, 0.00, 0.00)$ m
	MEO-2	$(0.75, 0.00, 0.00)$ m
Attitude model		Earth-pointing mode
Antenna reference point (R,S,W)	MEO-1	$(1.00, 0.00, 0.00)$ m
	MEO-2	$(1.00, 0.00, 0.00)$ m
Antenna orientation (Euler Angles)		Nadir-oriented (0º, 180º, 0º)

In the following figures and tables, the goal is to present the results in the most efficient way possible. To do so, the solution obtained by means of the orbit determination process is compared against the real propagated one for the two MEO satellites in all 3 case scenarios (CLO, MID, FAR). The accuracy of the orbit solution will be compared in position for all body frame components (radial, along-track, cross-track). Additionally, the observation residuals in both code and phase corresponding to the GPS and Galileo constellations are graphically and numerically represented. Finally, the estimated solar radiation pressure coefficient for both satellites in all three case scenarios is also shown as it is the only model parameter that is estimated along with the state vector. Generally, the closer the estimated value is to the real value used in propagation (1.0), the more accurate the reconstruction of the orbit will be.

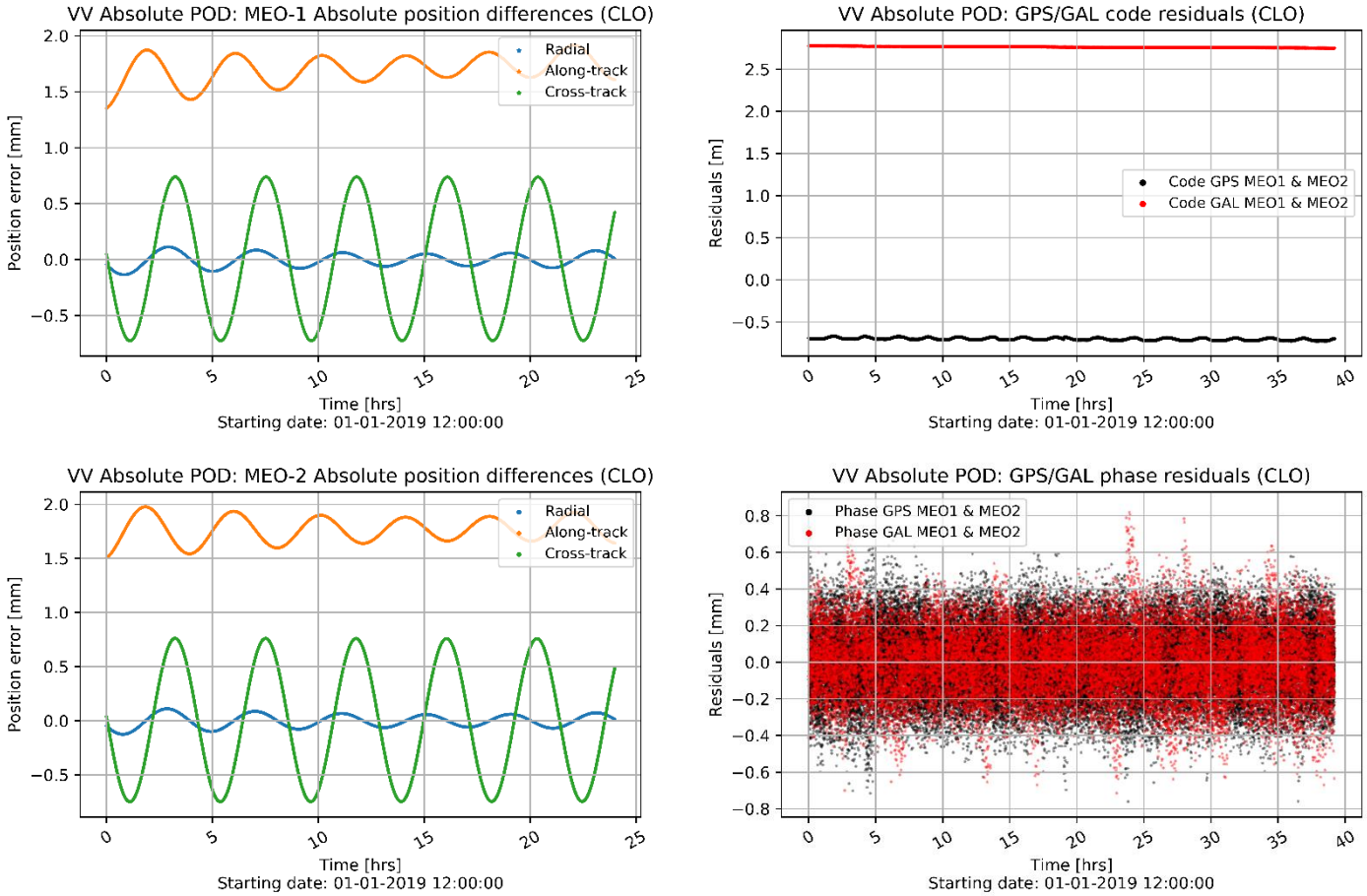

Figure 6-1. Absolute position differences and GNSS observations (code, phase) residuals (Validation, CLO)

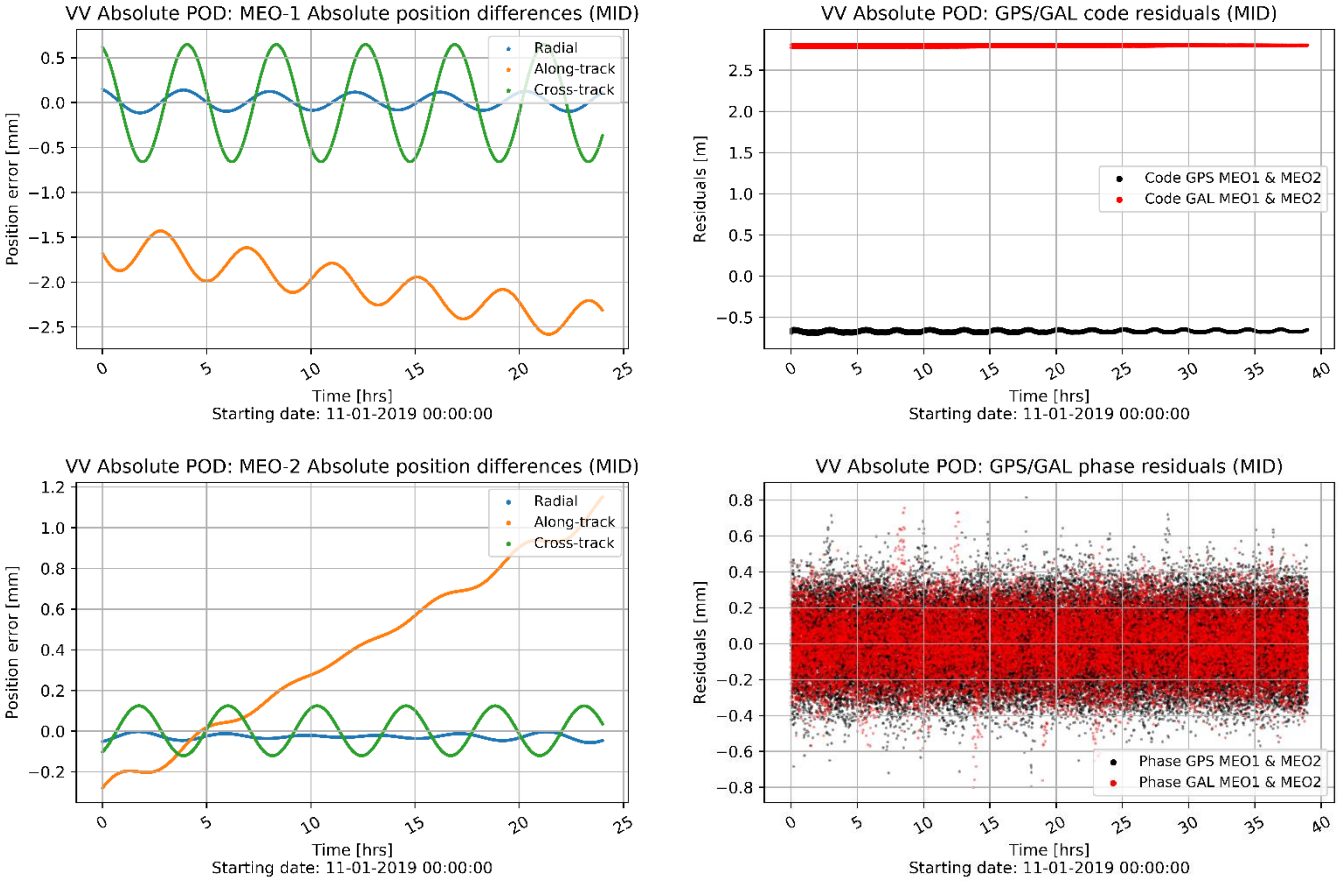

Figure 6-2. Absolute position differences and GNSS observations (code, phase) residuals (Validation, MID)

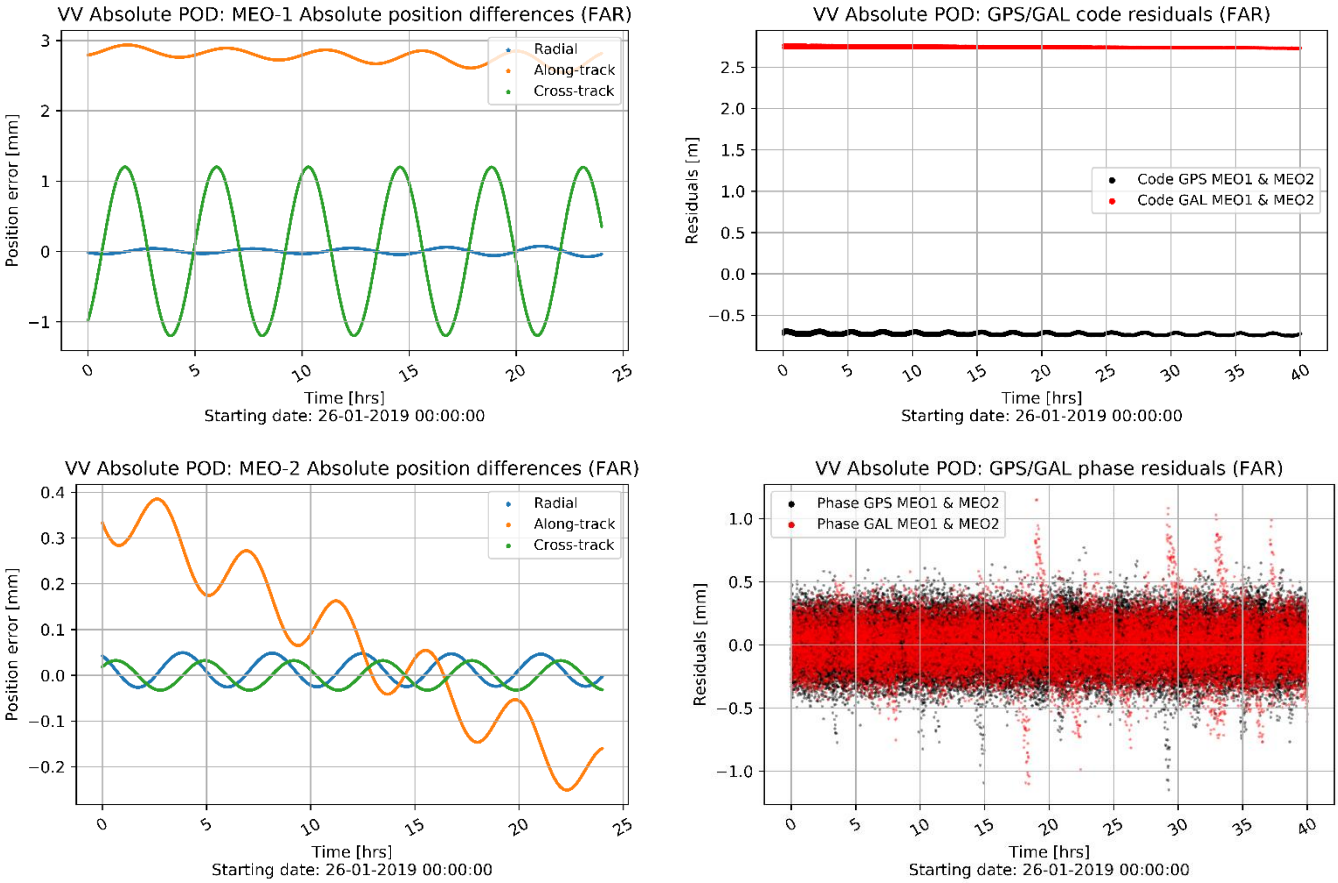

Figure 6-3. Absolute position differences and GNSS observations (code, phase) residuals (Validation, FAR)

Table 6-2. Summary of the validation results (position only)

Scenario	Satellite		Radial [mm]	Transverse [mm]	Cross [mm]	Total 3D [mm]	Typical RMS [mm]
CLO	**MEO-1**	RMS	0.06	1.71	0.51	1.78	1.03
	MEO-2	RMS	0.06	1.77	0.53	1.85	1.07
MID	**MEO-1**	RMS	0.08	2.04	0.46	2.09	1.21
	MEO-2	RMS	0.03	0.56	0.09	0.57	0.33
FAR	**MEO-1**	RMS	0.04	2.78	0.85	2.90	1.68
	MEO-2	RMS	0.03	0.19	0.02	0.20	0.11

Table 6-3. Summary of GNSS residuals for all validation tests

Scenario	Satellite	GPS code observations				GPS phase observations			
		Total	Rejected	Mean (m)	RMS (m)	Total	Rejected	Mean (mm)	RMS (mm)
CLO	MEO-1	22796	0	-0.70	0.70	22796	0	0.00	0.18
	MEO-2	22874	0	-0.70	0.70	22874	0	0.00	0.19
MID	MEO-1	22897	0	-0.68	0.68	22897	0	0.00	0.19
	MEO-2	23489	0	-0.66	0.66	23489	0	0.00	0.17
FAR	MEO-1	22509	0	-0.72	0.72	22509	0	0.00	0.20
	MEO-2	23403	0	-0.73	0.73	23403	0	0.00	0.17
Scenario	**Satellite**	**GAL code observations**				**GAL phase observations**			
		Total	Rejected	Mean (m)	RMS (m)	Total	Rejected	Mean (mm)	RMS (mm)
CLO	MEO-1	12439	0	2.76	2.76	12439	0	0.00	0.18
	MEO-2	12488	0	2.76	2.76	12488	0	0.00	0.18
MID	MEO-1	11985	0	2.79	2.79	11985	0	0.00	0.18
	MEO-2	11814	0	2.81	2.81	11814	0	0.00	0.15
FAR	MEO-1	12658	0	2.75	2.75	12658	0	0.00	0.21
	MEO-2	13506	0	2.73	2.73	13506	0	0.00	0.15

Table 6-4. Estimated solar radiation pressure coefficients

Scenario	Satellite	SRP
CLO	**MEO-1**	0.999910357
	MEO-2	0.999922172
MID	**MEO-1**	1.00006590
	MEO-2	0.999976957
FAR	**MEO-1**	0.999970657
	MEO-2	1.00000250

Focusing on the figures in which the absolute position differences are plotted (upper and lower-left of Figure 6-1, Figure 6-2 and Figure 6-3), it can be seen that for both satellites in all three case scenarios the radial and cross-track components present a non-biased oscillatory behaviour with an amplitude in the sub-millimetre level. On the other hand, the position differences in the along-track component are not quite as precise as for the other two but still lie within the [-3,3] mm range. Obtaining position errors of a very few mm in 3D can be expected for test simulations in which all errors are turned off, even the addition of noise in the GNSS observations.

The residuals of both GPS and Galileo phase observations are in the [-0.5,0.5] mm range (Table 6-3), which is probably due to the truncated accuracy in the mm level of the GNSS ephemeris data (in sp3 files). Additionally, it can be noted a bias between the code residuals of both GPS and Galileo constellations in all validation tests (upper and lower-right of Figure 6-1, Figure 6-2 and Figure 6-3). This can be explained by the fact that they present different time systems, in which the GPS clocks are aligned at 0 but the Galileo ones present an offset that derives into the mentioned bias. This only happens to the code observations since they are absolute and not to the phase ones whose residuals are non-biased due to the ambiguity of the measurements. To eliminate the bias in the pseudo-range residuals an intersystem bias could have been estimated. However, due to limitations of the software if the intersystem bias was estimated, the RMS of the

Galileo observations increased significantly and became too noise. That is why such intersystem bias was not included in the end. Further research in the near future to address this limitation is required. Finally, and as shown in Table 6-4, the solar radiation pressure of both MEO-1 and MEO-2 satellites in all scenarios have been estimated to have differences with respect to the true value of less than 0.0001, which is also representative of the high accuracy obtained in the orbit determination solutions.

In general terms, it can be assumed by looking at the previously presented and analysed results that the software has been validated and that the results that may follow from more realistic configurations can be taken as realistic. In the next section, different sets of realistic errors will be generated to assess their influence in the orbit solution of a more realistic absolute POD process.

6.2 Generation of error sources

In real life, when a POD process is performed, there are systematic and random errors that affect the error solution. The systematic errors are those that are always present and that impact the orbit solution in a constant or regular way, difficult to quantify initially. The random errors are unpredictable and very hard to predict beforehand. In this section, the main of goal is to present the different sources of error that have been included in the orbit determination processes carried out in this thesis study, in order to obtain realistic POD results. These errors are generally found as inaccuracies in the satellite model, uncertainties in the dynamic models, precision of the clocks and ephemeris data of the GNSS constellations in use and errors in the GNSS observations.

The way to assess the influence of these errors on the accuracy of the absolute POD process has been by means of Monte Carlo tests in which five variables are randomly modified following a normal distribution for the given values of mean and standard deviation. The error sources that have been object of study are the following: satellite centre of mass, antenna reference point, satellite area, uncertainties in the geopotential model and inaccuracies in GNSS ephemeris and clocks. In that regard, out of the total 5 sources of error that will be analysed in this thesis, there are 3 that allow to such type of approach: centre of mass, antenna reference point and area. Thus, these variables were given a reference value that was used in the generation of the real orbits and in the validation of the absolute POD process previously presented. For the purpose of this section, the reference values were introduced as mean in the normal distribution and a realistic selected value of standard deviation was used to perturb them from their reference values. Such standard deviation values had to be as realistic as possible and were selected with the help of references like Berruti and Banos (2016) and by means of trial and error simulations as well. The three-dimensional variables like centre of mass and antenna reference point have been independently varied in all their components while the cross-sectional area was modified in its only dimension (50 samples each time). They are all listed below in Table 6-5, in which the geopotential model and GNSS clocks and orbits are presented with their corresponding perturbed model and source respectively. The selection of the perturbed geopotential models (two) and GNSS ephemeris data and clocks (one) was based on their accessibility and compatibility with the NAPEOS software.

Finally, please note that these generation of errors and Monte Carlo tests have only been applied to the MEO-1 satellite in the starting date and determination arc that correspond to the CLO scenario (01/01/2019 12:00:00 UTC). These results will be later on analysed globally and could in principle be interpolated to some extent for the case of the MEO-2 satellite at another starting date but they have to be treated carefully.

Table 6-5. List of all errors introduced in the Absolute POD simulations: reference and perturbed values

		Ideal case[1]	σ (3 axes)	Perturbed model/source
MEO-1	**Centre of mass (R,S,W)**	(0.75, 0.00, 0.00) m	0.02	
	Antenna reference point (R,S,W)	(1.00, 0.00, 0.00) m	0.05	
	Area	5.0 m^2	0.1	

[1] Propagation of MEO-1 orbits & generation of GNSS signals

Geopotential model	EIGEN.GRGS.RL04.qmp	-	EIGEN.GRGS.RL03.v2 EIGEN-6S2.ext
GNSS clocks & eph source	AIUB/CODE	-	CNES/GRGS

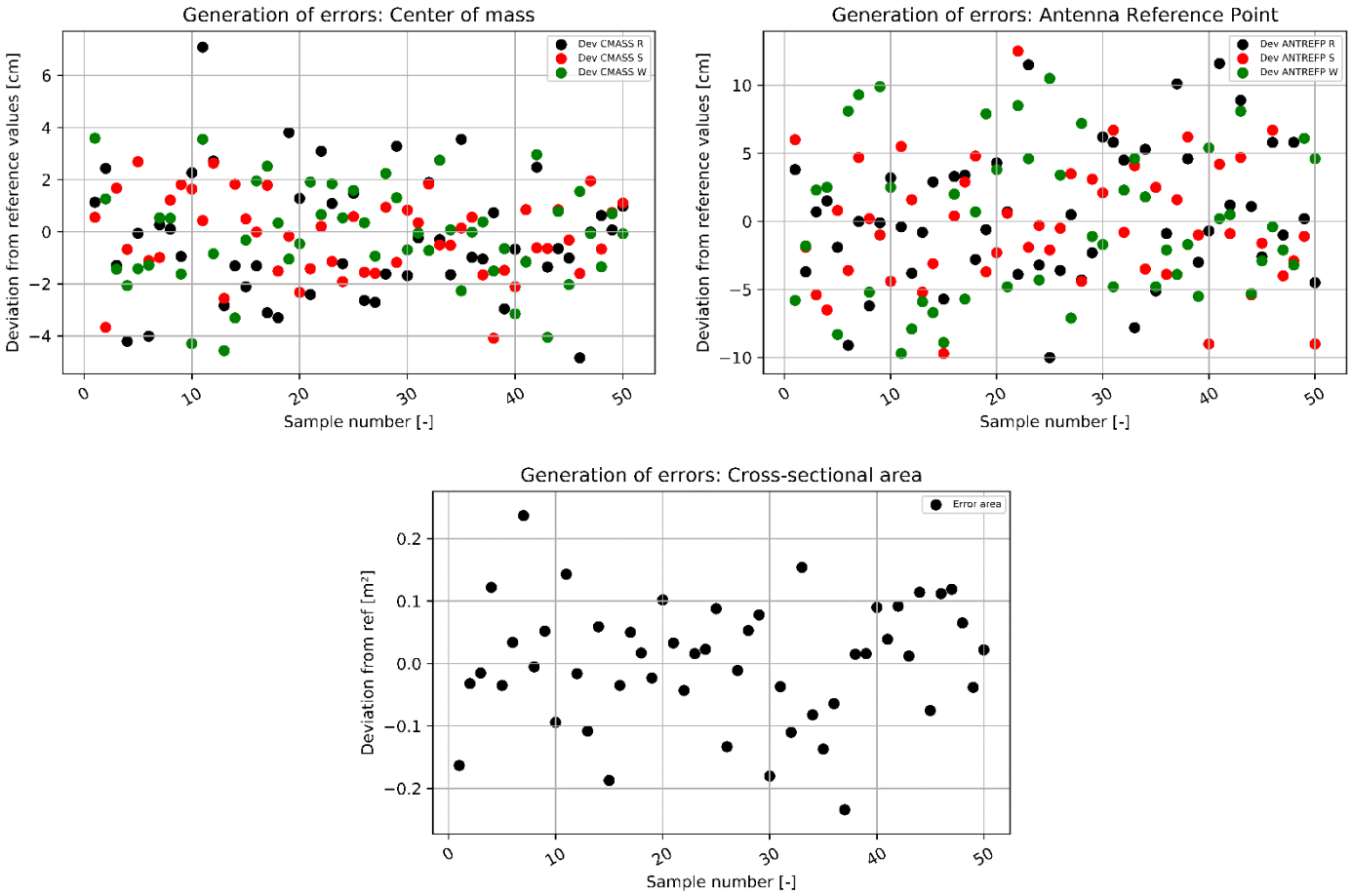

Figure 6-4. Generation of errors by means of normal distribution of centre of mass (upper-left), antenna reference point (upper-right) and area (bottom)

6.3 Impact of error sources

In this section, the impact of the error sources previously generated is assessed. In order to do a thorough and meaningful analysis of the results, the following approach will be followed. First, the impact of the sources of error will be examined in terms of the 3D error that they introduced in the orbit solution of the absolute POD. Along with that, the estimation of the solar radiation pressure coefficient will also be shown in order to assess how much of the total error this model parameter absorbs and how much it is correlated with each of the different introduced sources of error. Then, the error sources that have the largest impact on the final 3D orbit solution are analysed in terms of the impact they have on each of the body-frame orbit components: radial, along-track and cross-track.

6.3.1 Absolute impact on orbit solution

First of all, the influence of a perturbation on the different components of the centre of mass is examined. Then, the impact on the absolute orbit solution of an uncertainty in each of the axes of the antenna reference point is reviewed. Continually, an inaccuracy on the area of the satellite is assessed to understand how much it affects the accuracy of the predicted trajectory. Additionally, uncertainties in the geopotential model can lead to big errors in the absolute positioning and two different models have been examined. Finally, the use of different clocks and ephemeris data from the GPS and Galileo constellations from what was used to generate the code and phase

observations is analysed. In all cases, the predicted SRP coefficient is also shown to understand how much it is coupled with each of the error sources being tested.

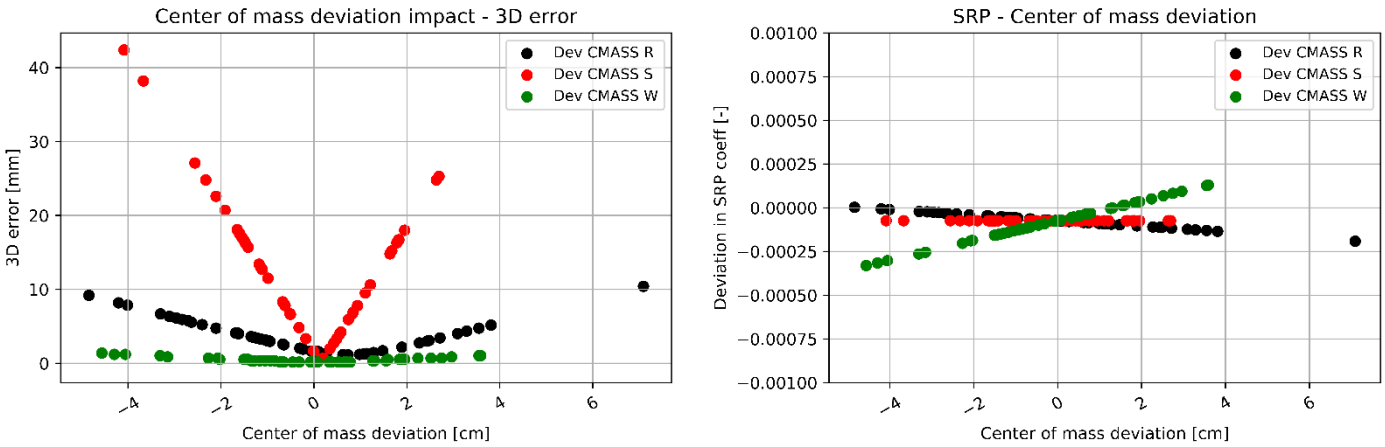

Figure 6-5. 3D error and SRP for different deviations in the center of mass

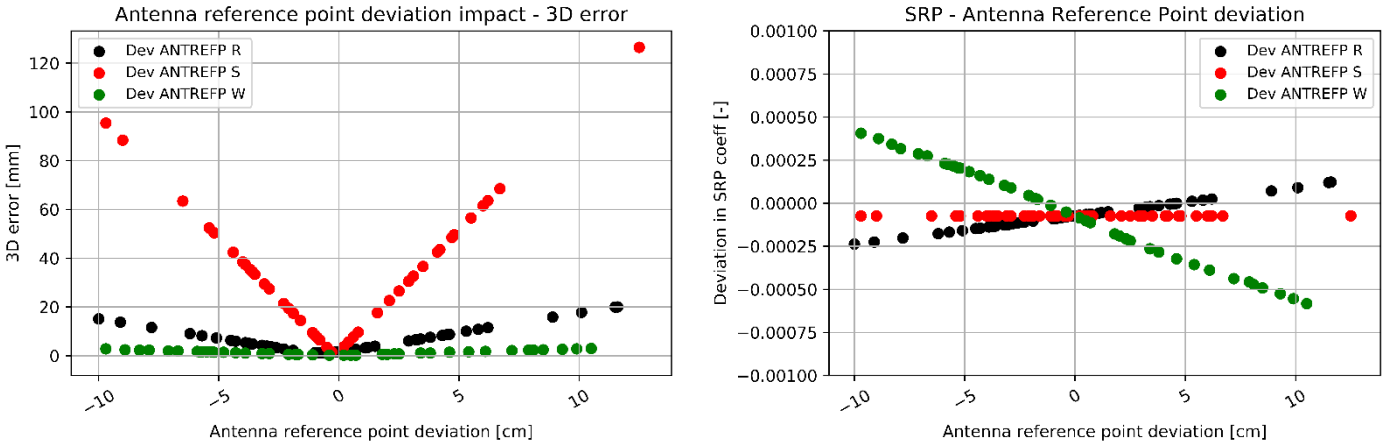

Figure 6-6. 3D error and SRP for different deviations in the antenna reference point

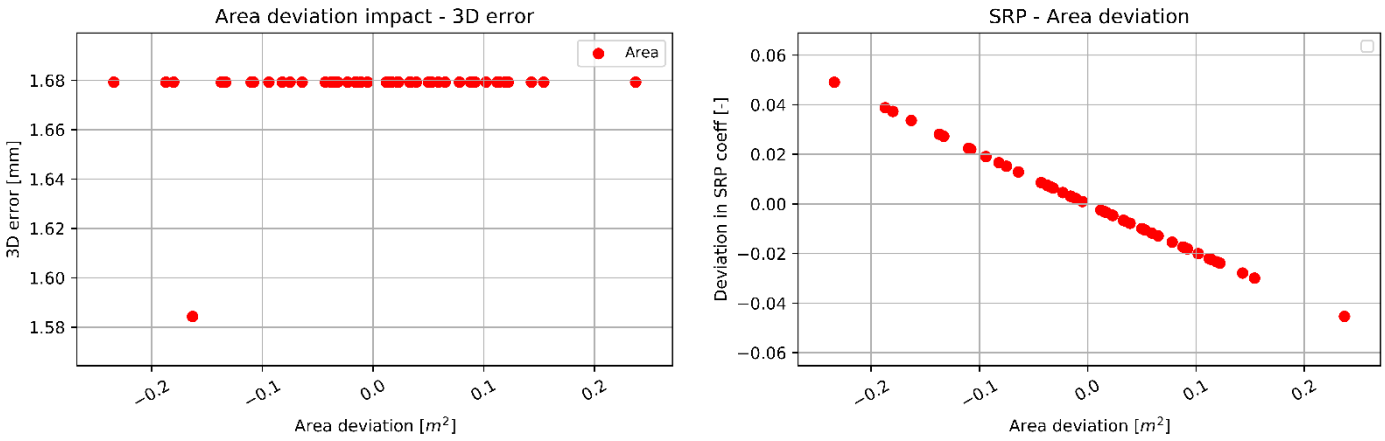

Figure 6-7. 3D error and SRP for different deviations in the cross-sectional area

Table 6-6. 3D error in the orbit solution for uncertainties in the geopotential model and inaccuracies in the GNSS orbits and clocks

		3D orbit error [mm]	ΔC_R [-]
Geopotential model	EIGEN-6S2ext	3.2	0.000696
	EIGEN.GRGS.RL03	2.7	-0.00026
GNSS Ephemeris & clocks		12.5	-0.00235

Following the results presented, the expected high correlation between the area and solar radiation pressure coefficient can be seen. As shown in Figure 6-7, no matter how the deviation from the reference area value is, the estimated SRP estimation also deviates from its true value in order to compensate for the error introduced in the cross-sectional surface of the satellite. Because of that, it can be observed that the resulting 3D error is almost negligible, since it is located in the low millimetre level and those small differences generally follow from numerical errors in the POD process and the fact that the GNSS observations are not ideal (white noise was added to them).

Furthermore, regarding the deviations in the centre of mass and antenna reference point shown in Figure 6-5 and Figure 6-6, it is first noticeable how the correlation with the SRP coefficient is much lower than it was for the uncertainty in the area. In this case, the deviations in the estimation of this model parameter are very small and does not ultimately manage to balance for the errors in the orbit solution induced by these inaccuracies in the satellite and antenna parametrization. On top of that, it can be observed how in both cases the deviation in the body-frame S axis is the one that carries a bigger error to orbit solution in 3D. The reasons behind such phenomena will be investigated in the following section but it is probably due to the fact that the S axis is oriented towards the direction of movement, that follow from the definition of the body-frame and nominal attitude. If that was the case, the error would lie in the along-track component which is generally much more sensitive to inaccuracies.

Finally, regarding the mismodelling of the geopotential model and the errors introduced in the GNSS ephemeris data and clocks (Table 6-6), it can be seen that the impact on the 3D orbit solution accuracy for these error sources is quite different. While the error when introducing uncertainties in Earth's geopotential model is in the order of a few millimetres (around 3mm), when using a different source of GNSS ephemeris and clock data the error is much bigger. In this case, a likely reason are the differences found in the GNSS clocks between both sources that would impact the estimation of the user satellites' trajectory.

6.3.2 Component-wise impact of orbit solution

As shown previously, the sources of error that most significantly affect the orbit solution in absolute terms are a deviation in the body-frame S axis for both the centre of mass and antenna reference point as well as uncertainties in the GNSS orbits & clocks and in the geopotential model. Following those findings, this section is focused in analysing the nature of the inaccuracies induced in the orbit solution by each of the included source of errors to better understand their correlation and the reasons behind them.

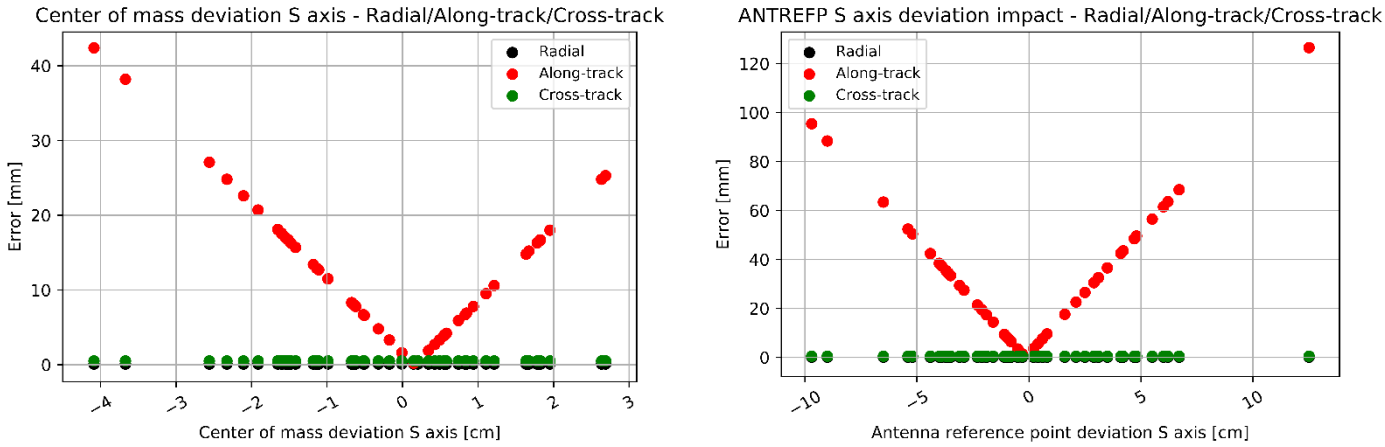

Figure 6-8. Impact of deviation in body-frame S axis of center of mass (left) and antenna reference point (right) in final orbit solution accuracy expressed in radial, along-track and cross-track components

Table 6-7.Impact of uncertainties in the geopotential model and inaccuracies in GNSS orbits and clocks expressed in radial, along-track and cross-track components

		Radial [mm]	Along-track [mm]	Cross-track [mm]
Geopotential model	EIGEN-6S2ext	0.8	3	0.8
	EIGEN.GRGS.RL03	0.6	2.5	0.8
GNSS ephemeris & clocks		1.6	4.9	11.3

Following the results presented above, the introduced sources of error have a greatest impact in the along-track component of the orbit solution, except for the GNSS ephemeris and clock errors. As previously stated, these component is the most sensitive and hardest to be estimated accurately and therefore seems reasonable to find the greatest inaccuracies in the direction of movement of the satellite.

It is important to note that for a satellite in an Earth-pointing attitude mode, the local body frame of the satellite will be changing its orientation at all times but the body-frame S axis will be aligned with the direction of movement at all times (recall Figure 4-2 for more clarity). Because of that, the results for the centre of mass deviations presented in the left-hand side of Figure 6-8 show that the error induced in the along-track component is in the order of a few centimetres while the error in the radial and cross-track components is almost negligible. Following the same line of thought, an error in the S axis for the antenna reference point will also affect the along-track component like shown in the right-hand side of Figure 6-8.

Regarding the geopotential models, it can be see that the greatest error is induced by the EIGEN-6S2ext in the along-track component as well. In this case, the use of a different geopotential model makes the estimation of the main force exerted on the satellite to be slightly different from the one used in the generation of the so-called real orbits. The fact that the forces exerted on the satellite can be estimated differently is directly linked to the velocity estimations. Thus, the error mainly affects the component of the orbit solution which is aligned to the velocity direction, which in this case is the along-track. Further information on the impact of modelling of geopotential models in the determined orbit solution for the specific case of DORIS satellites can be found in Stepanek et al. (2016).

The inaccuracies present in the GPS and Galileo orbits and clocks have mainly impacted the orbit solution in its cross-track component. The highest error would have expected to be in the along-track explained by the fact that the GNSS clocks are a key factor in generating and reconstructing both code and phase signals which generally affect the orbit estimation in the velocity component. Further research and tests that involve the use of ephemeris data and clocks from other days and other GNSS satellites would be important to fully understand the impact of the inaccuracies in the orbit solution. It is important to state that both CODE and GRGS orbits and clocks are considered to be very precise (they are not a navigation solution) but in this case the sensitivity of the final orbit solution with respect to the GNSS clocks has proven to be so high that even the difference from two very precise solutions can affect it in the order of centimetres as shown in Table 6-7.

Please note that the component-wise impact of inaccuracies in the R and W body-frame components of both centre of mass and antenna reference point can be found in Appendix A and have not been included since they did not provide any extra information to the analysis.

6.4 Absolute orbit solutions

In this section, and following the analysis performed previously, a final configuration of the error sources is selected and the corresponding orbit solutions are obtained. The goal is not only to perform realistic absolute POD, but also to obtain perturbed orbits of both satellites in absolute terms that can also be used to derive relative differences. These orbits can be used as starting point in the upcoming relative POD processes in which the use of ISL observations are assessed.

From what was learnt in the previous section, not all sources of error neither have the same influence on the final orbit solution nor do they affect it in the same component. The inaccuracies

have been introduced in all components of the centre of mass and antenna reference point, being as can be seen from Table 6-8. The area of both satellites was modified in same magnitude but different sign even though their influence is greatly balanced by the solar radiation coefficient. Finally, the geopotential model chosen was the least updated version of the pair analysed that yields the higher orbit error and the GNSS orbits and clock new source was chosen to be the only one examined, CNES.

The final absolute orbit solutions of MEO-1 and MEO-2 satellites as well as GPS/Gal residuals corresponding to such simulations are presented. The configuration employed has been summarized in Table 6-8 below.

Table 6-8. Final configuration of Absolute POD processes

Orbit determination parameters		
MEO-1 & MEO-2 state vectors		Position, Velocity, C_R (7 variables estimated per satellite)
MEO clocks		Estimated per epoch, every 30 s
GPS/Galileo ephemeris & clocks source		CNES (GRGS products – multi GNSS)
GPS/Galileo orbits		Fixed
GPS/Galileo clocks		Fixed
GNSS phase ambiguity		Estimated
Determination arc		24-hr
Observations		
Pseudo-range weight sigma		1.5 m
Carrier-phase weight sigma		10 mm
Minimum grazing altitude		100 km
Corrections applied		Center of mass, Antenna Phase Center, Antenna Phase Wind-up
Dynamical Model		
Gravity field		EIGEN-6S2ext.coef (120x120)
Solar Radiation Pressure		IERS Conventions 2003 –C_R fixed, change in cross-sectional area
Rest of perturbations		Same as in Table 4-1
Satellite reference		
Centre of mass (R,S,W)	MEO-1	$(0.76, 0.02, -0.01)$ m
	MEO-2	$(0.74, -0.02, 0.01)$ m
Cannonball area	MEO-1	4.9 m^2
	MEO-2	5.1 m^2
Attitude model		Earth-pointing mode
Antenna reference point (R,S,W)	MEO-1	$(0.95, 0.00, 0.03)$ m
	MEO-2	$(1.05, 0.01, -0.03)$ m
Antenna orientation (Euler Angles)		Nadir-oriented (0º, 180º, 0º)

6.4.1 CLO scenario

The results for the conditions in which the satellites are close to each other (1,000km) can be found below. The final absolute orbit solution accuracy in 3D for both satellites is placed in the few cm level which can be considered as realistic values. Please note that Typical RMS refers to the square root of the sum of the squared RMS values in radial, along-track and cross-track.

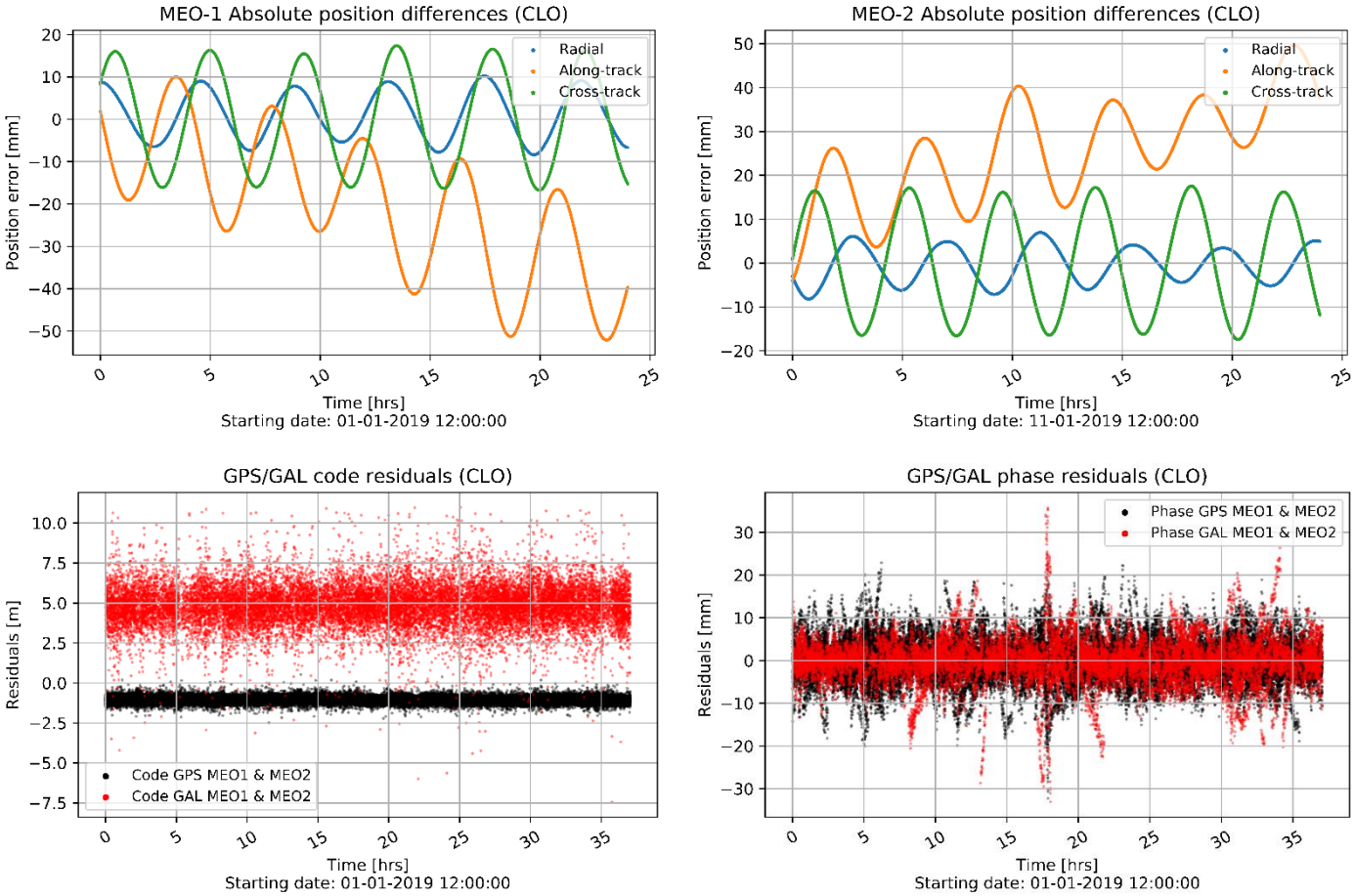

Figure 6-9. Absolute position differences (top) and GNSS observations (code, phase) residuals (bottom) (CLO)

Table 6-9. Summary of position differences after realistic POD process (CLO)

Satellite		Radial [mm]	Along-track [mm]	Cross-track [mm]	Total 3D [mm]	Typical RMS [mm]
MEO-1	Mean	1.05	-20.48	0.56		
	RMS	5.78	26.11	11.54	29.12	16.81
	Max	10.22	10.05	17.38		
MEO-2	Mean	-0.45	25.65	0.85		
	RMS	4.17	28.23	11.76	30.86	17.82
	Max	6.96	49.68	17.56		

Table 6-10. Summary of observation residuals (code, phase) for both GPS and Galileo constellations (CLO)

Satellite	GPS code observations				GPS phase observations			
	Total	Rejected	Mean (m)	RMS (m)	Total	Rejected	Mean (mm)	RMS (mm)
MEO-1	22721	74	-1.05	1.07	22721	74	0.00	4.60
MEO-2	22804	70	-1.05	1.07	22804	70	0.00	4.55
Satellite	**GAL code observations**				**GAL phase observations**			
	Total	Rejected	Mean (m)	RMS (m)	Total	Rejected	Mean (m)	RMS (m)
MEO-1	10569	45	4.84	5.03	10569	45	0.00	4.67
MEO-2	10616	73	4.85	5.03	10616	73	0.00	5.32

6.4.2 MID scenario

The results for the conditions in which the satellites are neither close not far from each other (10,000km) can be found below. The final absolute orbit solution accuracy for MEO-2 satellite is slightly worse than for MEO-1. It can be due to worsened visibility conditions in that particular observation arc since MEO-1 presents less tracking observations compared to the other cases.

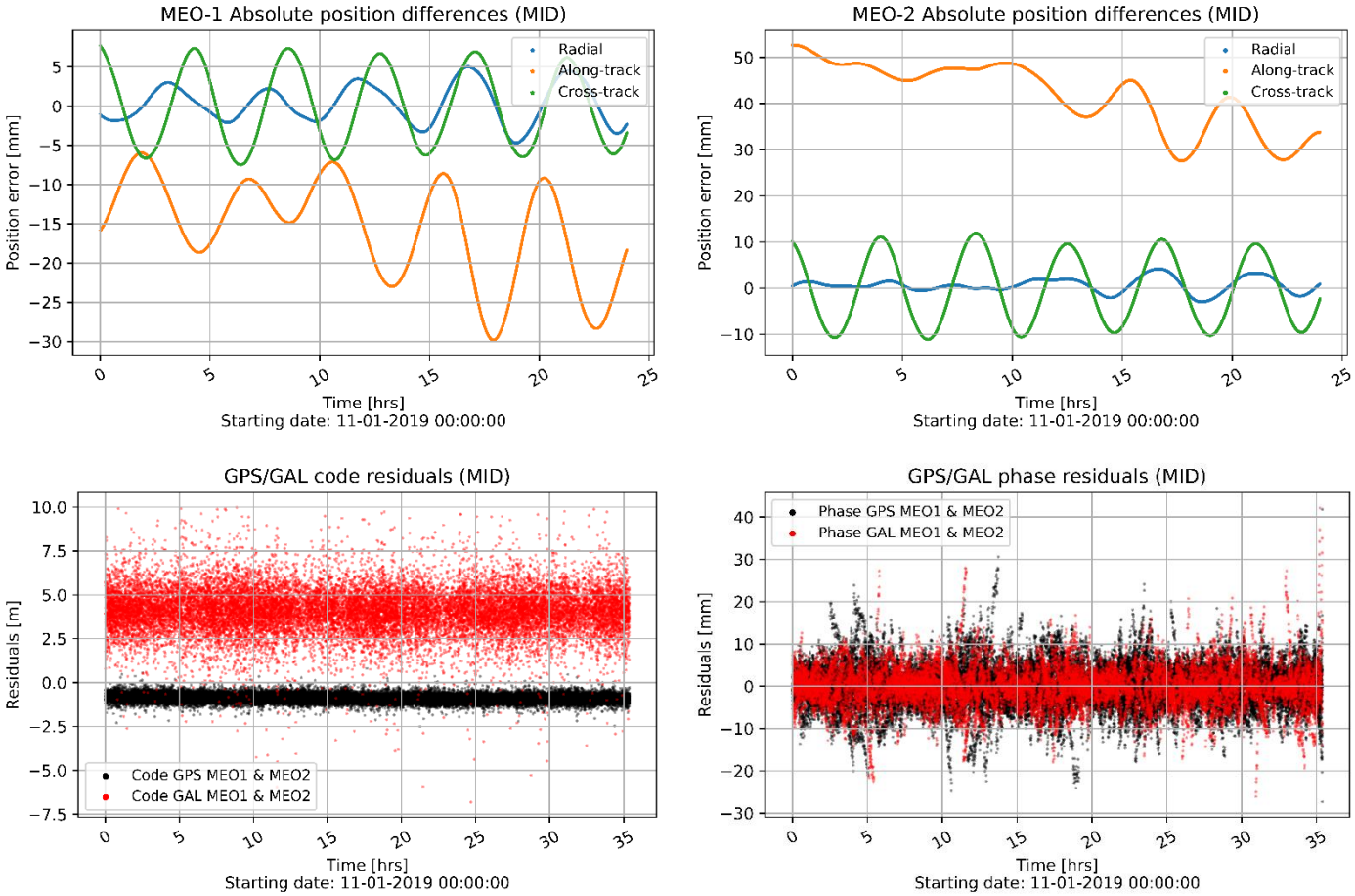

Figure 6-10. Absolute position differences (top) and GNSS observations (code, phase) residuals (bottom) (MID)

Table 6-11. Summary of position differences after realistic POD process (MID)

Satellite		Radial [mm]	Along-track [mm]	Cross-track [mm]	Total 3D [mm]	Typical RMS [mm]
MEO-1	Mean	0.32	-15.52	-0.08		
	RMS	2.45	16.79	4.83	17.64	10.19
	Max	5.00	-5.94	7.71		
MEO-2	Mean	0.62	41.79	-0.33		
	RMS	1.67	42.40	7.40	43.07	24.87
	Max	4.16	52.68	11.89		

Table 6-12. Summary of observation residuals (code, phase) for both GPS and Galileo constellations (MID)

Satellite	GPS code observations				GPS phase observations			
	Total	Rejected	Mean (m)	RMS (m)	Total	Rejected	Mean (mm)	RMS (mm)
MEO-1	21448	5	-0.91	0.93	21448	5	0.00	4.80
MEO-2	21902	6	-0.87	0.89	21902	6	0.00	4.49
Satellite	**GAL code observations**				**GAL phase observations**			
	Total	Rejected	Mean (m)	RMS (m)	Total	Rejected	Mean (m)	RMS (m)
MEO-1	10349	24	4.04	4.25	10349	24	0.00	4.68
MEO-2	9996	40	4.09	4.30	9996	40	0.00	4.46

6.4.3 FAR scenario

The results for the conditions in which the satellites are far from each other (20,000km) can be found below. The final absolute orbit solution accuracy for both satellites is very similar and placed at the few cm level.

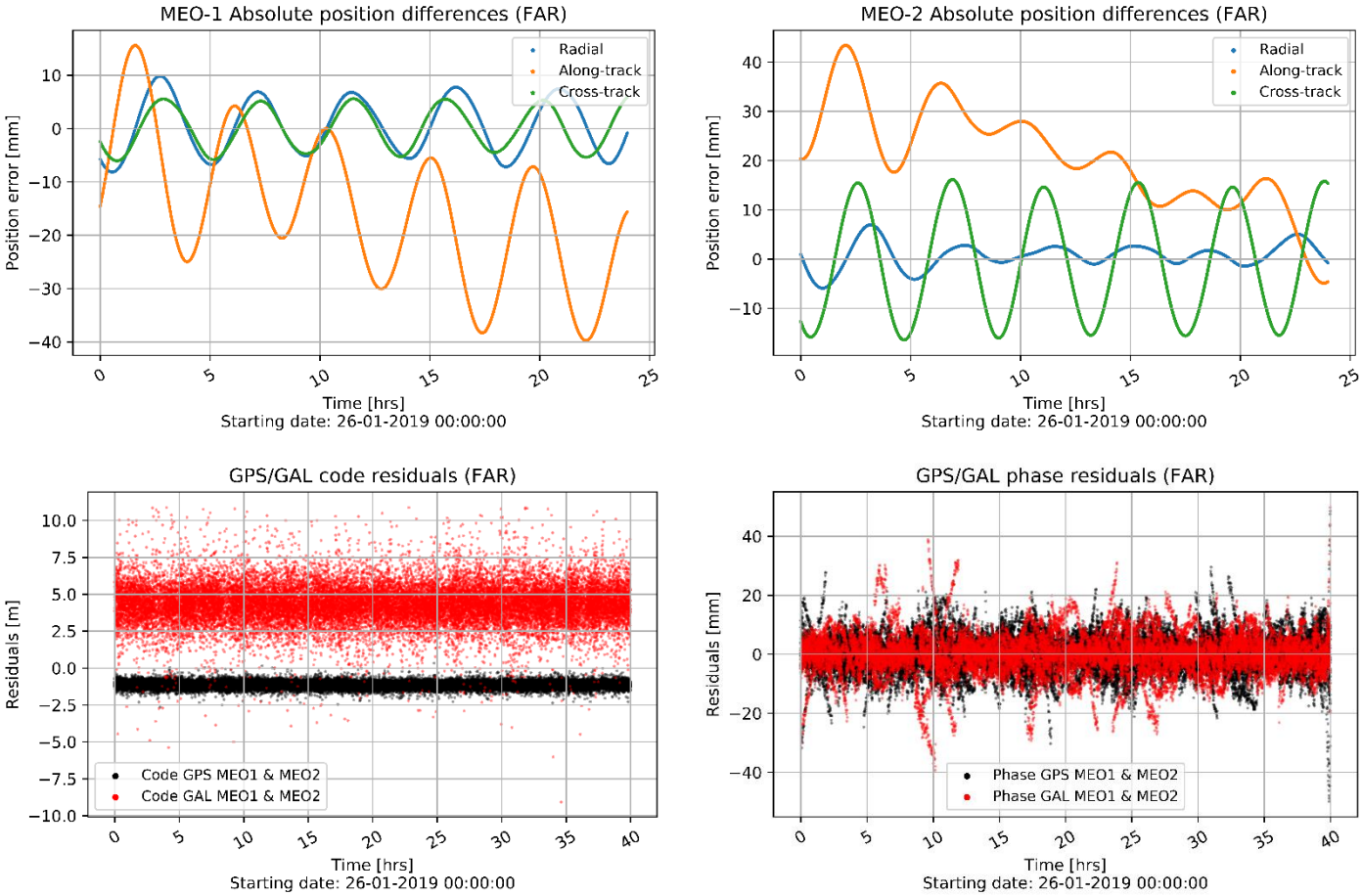

Figure 6-11. Absolute position differences (top) and GNSS observations (code, phase) residuals (bottom) (FAR)

Table 6-13. Summary of position differences after realistic POD process (FAR)

Satellite		Radial [mm]	Along-track [mm]	Cross-track [mm]	Total 3D [mm]	Typical RMS [mm]
MEO-1	Mean	0.37	-14.92	-0.05		
	RMS	5.15	20.14	3.82	21.13	12.20
	Max	9.88	15.63	5.96		
MEO-2	Mean	0.72	20.61	-0.44		
	RMS	2.65	23.03	11.15	25.72	14.85
	Max	6.96	43.44	16.16		

Table 6-14. Summary of observation residuals (code, phase) for both GPS and Galileo constellations (FAR)

Satellite	GPS code observations				GPS phase observations			
	Total	Rejected	Mean (m)	RMS (m)	Total	Rejected	Mean (mm)	RMS (mm)
MEO-1	22499	11	-1.13	1.15	22499	11	0.00	5.22
MEO-2	23371	32	-1.16	1.18	23371	32	0.00	5.55
Satellite	**GAL code observations**				**GAL phase observations**			
	Total	Rejected	Mean (m)	RMS (m)	Total	Rejected	Mean (m)	RMS (m)
MEO-1	12625	27	4.34	4.54	12625	27	0.00	6.48
MEO-2	13484	21	4.33	4.54	13484	21	0.00	6.17

6.4.4 Discussion of results

The orbit solutions of both MEO satellites in all three case scenarios present the highest inaccuracies from the reference orbits in the along-track component due to the phenomena explained in the previously in this chapter. Errors in the radial and cross-track components have also appeared even though their magnitude is generally lower than in comparison with the along-track. In general terms, the total 3D errors of the 6 orbit solutions are in the centimetre level and range from a minimum of 1.7 to a maximum of 4.3 (Table 6-9, Table 6-11, Table 6-13). These can be considered as quite representative errors in the absolute orbit solutions, as they lie in the range of state-of-the-art missions such as the Sentinels (Berzosa and Fernandez, 2018). Thus, it is safe to state that a similar performance in all three scenarios has been obtained. These results for absolute POD with no difference between the three study cases were expected.

Additionally, and as happened with the GNSS residuals presented in the validation section 6.1, there is a bias in the code observations of the GPS and Galileo observations. As explained before, it is due to the fact that they present different time systems in which Galileo presents an offset with respect to GPS. It only affects to the absolute observations (pseudorange) and not the ambiguous ones (phase) as can be observed in bottom of Figure 6-9, Figure 6-10 and Figure 6-11).

Finally, it can be seen how the position differences of both MEO-1 and MEO-2 satellites are quite disperse from one another in all three case scenarios (top of Figure 6-9, Figure 6-10 and Figure 6-11) which generally implies that the relative positioning accuracy will also be perturbed. Contrarily, if the two orbit solutions in the same determination arc presented absolute orbit solutions that had been perturbed in the same way or direction, it not necessarily would translate into a perturbed relative orbit solution. In this case, perturbing the relative positioning accuracy at this stage was very important since these orbits are used as starting points for the corresponding relative POD processes presented in the next chapter. Especially for the cases with an initial non-precise relative orbit solution, the use of ISL might be beneficial to improve the relative POD accuracy.

7

Results: Relative POD

In this chapter, the results obtained by means of relative POD are presented and analysed. The validation of the simulated ISL observations and software used are presented first. In this case white Gaussian noise was added to the simulated inter-satellite links observations to avoid problems with the conditioning of the LSQ matrix. In the validation process, the goal was to show accurate relative orbit positioning of the MEO-placed satellites was obtained under these ideal conditions (even with measurement noise). Please note that in all relative POD serves to refine the orbit of MEO-2 while MEO-1 is kept fixed. In section 7.2. the use of inter-satellite links is assessed in all three case scenarios to determine the impact of the relative distance between the satellites in the accuracy of the relative orbit solutions. Finally, and due to the fact that the orbits of both satellites are co-planar as defined by the initial state vectors shown in Chapter 1, there are some complications that arise from this fact. Therefore, section 7.3 is focused in analysing different possibilities to overcome the added complexity that comes along with both MEO-1 and MEO-2 satellites being in the same orbit plane.

7.1 Validation

The validation of the relative POD process by means of ISL observations is presented below. The results presented in this section are only means to provide proof that under ideal, and therefore not realistic, circumstances the use of ISL provides accurate relative positioning. Hence, the results neither confirm nor deny any hypothesis presented previously in the set of research questions. Those questions always refer to case scenarios in which the configuration of the simulations is up to some point representative of reality and can only be answered then.

It is important to stress that the validation has been performed under the circumstances of close, mid and far relative distance between the satellites. As can be expected, the case scenario in which the satellites are close to each other is more favourable for obtaining low accuracies in the relative positioning and actually represents a good approach to assess the impact of the use of inter-satellite links in a relative POD process. However, obtaining a positive outcome in the validation tests of the mid and far case scenarios in which the conditions might not be as favourable, would fully validate the configuration and methodology implemented in all relative POD processes.

Additionally, it has to be noted that the initial orbits of MEO-1 and MEO-2 used as starting points for the relative POD were also obtained error-free in the absolute POD process and are the ones shown in section 6.1. Therefore, it can be considered that the results presented below are the result of implementing a full error-free POD process, first in absolute and then in relative terms. The comparison of relative positioning has been done in the J2000 ECI reference frame (XYZ)

since it actually represents the differences of the differences between the propagated and determined orbits of the satellites. Establishing a body frame for such long baselines is not very meaningful and the reason why the relative accuracy was assessed in the inertial reference frame. Finally, it can be seen in Table 7-1 a set of empirical accelerations have been defined in the along-track component of the satellite even when there are no dynamical errors to absorb. Due to the fact that the residuals of the ISL observations have such a small order of magnitude in comparison to the GNSS observations, the definition of these accelerations helped the conditioning of the LSQ matrix.

Table 7-1. Configuration of simulations to validate Relative POD process

Orbit determination		
MEO-2 estimated parameters		Position, Velocity, sets of empirical accelerations
Initial position, velocity weight sigmas		$\sigma_{pos} = 1\ cm, \sigma_{pos} = 0.01\ mm/s$
MEO-2 fixed parameters		Clocks and C_R (obtained from Abs POD simulations)
GNSS parameters		GPS/Galileo clocks and orbits fixed
Emp accelerations arcs		every 15.0 min
Emp accelerations reference frame		RSW
Emp accelerations parameters		Only estimated in along-track component (S)
GPS/Galileo ephemeris & clocks source		AIUB (CODE products – multi GNSS)
Observations		
Pseudo-range weight sigma		1.5 m
Carrier-phase weight sigma		10 mm
ISL weight sigma		10 μm
Minimum grazing altitude		100 km
Corrections applied		Center of mass, Antenna Phase Center, Antenna Phase Wind-up
Dynamical Model		
Gravity field		EIGEN.GRGS.RL04.qmp (120x120)
Rest of perturbations		Same as in Table 4-1
Satellite reference		
Centre of mass (R,S,W)	MEO-1	$(0.75, 0.00, 0.00)$ m
	MEO-2	$(0.75, 0.00, 0.00)$ m
Cannonball area	MEO-1	5.0 m^2
	MEO-2	5.0 m^2
Attitude model		Earth-pointing mode
Antenna reference point (R,S,W)	MEO-1	$(1.00, 0.00, 0.00)$ m
	MEO-2	$(1.00, 0.00, 0.00)$ m
Antenna orientation (Euler angles)		Nadir-oriented (0º, 180º, 0º)

Table 7-2. Relative differences for all Rel POD validation tests

Scenario		X [mm]	Y [mm]	Z [mm]	Total 3D [mm]	Typical RMS [mm]
CLO	Mean	-0.01	-0.01	-0.01		
	RMS	0.08	0.07	0.08	0.14	0.08
	Max	0.14	0.11	0.17		
MID	Mean	-0.08	-0.03	-0.09		
	RMS	1.92	0.51	1.93	2.77	1.60
	Max	3.58	0.70	3.43		
FAR	Mean	-0.10	0.06	0.03		
	RMS	3.72	1.50	3.83	5.55	3.20
	Max	7.08	2.12	7.77		

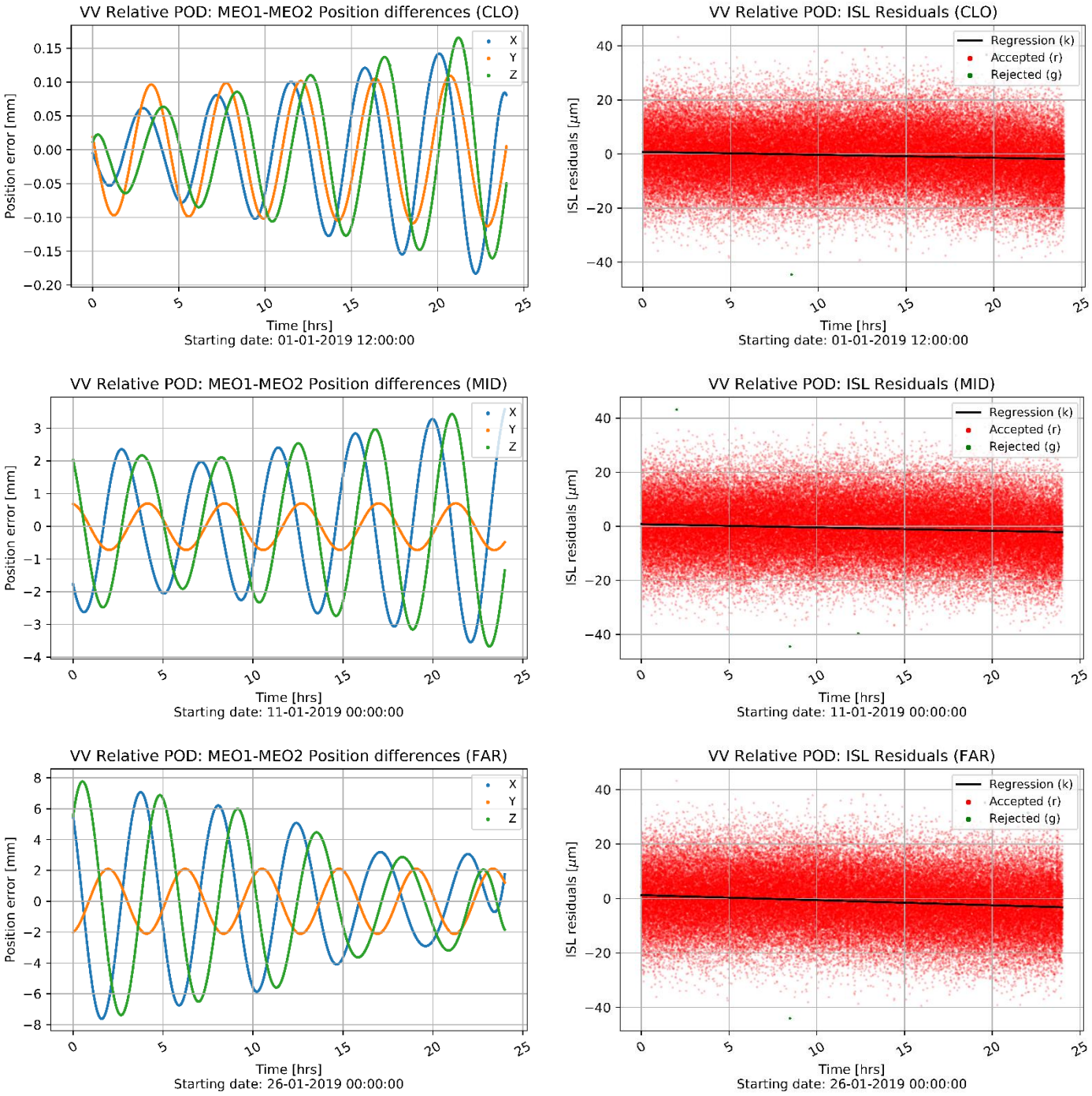

Figure 7-1. Position differences and ISL residuals for all Rel POD validation tests

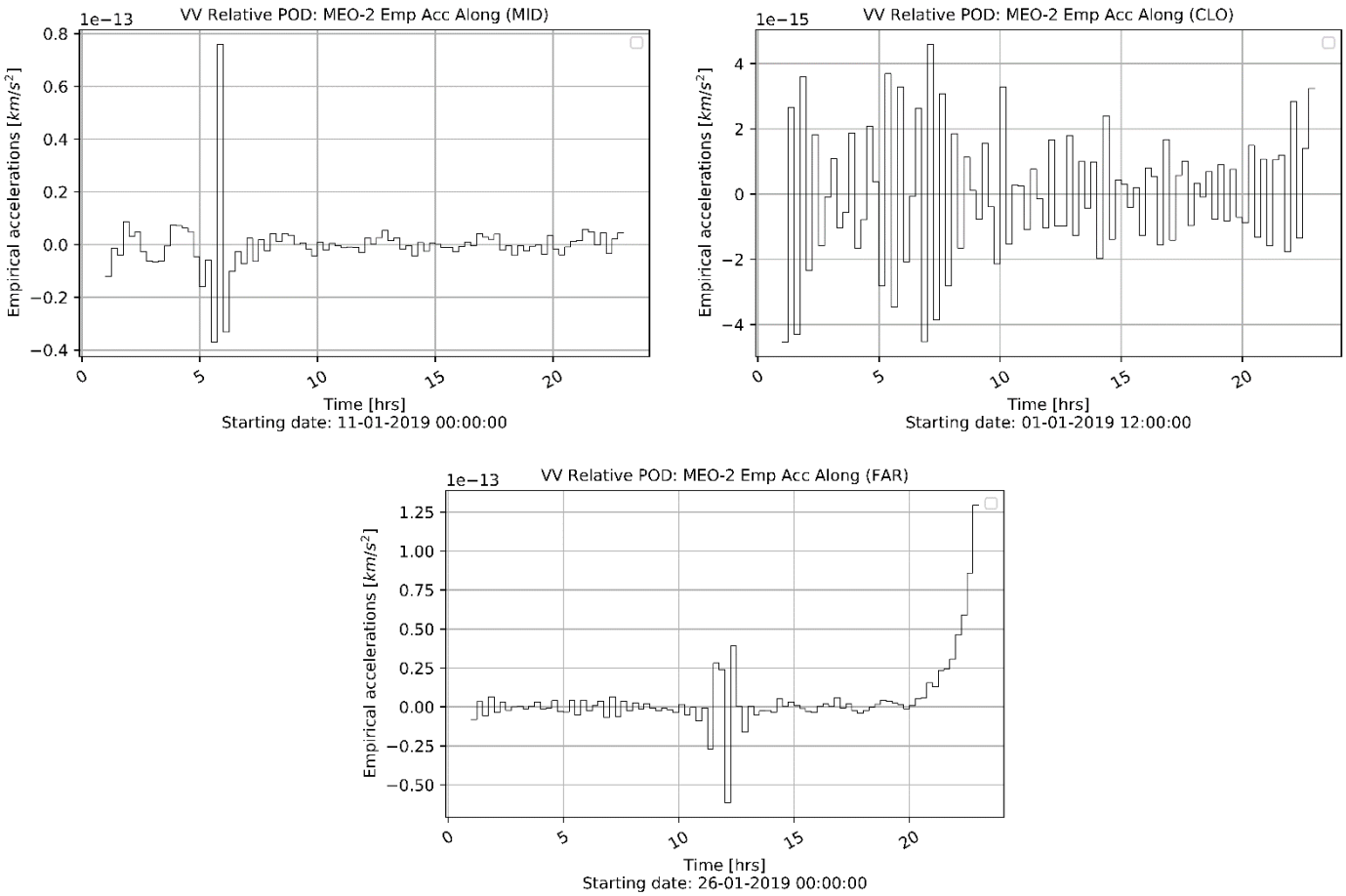

Figure 7-2. Estimated empirical accelerations for all Rel POD validation tests

First of all, it can be seen that the greatest accuracy is obtained in the scenario in which the satellites are close to each other. In this case the total 3D error is situated below the millimetre level (0.14 mm), an accuracy only possibly achievable in ideal conditions. Second, the precision in the other two case scenarios (MID, FAR) is still very high and placed in the millimetre level (2.77 and 5.55 mm in total 3D error respectively). Regarding the trend of the relative position differences shown in the left-hand side of Figure 7-1, in which depending on the scenario they seem to increase, decrease or remain constant in amplitude of oscillation. These behaviour are probably related to the initial relative position differences that follow from the relative differences of the absolute orbits obtained by means of GNSS observations only. In general terms, due to the fact that these are validation tests and there are no dynamical or satellite model errors to absorb, the final relative accuracy has shown to be very high. Moreover, it can be observed that the closer the satellites the highest the accuracy of the relative positioning and as they get further away from each other the accuracy is limited by the precision of the ISL measurements.

Additionally, as shown in Table 7-1 above, the white noise included in the inter-satellite links measurements is $10\ \mu m$ because the NAPEOS software would not allow a lower precision in the observations. Because of that, it can be seen how the observation residuals in all three cases present the same order of magnitude $(-20, 20 \mu m)$ which translates into a higher relative orbit accuracy when the satellites are closer to each other on comparison to when they are further apart. Furthermore, in all 3 cases the regression line of the ISL residuals is not completely straight but presents a slight negative slope (right-hand side Figure 7-1). This phenomena should be further researched but it could be related to the way in which the observations have been optimized in batch; where the optimum fit to those observations lies within the 24-hr observation arc. Finally, it is also important to note how the magnitude of the estimated empirical accelerations is lower for the scenario in which the satellites are closer, probably due to the similarities in the perturbations impacting the satellite (Figure 7-2). This enlightens the fact that the lower the estimation of the empirical accelerations is, the easier it is for the least-squares algorithm to find a fit for the ISL observations. In these cases, the empirical accelerations are probably absorbing

numerical errors and providing more degrees of freedom to the LSQ algorithm since the simulations have been carried out without dynamical or satellite model errors.

In general terms, the results obtained in these ideal test case simulations are expected and can be used as proof that the methodology and approach taken to the relative POD process has been validated.

7.2 Impact of inter-satellite links in relative positioning

In this section of the report, the use of inter-satellites to improve the relative positioning between the satellites is assessed. After having validated the methodology employed in the relative POD processes, in these simulations a more realistic configuration is employed. As happened before with the absolute POD simulations, a set of sensible errors are included in the Relative POD processes to represent conditions more similar to the ones encountered in real-life. Such errors are highlighted in red in Table 7-3 below and are exactly the same as the ones included in the Absolute POD processes.

Table 7-3. Final configuration of Relative POD processes

Orbit determination		
MEO-2 estimated parameters		Position, Velocity, sets of empirical accelerations
Initial position, velocity weight sigma		$\sigma_{pos} = 1\ cm, \sigma_{pos} = 0.01\ mm/s$
MEO-2 fixed parameters		Clocks and C_R (obtained from Abs POD simulations)
GNSS parameters		GPS/Galileo clocks and orbits fixed
Emp accelerations arcs		every 15.0 min
Emp accelerations reference frame		RSW
Emp accelerations parameters		Only estimated in along-track component (S)
GPS/Galileo ephemeris & clocks source		CNES (GRGS products – multi GNSS)
Observations		
Pseudo-range weight sigma		1.5 m
Carrier-phase weight sigma		10 mm
ISL weight sigma		10 μm
Minimum grazing altitude		100 km
Corrections applied		Center of mass, Antenna Phase Center, Antenna Phase Wind-up
Dynamical Model		
Gravity field		EIGEN-6S2ext.coef (120x120)
Rest of perturbations		Same as in Table 4-1
Satellite reference		
Centre of mass (R,S,W)	MEO-1	$(0.76, 0.02, -0.01)$ m
	MEO-2	$(0.74, -0.02, 0.01)$ m
Cannonball area	MEO-1	4.9 m^2
	MEO-2	5.1 m^2
Attitude model		Earth-pointing mode
Antenna reference point (R,S,W)	MEO-1	$(2.95, 0.0, 0.03)$
	MEO-2	$(3.05, 0.01, -0.03)$
Antenna orientation (Euler angles)		Nadir-oriented (0º, 180º, 0º)

Once the configuration of the simulations has been clearly stated, the set of results presented in this chapter are reviewed. First, this section is divided into four main subsections: the first three are dedicated to the presentation of results in terms of relative positioning that correspond to the 3 selected case scenarios and the last is focused in discussing the previously presented results mainly focusing in the differences between them. When it comes to the type of data presented for the CLO, MID, FAR scenarios, there are 2 graphs of relative position residuals (before and after applying the relative POD process), 1 table summarizing the position residuals in both situations, another graph of the ISL residuals and a graphical representation of the empirical accelerations. It is important to note that the initial relative position residuals (prior to applying the Rel POD

process) are a result of the orbit differences that follow from the absolute POD processes in which the set of errors highlighted in red above were also included.

7.2.1 CLO scenario

The results for the conditions in which the satellites are close to each other (1,000km) can be found below. The final relative orbit solution accuracy in 3D is placed at 1 mm in the radial and along-track components (X,Z in ECI J2000). The cross-track component is not visible and a local minimum has been found. Please note that Typical RMS refers to the square root of the sum of the squared RMS values in radial, along-track and cross-track.

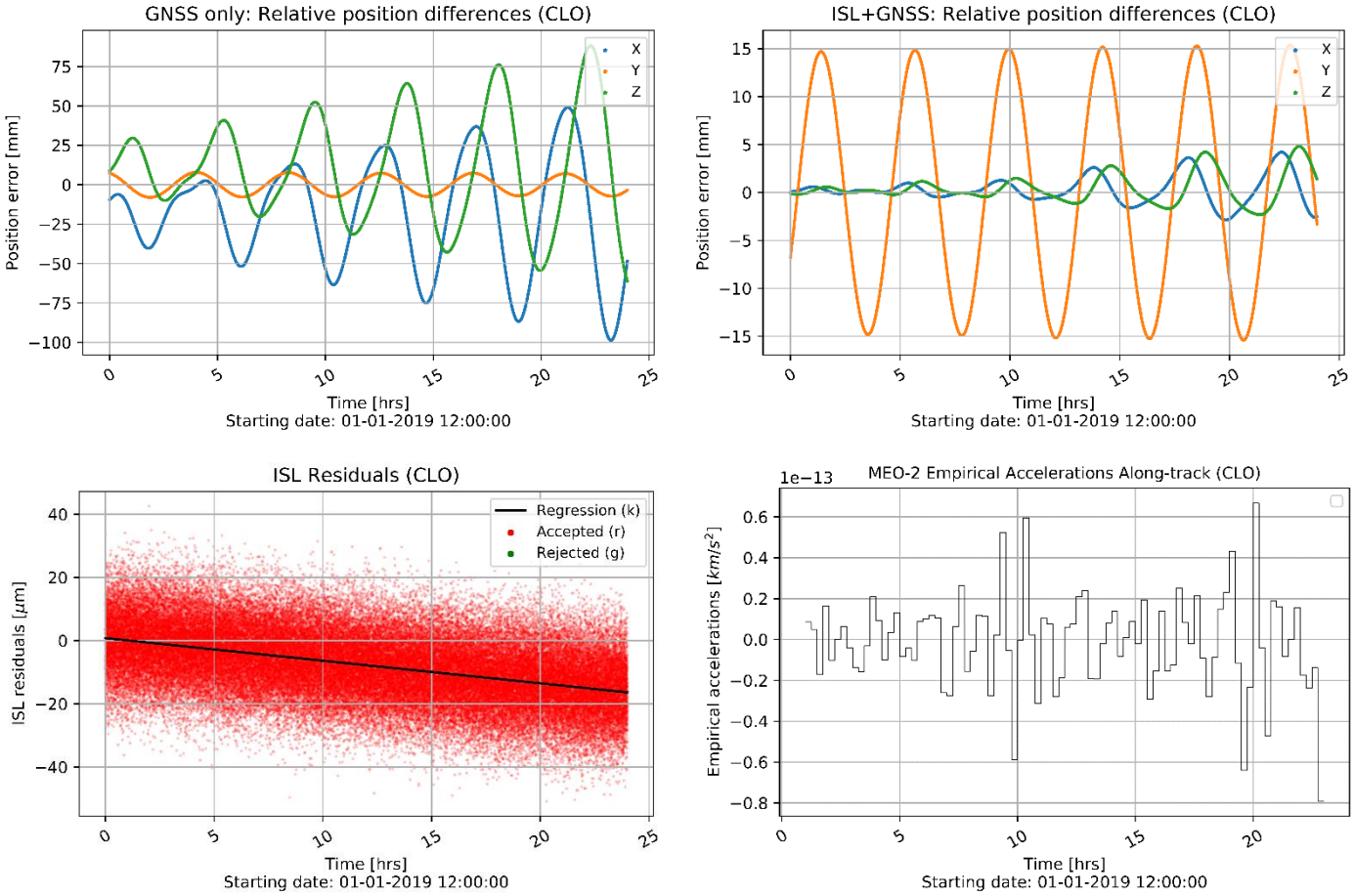

Figure 7-3. Initial relative position differences (upper-left), final relative position differences (upper-right), ISL residuals (lower-left), estimated empirical accelerations (lower-right) (CLO)

Table 7-4. Summary of position residuals for Abs POD (GNSS) and Rel POD (ISL+GNSS)

Conditions		X [mm]	Y [mm]	Z [mm]	Total 3D [mm]	Typical RMS [mm]
GNSS	Mean	-18.9564	-0.2865	11.6151		
	RMS	40.2049	5.3331	36.4952	54.5598	31.5001
	Max	49.0813	7.8617	88.2662		
ISL+GNSS	Mean	0.3153	0.7676	0.4456		
	RMS	1.4836	10.5660	1.5827	10.7864	6.2275
	Max	4.1998	15.3664	4.8101		

7.2.2 MID scenario

The results for the conditions in which the satellites are neither close nor far to each other (10,000km) can be found below. The final relative orbit solution accuracy in 3D is placed at 8 mm in the radial and along-track components (X,Z in ECI J2000). The cross-track component is still not visible, and a precise local minimum was found in this case.

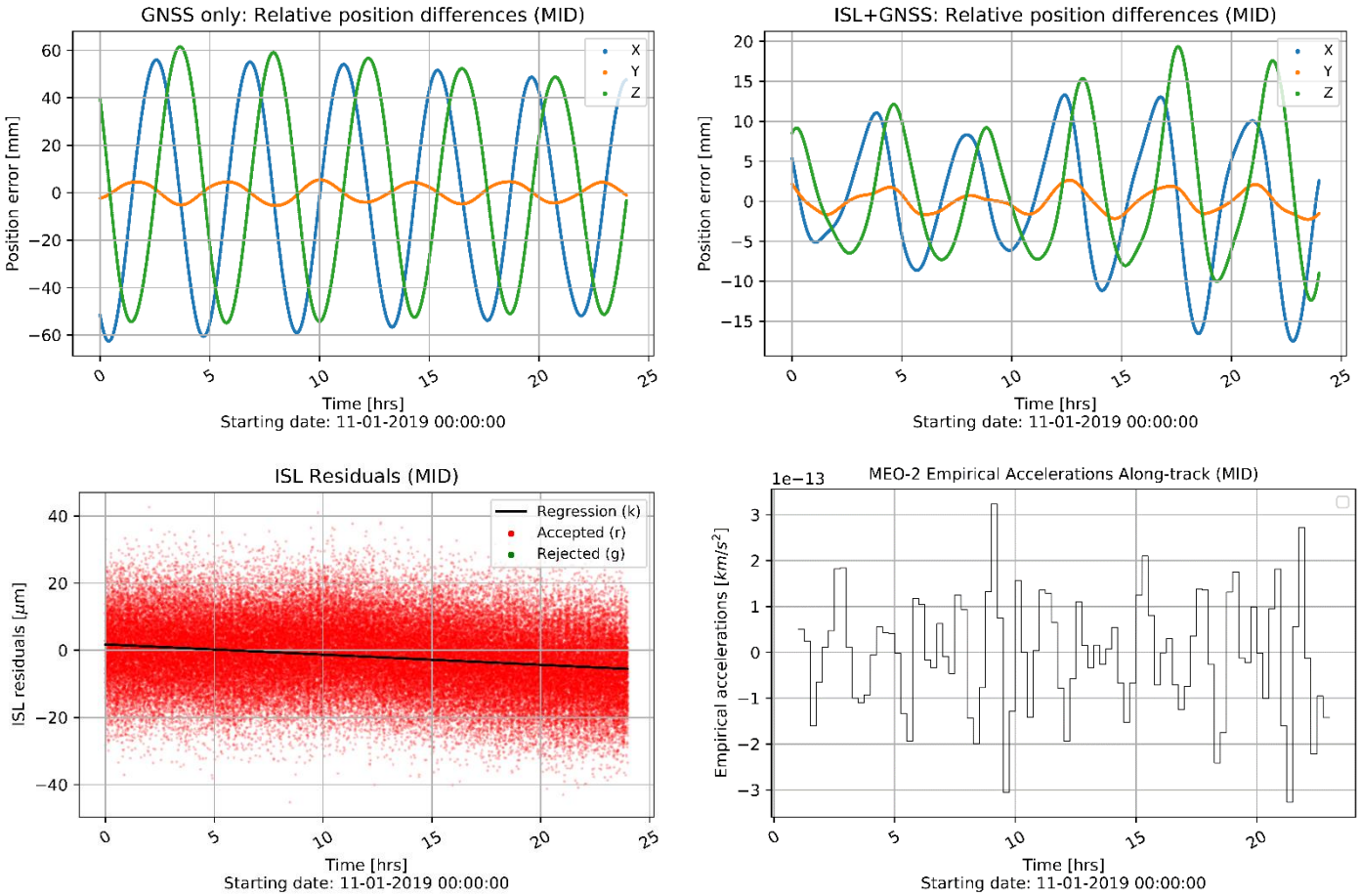

Figure 7-4. Initial relative position differences (upper-left), final relative position differences (upper-right), ISL residuals (lower-left), estimated empirical accelerations (lower-right) (MID)

Table 7-5. Summary of position residuals for Abs POD (GNSS) and Rel POD (ISL+GNSS)

Scenario		X [mm]	Y [mm]	Z [mm]	Total 3D [mm]	Typical RMS [mm]
GNSS	Mean	-2.71169	0.251234	-0.44084		
	RMS	39.05352	3.29596	38.43646	54.89447	31.69334
	Max	55.97869	5.427421	61.52789		
ISL+GNSS	Mean	-0.2232	-0.0395	1.5228		
	RMS	7.9333	1.2940	8.2071	11.4877	6.6324
	Max	13.3020	2.6374	19.3455		

7.2.3 FAR scenario

The results for the conditions in which the satellites are far to each other (20,000km) can be found below. The precision of the final relative orbit solution accuracy in 3D has been significantly worsened and is placed at 23 mm in the radial and along-track components (X,Z in ECI J2000). The long baseline between the satellites has proven to be an important factor regarding the loss in relative accuracy.

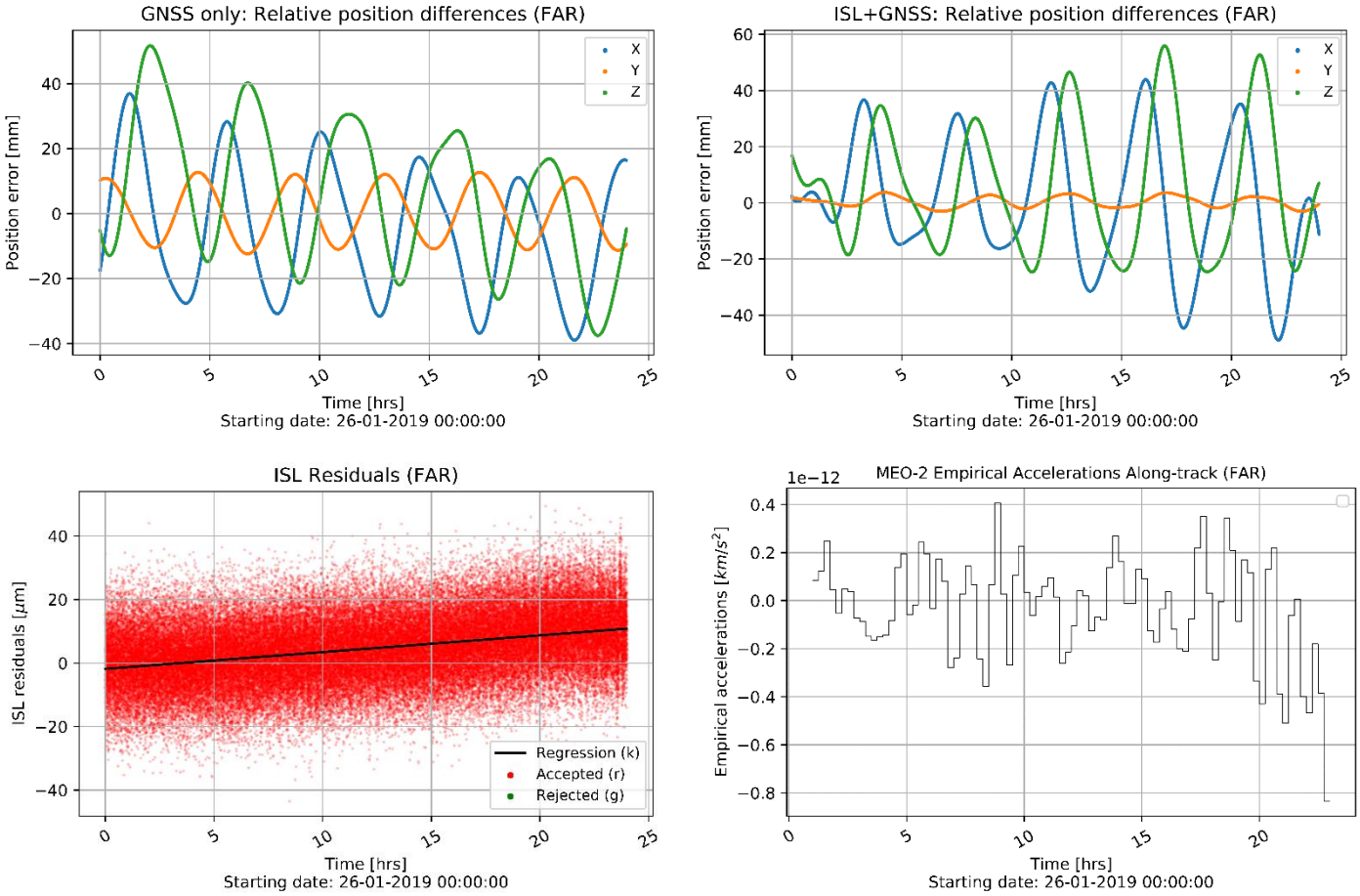

Figure 7-5. Initial relative position differences (upper-left), final relative position differences (upper-right), ISL residuals (lower-left), estimated empirical accelerations (lower-right) (FAR)

Table 7-6. Summary of position residuals for Abs POD (GNSS) and Rel POD (ISL+GNSS)

Scenario		X [mm]	Y [mm]	Z [mm]	Total 3D [mm]	Typical RMS [mm]
GNSS	Mean	-4.7032	0.3902	6.1100		
	RMS	20.5405	8.3061	22.9623	31.9088	18.4225
	Max	36.9823	12.7301	51.7113		
ISL+GNSS	Mean	0.7966	0.3577	5.8704		
	RMS	23.1086	1.9064	23.3156	32.8825	18.9847
	Max	43.8983	3.6942	55.9552		

7.2.4 Discussion of results

First of all, it is important to understand the meaning of the XYZ axes in the J2000 ECI reference frame in order to be able to analyse the accuracy of relative positioning results. Since the orbits of both MEO-1 and MEO-2 are polar (their inclination is 90º), then the J2000 Y axis corresponds to their cross-track component. Thus, the J2000 X and Z components are coupled and both represent a combination of the radial and along-track components.

Secondly, it can be seen from the results presented in sections 7.2.1 to 7.2.3 that the scenario in which the relative accuracy has experienced a greater gain is when the satellites are close. In those conditions, and as shown in upper-right Figure 7-3 and Table 7-4, the relative accuracy between the satellites goes down to around 1 mm in the X and Z axes (1.48 & 1.58mm respectively) due to the inclusion of inter-satellite link observations which are very precise observations in these components. The relative position accuracy in the Y axis is much higher than in the other 2 components, and it oscillates in time with constant amplitude (upper-right Figure 7-3). This behaviour can be explained by means of the ISL not giving any information in the cross-component of the relative motion between the satellites since the orbits of both satellites are defined as co-planar by the initial state vectors defined in Table 1-1. Additionally, the ISL residuals lie in the range $(-20, 20\mu m)$ as in the validation test cases but present a more pronounced slope regression line which explains the increment trend of the relative position residuals in the X and Z axes. In that regard, the further the observations are from the reference epoch in which the state vector is determined, the harder it is to fit them to the dynamical model, which in this case presents deficiencies with respect to the one used in validation. Finally, it was vital to include constant piece-wise empirical accelerations in the along-track body frame of the MEO-2 to help the LSQ algorithm fit the ISL observations. As shown in lower-right Figure 7-3, they present an oscillating behavior that is possibly related to the fact that the relative distance between the satellites in their respective along-track components is also oscillatory. The magnitude of such empirical accelerations is located at the $10^{-11}\, m/s^2$ level, which is something expected for medium MEO-placed satellites; it is around $10^{-6}\, m/s^2$ for low-LEO as shown in Berzosa and Fernandez (2018) for the Sentinel satellites.

Thirdly, there are some main conclusions that can be drawn from the results obtained for the mid and far case scenarios. The first one is that they further away the satellites are from each other, the lower the gain in relative positioning accuracy that follows from the use of ISL. As can be extracted from the information in Table 7-5, when the satellites are 10,000km away from each other (MID) the precision obtained is of 7.9 and 8.2 mm in the X and Z axes respectively. Contrarily, as seen in Table 7-6, such accuracies grow up to 23.1 and 23.3 mm respectively when the satellites are 20,000km apart (FAR). These results highlight the fact that, if the precision of the inter-satellite link ranging observation is maintained constant, the relative distance between the satellites is a key factor in determining the accuracy of the relative positioning fit between them. This conclusion is also confirmed by the set of determined set of empirical accelerations, whose magnitude is higher as the relative distance between the satellites gets bigger (lower-right of Figure 7-4 and Figure 7-5). As the fit of the ISL observations gets much more complicated due to the big separation between the satellites, the estimation of these empirical accelerations is also higher.

Another conclusion from these simulations is regarding the weight that has to be given to the initial estimation of position and velocity, which needs to be very low. This second relative POD process needs to be understood as a way to refine the previously determined orbit of the MEO-2 satellite by means of GNSS satellites which have proven to be in the lower centimeter level in both absolute and relative positioning terms. Thus, the way to configure this refinement is by restraining quite a lot the initial estimations of both position and velocity previously estimated in the absolute POD process. It those initial weights are selected to typical values (m, cm/s) the relative POD is unable to fit the ISL observations due to their high precision (micro-meter level or below). Thus, the algorithm does not converge to the real solution. On the other hand, it has also been concluded that the relative POD process cannot be undertaken by making use of ISL observations only, but GNSS observations need to be available as well to help condition the problem even though they do not provide any extra in terms of relative positioning accuracy. Furthermore, it has also been proven the necessity of estimating empirical accelerations in the along-track component to give the least-squares algorithm more degrees of freedom to help fit the ISL observables. If they are not estimated, the algorithm rejects all the ISL observations and

the solution of the relative POD process is exactly the same as an absolute POD one by means of GNSS observations.

In summary, the main complexity and challenging part of the relative positioning by means of very precise observations of ISL is the conditioning of the LSQ algorithm in which very disperse magnitude orders are processed together (GNSS code, phase, and ISL) along with the estimation of the empirical accelerations. The algorithm is very sensible to any small change in the configuration of the problem and even though following what can be assumed as a correct or proper approach, the algorithm does not work perfectly. In fact, such statement can be proven by the fact that the relative accuracy in the Y axis (cross-track component) seems to be "improved" when the satellites get further from each other away (upper-right of Figure 7-4 and Figure 7-5) instead of presenting the high-amplitude oscillatory behavior seen in the CLO scenario (Figure 7-3). Such behavior is consistent with the specific orbit conditions of this thesis in which the satellites present polar very stable orbits with the same orientation (equal RAAN). In these conditions, the satellites are placed in co-planar orbits and therefore the ISL observations cannot provide any information on such component because there is no visibility. However, due to already quite high conditioning problems of the LSQ algorithm, the fact that both satellites lie in the same orbital plane adds complexity to the case. It is important to note that these orbits are very stable and that they maintain their co-planarity throughout the whole 6-month arc used in the initial propagation of the orbits (Figure 1-2).

Finally, a summary of the results obtained in terms of the relative positioning accuracy is presented below in Table 7-7. It outlines the main differences between the presented case scenarios as have been previously discussed. First, it is safe to state that assuming a given precision of the ISL observations, it can be safely said that the higher the distance between the satellites the lower the accuracy of the relative orbit determination process (mainly affecting the radial and along-track components). In case the accuracy of the relative positioning was required to remain unchanged for any relative distance between the satellites, the precision of the ISL observations would need to be increased. However, in our particular case, a noise lower than the one presented in Table 7-3 was not supported by the software. On the other hand, the instability of the LSQ algorithm used in these relative POD processes due to its complex conditioning added to the fact that the orbits of the satellites are co-planar have resulted in diverse cross-track estimations. From Table 7-7 below, it could look like the cross-track component is fixed as the relative distance between the satellites gets higher but in those cases the small RMS errors probably respond to the finding of a local minimum. In fact, such diverse solutions in the 3 studied cases prove that there is no visibility in such component and that an angular plane separation of the orbits of MEO1 and MEO2 should be induced to obtain a full accurate relative orbit solution.

Please note the use of colors in Table 7-7 is to highlight the scenarios in which the highest accuracy of the relative orbit solution has been obtained. The most precise results are shown in green, the worst ones in red, and the ones in between them are shaded in yellow.

Table 7-7. Comparison of relative position residuals for the 3 case scenarios after relative POD

Scenario		X [mm]	Y [mm]	Z [mm]	Total 3D [mm]	Typical RMS [mm]
CLO	RMS	1.4836	10.5660	1.5827	10.7864	6.2275
MID	RMS	7.9333	1.2940	8.2071	11.4877	6.6324
FAR	RMS	23.1086	1.9064	23.3156	32.8825	18.9847

7.3 Non-coplanar orbits

In this section of the report, different configurations of non-coplanar orbits of MEO-1 and MEO-2 satellites are investigated to check whether the issue of non-visibility in the cross-track component can be solved. This analysis has only been performed for the CLOSE scenario, which provides the most accurate relative POD results.

Given the initial state vectors in Keplerian elements shown in Table 1-1 of both satellites, the following changes have been introduced to the orbit conditions of MEO-2. Please note that the initial state vector and therefore orbit trajectory of the satellite MEO-1 remains unchanged and that both state vectors are referenced to the epoch 01/01/2019 00:00:00 UTC.

1. RAAN = 359 deg (case scenario known as RAAN1)
2. RAAN = 357 deg (case scenario known as RAAN3)
3. RAAN = 350 deg (case scenario known as RAAN10)

It can be deduced that since the initial state vector of MEO-1 is not modified and the only modification to the initial Keplerian elements of MEO-2 is introduced in the RAAN, an initial angular separation between the orbital planes of 1, 3 and 10 degrees will be obtained respectively. Since the determination arcs of these simulations will have the same starting dates as the previously presented like close test case scenario (01/01/2019 12:00:00 UTC), the separation between the orbital planes will not be exactly 1, 3 or 7 degrees but they will be very close to such values (see upper-left of Figure 7-6, Figure 7-7 and Figure 7-8).

Additionally, please note that the relative orbit solutions to be presented in the following subsections have been obtained with the same configuration as shown in Table 7-3, which was used to assess the accuracy of the relative positioning in the so-called CLO, MID, FAR test case scenarios. Finally, the results of the RAAN1, RAAN3 and RAAN10 test case scenarios are presented in sections 7.3.1 to 7.3.3, and they are discussed as well as analysed both individually and as a whole in subsection 7.3.4.

7.3.1 Initial RAAN difference: 1deg

The results for an angular separation between the orbital planes of 1 degree are shown below. In general terms, it can be noticed that the visibility issue of the cross-track has not yet been solved. However, the amplitude of oscillation has been slightly reduced from the co-planar case (Figure 7-3 and Table 7-4).

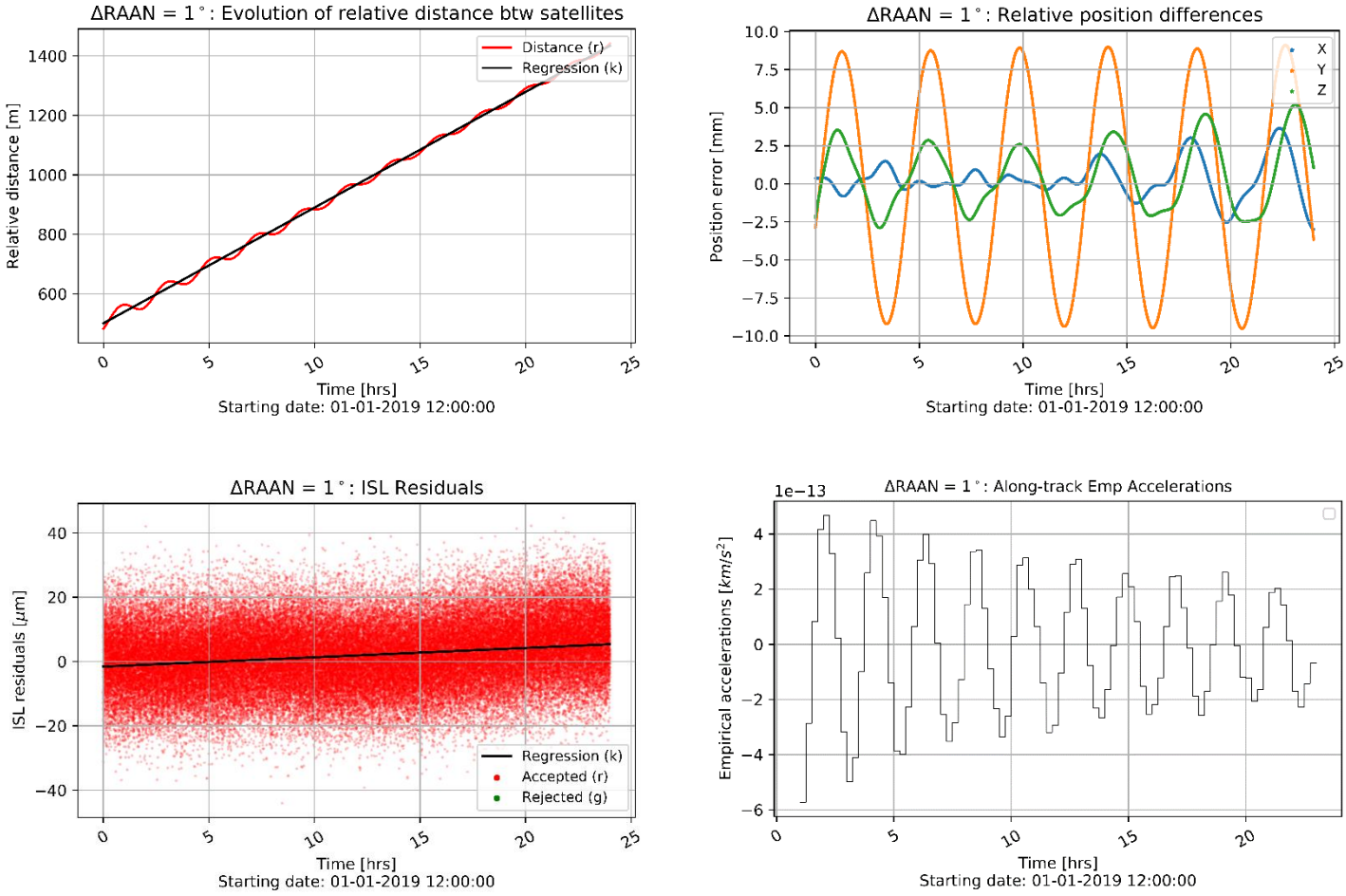

Figure 7-6. Evolution of relative distance (upper-left), relative position errors (upper-right), ISL residuals (lower-left), estimated empirical accelerations (lower-right) (RAAN1)

Table 7-8. Summary of relative position differences

Scenario		X [mm]	Y [mm]	Z [mm]	Total 3D [mm]	Typical RMS [mm]
RAAN1	Mean	0.2943	0.2911	0.5160		
	RMS	1.2471	6.3778	2.2274	6.8698	3.9662
	Max	3.6584	9.1181	5.2166		

7.3.2 Initial RAAN difference: 3 deg

The results for an angular separation between the orbital planes of 3 degrees are shown below. From those results, it can be seen that the precision in the cross-track component has greatly improved in comparison with the nominal co-planar case (Figure 7-4 and Table 7-5). The behaviour in the cross-track component is still oscillatory even though its amplitude has significantly been reduced.

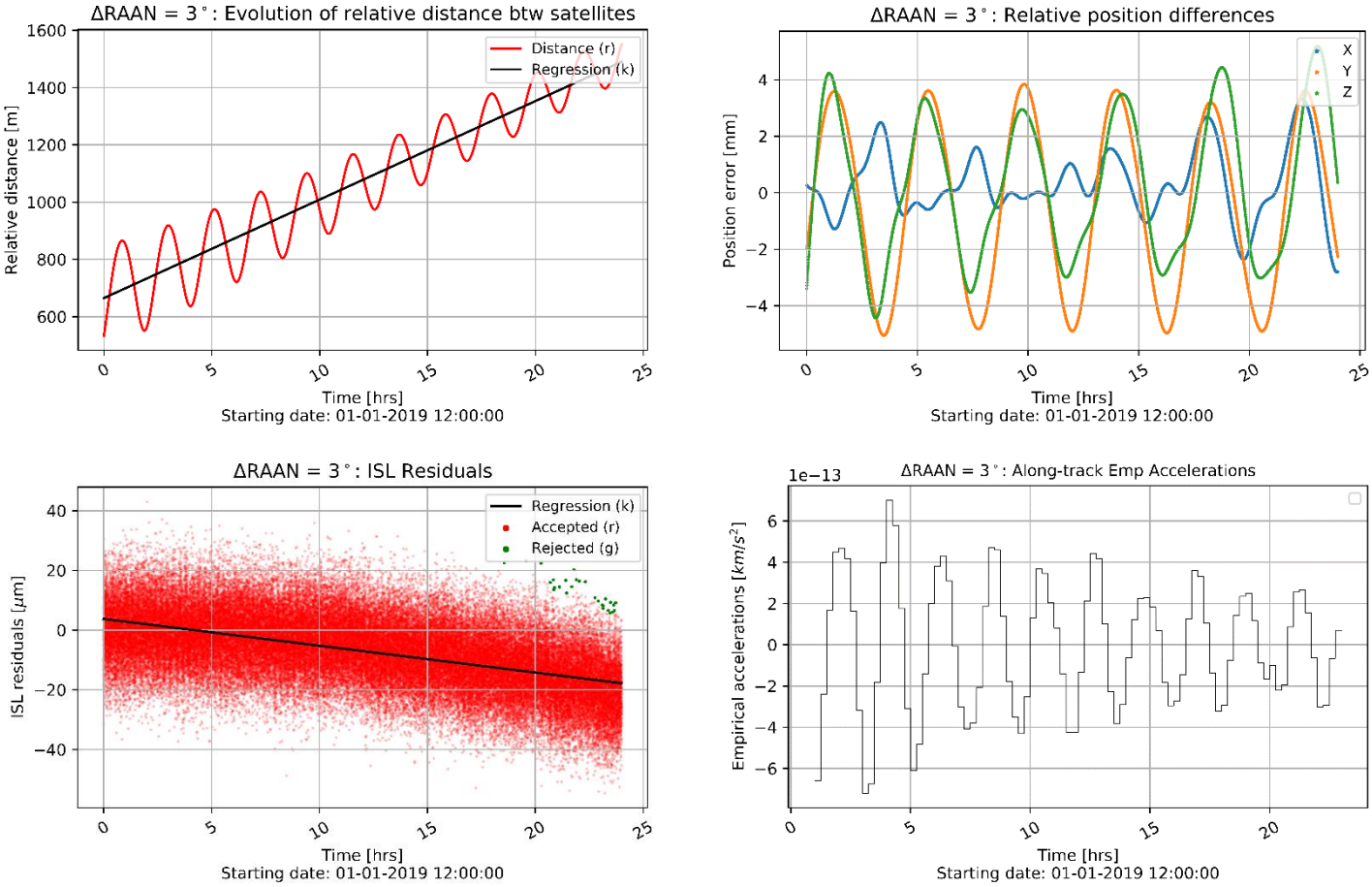

Figure 7-7. Evolution of relative distance (upper-left), relative position errors (upper-right), ISL residuals (lower-left), estimated empirical accelerations (lower-right) (RAAN3)

Table 7-9. Summary of relative position differences

Scenario		X [mm]	Y [mm]	Z [mm]	Total 3D [mm]	Typical RMS [mm]
RAAN3	Mean	0.2985	-0.3586	0.3005		
	RMS	1.2272	2.9714	2.5251	4.0880	2.3602
	Max	3.3117	3.8472	5.1811		

7.3.3 Initial RAAN difference: 10 deg

The results for an angular separation of 10 degrees between the orbital planes are shown below. It can be seen how the position residuals in all 3 components are not oscillatory. This enlightens the fact that there is full visibility between both satellites, especially in the cross-track component. In such component, the accuracy has increased significantly from the nominal co-planar case shown in Figure 7-5 and Table 7-6.

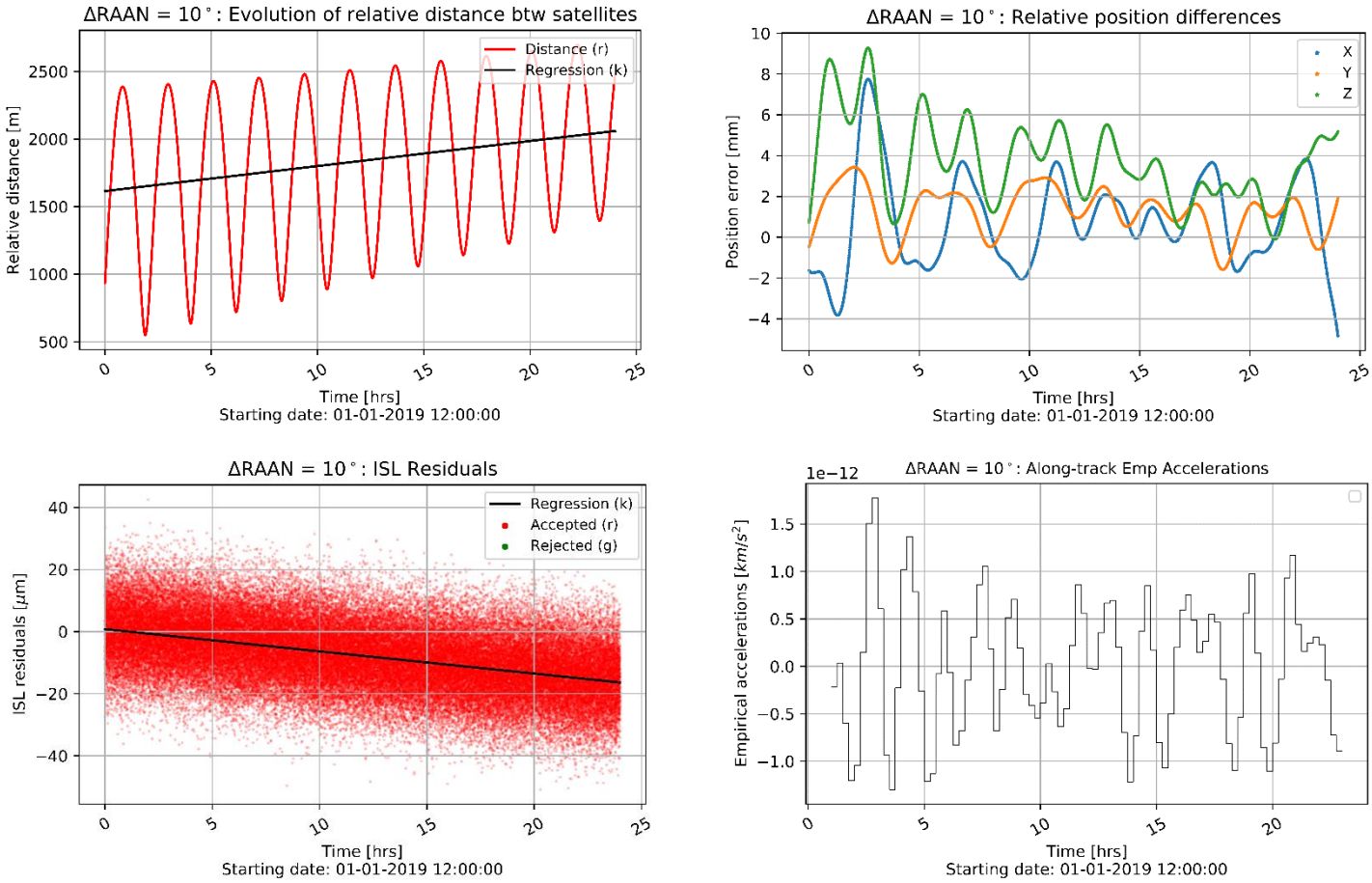

Figure 7-8. Evolution of relative distance (upper-left), relative position errors (upper-right), ISL residuals (lower-left), estimated empirical accelerations (lower-right) (RAAN10)

Table 7-10. Summary of relative position differences

Scenario		X [mm]	Y [mm]	Z [mm]	Total 3D [mm]	Typical RMS [mm]
RAAN10	Mean	0.7683	1.2770	3.7477		
	RMS	2.4439	1.7141	4.2695	5.2096	3.0078
	Max	7.7526	3.4302	9.2694		

7.3.4 Discussion of results

In this section of the chapter, the main goal is to analyze the results presented for the different RAAN configurations to draw conclusions on which approach yields the best relative positioning accuracy. As proceeded previously, the results are to be examined in terms of the relative accuracy in the radial and along-track components which are the directions in which the ISL observations provide more information as well as determining whether or not it was possible to fix the cross-track component of the relative positioning between the satellites. Focusing first on the results obtained for an initial angle separation of 1 degree between orbital planes, it can be seen in mid-left Figure 7-6 that the relative position differences in the cross-track component (Y axis) oscillate with constant amplitude for the whole duration of the determination arc. Even though the amplitude is lower (6.3mm) than it was in the initial close scenario in which the orbits were co-planar (10.6mm), the behavior of the position errors in the cross-track component implies that the angular separation of 1 degree does not provide enough visibility. Under these orbit conditions, the accuracy of the relative positioning in the radial and along-track components are the same order of magnitude (1-2 mm) as it was in the initial co-planar close scenario, see Table 7-11 below. Additionally, it is important to note that during this 24-hr determination arc the relative distance between the satellites goes from 500 to 1400km which are quite low values and can explain the reason behind the high-accuracy obtained in the relative positioning (upper-right Figure 7-6).

Second, when the initial separation between the orbital planes is set at 3 degrees, the position residuals remain in the same order of magnitude as in the RAAN1 test case scenario. As shown in Table 7-11 below, the errors in the X and Z axes are 1.2 and 2.5mm respectively. These position differences in the radial and along-track component imply that even though the initial 3 degrees angle separation between orbital planes increments the range of values of the relative distance in the observation arc (700-1500km) (upper-right Figure 7-7), the ISL measurements can still be fitted properly. Additionally, it seems that the greater angle provides more visibility in the cross-track component because the amplitude of oscillation is reduced dramatically to 3mm (Table 7-11). However, and even though the error in such component has been lowered down due to the 3 degree initial aperture angle between the orbital planes, the fact that these difference still oscillate in time with constant amplitude might suggest that more favourable visibility conditions could still be achieved (mid-left Figure 7-7).

Finally, if the initial angular separation between the orbital planes is set at 10 degrees, the relative position differences look like the ones shown in mid-left Figure 7-8. At first sight it can be noticed how the errors in each of the XYZ axes present a non-oscillatory behavior, in contrast to what had been obtained in the RAAN1 and RAAN3 case scenarios. Additionally, and as shown in Table 7-11, the visibility in the cross-track component is now very high and the RMS of the error has been lowered down to 1.7mm in the Y axis. Additionally, it can be seen how the differences in the X and Z axes have been increased to 2.4 and 4.2mm respectively. This can be explained by the fact that a greater orbital separation carries a greater relative distance between the satellites, in this case it ranges from 1600 to 2100km (upper-right Figure 7-8).

In summary, the fact that the position differences trends in all 3 axes of the RAAN10 scenario do not present an oscillatory behavior, plus the fact that their respective RMS is not higher than a few millimeters are quite solid arguments to consider it as the best configuration. However, RAAN3 scenario also presents very high accurate results as shown in Table 7-11 and could be considered as optimal, even though the behavior of the residuals are quite oscillatory (upper-right Figure 7-7). From this analysis, it can be learnt that in order to achieve high-accuracy solutions in relative positioning, not only do very precise measurements need to be available but there has to be a minimum angle separation between the orbital planes of the satellites. In the particular orbit conditions of this study, such separation has proven to be in between 3 and 10 degrees but it could slightly vary depending on the specifics of each mission. Generally, that minimum orbital plane separation is beneficial when 1D ISL observations are used.

Table 7-11. Comparison of relative position differences for the 3 new RAAN and the initial CLO scenarios

Scenario		X [mm]	Y [mm]	Z [mm]	Total 3D [mm]	Typical RMS [mm]
CLO	RMS	1.4836	10.5660	1.5827	10.7864	6.2275
RAAN1	RMS	1.2471	6.3778	2.2274	6.8698	3.9662
RAAN3	RMS	1.2272	2.9714	2.5251	4.0880	2.3602
RAAN10	RMS	2.4439	1.7141	4.2695	5.2096	3.0078

8

Conclusions & Recommendations

This thesis study has been enclosed in the growing field of POD, focused in shedding light into the challenging and innovative area of relative navigation in medium-Earth orbits. In general terms, progress has been made with regards to the methodology and configuration of relative orbit determination processes when using very precise range measurements such as inter-satellite links. It is safe to say that the work performed in this thesis has indeed achieved the main research goal that involved the exploration of the challenges and limitations of performing relative in high orbital regimes. All the results presented in this document have ultimately tried to give answer and validate the main proposed hypothesis stating that the use of very precise inter-satellite links between a pair of MEO-placed satellites actually improves their relative positioning. The conclusions and future work recommendations that follow from such results are presented in sections 8.1 and 8.2 respectively.

8.1 Conclusions

A summary of the main outcomes can be found in this section. Such conclusions have been structured in three main groups that correspond to the main research questions (RQ) proposed at the beginning of the document in Chapter 1.

GNSS visibility – RQ1

The first steps of this thesis study were to assess the visibility conditions of the GPS and Galileo constellations for a pair of MEO-placed satellites at an altitude of 7,009 and 6,991km respectively. In that regard, it was first unclear which orientation of the receiver antenna would provide with the higher number of contacts with the mentioned GNSS constellations. The main considered antenna orientations were zenith and nadir since the visibility conditions for side-looking antennas proved to be a combination of these two. Zenith-oriented antennas are the most common in all LEO-placed Earth observation missions and nadir-oriented antennas are generally adopted for orbit conditions in which the geometry is not favourable. In the specific orbit conditions of this thesis work, it was found that the altitude of the MEO-placed satellites was quite high and that they were too close to the range of altitudes in which the majority of the GNSS constellations are placed. Thus, the results showed that assuming a nominal zenith orientation for the receiver antenna did not provide the sufficient visibility contacts of the GPS and Galileo constellations to

perform a precise orbit determination process. Contrarily, for a nadir-oriented antenna the visibility conditions were very much improved and the number of contacts increased considerably. The potential complication when assuming a nadir-looking strategy was the fact that the signal-to-noise ratio can be compromised due to the fact that the signals travel much greater distances, can get very close to Earth, be more affected by atmospheric delays and therefore become noisier. To ensure that the observations gained by means of the nadir orientation were of good quality, a minimum threshold value of signal-to-noise ratio was set. Even after setting that requirement, the visibility contacts if assuming a nadir orientation of the receiver antenna were much higher than for a nominal zenith one.

Additionally, taking into account the side lobes of the emitter antennas of both GPS and Galileo satellites was also studied. The results showed that considering them yields an increase in the number of visibility contacts that are over the minimum threshold set for the signal-to-noise ratio. In this case, it was vital to include such threshold because the consideration of side lobes will generally guarantee an increase in the visibility contacts but the goal of this analysis was to ensure that the extra observations had an acceptable noise level and could later be used in the POD processes. Besides, an analysis was performed to assess the impact of the minimum grazing altitude on the total number of visibility contacts. In that regard, two possibilities were considered: 100 and 1000km to rule out the tropospheric and ionospheric-affected observations respectively. As expected, as the grazing altitude was higher, the number of visibility contacts was decreased. It was finally decided to set the value at 100km since the drop of observations was quite critical when placing it at 1,000km in an effort to get rid of all signals travelling across Earth's ionosphere.

Finally, to find the configuration that would optimize the number of contacts, a combination of antennas in different orientations was analysed. It was found that the best configuration was to include a pair of antennas that would look towards free-space and Earth (zenith and nadir). It was also found that including antennas in the other two remaining directions did not provide an increase of observations since they were coupled with the nadir and zenith-orientations. After the analysing these results and due to the fact that the satellite was required to be equipped with a single antenna oriented in one direction, the final selected visibility configuration would consider the side lobes gain pattern of the emitter GPS and Galileo satellites, a nadir-oriented receiver antenna and a grazing altitude of 100km.

Absolute POD – RQ2

The approach of this thesis work was to perform absolute POD to the pair of MEO-placed satellites and use those orbits as starting points for the relative POD processes that would then focus on just refining the relative orbit accuracy by means of the use of very precise ISL ranging measurements. In real-life conditions, the POD processes in which the trajectory of a given user satellite is determined are affected by numerous errors that compromises the accuracy of the absolute orbit solution. In this thesis work, it was desired to assess the impact of a given set of realistic error sources to achieve an accuracy in the orbit solutions that could simulate the ones found in state-of-the-art missions. Furthermore, it is important to note that the presence of error sources that perturb the orbit solution in absolute terms of each of the satellites will also likely result in a non-precise relative orbit solution. The resulting relative positioning error level is used as the starting point to assess the impact of using additional ISL observations for relative POD.

The impact of inaccuracies in the centre of mass, antenna reference point and cross-sectional area in the absolute orbit solutions have been assessed through Monte Carlo simulations. These quantities were perturbed from their reference values following a normal distribution with a specific standard deviation value (sigma) for a total of 50 times. The conclusion was that the impact of an error in the centre of mass and antenna reference point was much higher than for inaccuracies in the area of the satellite. The high correlation between the cross-sectional area and the solar radiation pressure coefficient would make the estimation of the latter to balance for any introduced error in the area and thus the orbit solution was very close to the real true one. However, the almost-null correlation between the centre of mass and antenna reference point and the SRP coefficient would generally translate into errors in the absolute solution of a few centimetres in 3D. The highest inaccuracies were found in the along-track due to perturbations in the S axis of the fixed-body frame. Regarding uncertainties in the geopotential model and GNSS orbits and clock, their impact was assessed by using slightly different models and providers. While

the final accuracy of the orbit solutions for the two different geopotential models used was no higher than a few millimetres, the use of different precise GPS and Galileo orbits and clocks induced an error in the low-centimetre level in 3D, with the cross-track having the largest inaccuracy.

Finally, the inclusion of all error sources at the same time impacted the accuracy of the absolute orbit solution of both MEO-satellites and up to the 3-4 centimetre level in 3D, a level of accuracy observed in other real-life on-going missions.

Relative POD – RQ3

The assumed architecture was a two-way optical inter-satellite ranging system. Besides, the main conclusion from the relative POD results chapter (Chapter 7) is that, in general terms, it seems that the use of ISL helps in improving the relative orbit accuracy between the satellites. To achieve so, the initial relative orbit solution has to be greatly constrained and 15-minute constant piece-wise empirical accelerations in the along-track component had to be estimated. However, it is important to bear in mind that even though the work performed in this thesis work points in that direction, there are still many challenges and questions to answer as specified in the future work recommendations section.

Regarding the achieved relative accuracy, it was shown to depend on the relative distance between the two MEO satellites. First, for the case in which the satellites were close to each other (1,000km), the relative accuracy in the radial and along-track component went down to the 1mm level, improving quite a lot the initial relative accuracy that was obtained by means of the absolute POD process with GNSS observations only. As the relative distance between the satellites was increased, the impact of the ISL in the relative orbit solutions has become lower as proven in the MID and FAR case scenarios (10,000 and 20,000km respectively). In the MID scenario, the relative accuracy in radial and along-track components has been placed in the high millimetre level improving the initial relative solution. In the FAR scenario, the solution is almost identical to the initial one and the impact of the ISL seems to be almost null. Even more precise ISL seem to be required to improve the relative POD for these very long baselines.

Additionally, in all cases, the relative POD is not able to provide a good estimate of the cross-track component due to the fact that they are placed in co-planar orbits and this direction is not sensed by the 1D ISL observations. Nevertheless, the precision of the cross-track component estimation seems to change quite a lot from one scenario to another which could be due to the critical conditioning of the LSQ matrix that can lead to the finding of a local minimum. However, our understanding and knowledge of this feature is still limited and would require to be further studied in detail.

Finally, it was shown that a relative POD accuracy at the low millimetre level was obtained for all orbit components (radial, along-track, cross-track) for a relative distance of around 1,000km and for an angular separation of the orbital planes of 10 degrees. In this regard, it can be concluded that with the approach and configuration followed in this master thesis and in order to obtain an overall improvement in the relative orbit accuracy, the distance between the satellites has to be low and there has to be a minimum separation between the planes of the orbits. For longer baselines, further research has to be carried out especially focusing in the conditioning of the LSQ matrix, estimation of empirical accelerations and improvement of the software tool to allow for higher precision accuracies of the ISL observations.

8.2 Future work recommendations

The field of precise relative orbit determination is quite recent and yet to be fully explored. Nevertheless, this master thesis has focused in trying to prove that it is indeed possible to obtain very precise relative orbit accuracies by means of the innovative inter-satellite link technology, which allows to obtain high precision range observations between the satellites. The challenges faced in this thesis' work lead to future work recommendations in the different areas of knowledge

that have been part of the study. These recommendations have been structured in the following way: GNSS visibility, Absolute POD and Relative POD.

GNSS visibility

Firstly, it has been proven that the visibility of GNSS constellations is not optimal for MEO-placed satellites, so more GNSS constellations should be considered to improve the visibility conditions. In that regard, other global systems like GLONASS and BeiDou when the third generation is fully operational by 2020. A thorough analysis should be performed in order to determine how much the gain will be in comparison to the conditions of the visibility simulations of this master thesis in which only GPS and Galileo were considered. Additionally, the possibility of using GNSS satellites in GEO or IGSO orbits (e.g. QZSS and IRNSS) to improve the visibility of the GNSS constellations would also be an interesting study. The results of the analysis could be compared against the current visibility conditions of MEO-placed satellites and determine whether or not it is worth it to consider such scenario. Additionally, it has to be considered as well the expected accuracy of the different GNSS constellations; in particular the products of GEO satellites are less precise (Kazmierski et al., 2018). For those improved visibility conditions, a slightly higher grazing altitude than 100km could be investigated. A more thorough and realistic simulation of the ionospheric error could be carried out to investigate how big of a problem this is and to determine an even more optimal grazing altitude.

Absolute POD

Further research study is required to better understand the impact of uncertainties in the geopotential model in the final absolute orbit solution. In this thesis study, two different geopotential have been compared against the one used in the generation of the real orbits of the satellites, which is considered as state-of-the-art in operations of current missions such as the Sentinels. However, such comparison has only been performed for a specific day and given the fact that the orbits are quite stable along with a quite high period, does not cover all Earth's geopotential. It would be nice to try to assess the difference in impact for the inaccuracies in the models for a higher number of revolutions or run multiple test cases after varying the initial RAAN of the orbits to assess other areas of the Earth's geopotential, or different epochs to assess the impact of the extrapolate the time-variable coefficients.

It would also be advisable to increase the knowledge on the discrepancies that appear in different solutions of precise ephemeris and clock data of the GNSS constellations, especially assessing their impact on the orbit determination process accuracy. In this particular study, GNSS orbits and clocks from the University of Bern (Switzerland) were used in the generation of the code and phase and observables and the GNSS orbits and clocks calculated by CNES were used in the orbit determination process. In that regard, it would also be advisable to assess the discrepancies between European sources of GNSS products (Bern, CNES) with other non-European ones like the ones provided so far by the Jet Propulsion Laboratory (JPL) in Pasadena, CA. Then, the difference in impact of the non-European products could be compared against the ones used in the calculations of this master thesis. Furthermore, in order to fully complete the analysis performed in this thesis, several 1 day 24-hr observation arcs could be considered to gather more understanding on how the discrepancies in GNSS orbits and clocks ultimately impact the accuracy of the absolute POD process.

The further investigation of POD with a combination of different GNSS systems is recommended. The possibility to estimate a proper working inter-system bias to erase the code residuals offset should be pursued. Moreover, investigating the impact of more realistic satellite model errors when such information is available, would be worthwhile.

For a nadir-looking orientation of the MEO-placed satellites, the signal from the GNSS satellites can potentially get really close to the Earth's surface and travel across the different layers of the ionosphere. Due to the geometry of the problem, it has been researched that existing models like IRI or Klobuchar do not perform well. The precise modelling of the ionosphere would allow to include this delay in the generation of the GNSS observables for this specific path of the signals, to make them more realistic. Further research on the modelling of the ionospheric delay for the specific geometries of GNSS tracking of MEO-placed satellites with nadir-looking antennas would

be beneficial. In that regard, the onion-peeling approach seems like a promising and feasible option.

Relative POD

First, the limiting factors of the NAPEOS software should be addressed. Further research on the conditioning of the LSQ algorithm is required. The coupling of quantities that are very diverse in magnitude such as ISL residuals with respect to GNSS phase and code as well as constant piece-wise empirical accelerations with respect to the position and velocity estimates could be further investigated. Additionally, developments and improvements have to be included in the software tool so that it can process higher-precision ISL measurements, closer to current state-of-the-art precisions that are placed in the nanometre level. Future investigation on the techniques to arrive to such precision levels in the measurements needs to be performed, to determine whether it can be achieved by means of ranging, Doppler or both. Hence, being able to work with such low precisions would show whether or not is the relative orbit solution's accuracy in the MID and FAR case scenarios of this thesis limited by the micro-meter level precision of ISL used in the simulations.

Second, it would be advisable to further investigate the impact of the estimated empirical accelerations in the relative POD processes by means of ISL. In the work performed in this mater thesis, they have been proven to be vital in allowing the sufficient degrees of freedom to the LSQ algorithm to fit very precise observations such as the inter-satellite links. However, further research on the optimum configuration of these empirical accelerations and their fit in the relative POD process could be a key to the future of precise relative navigation. For instance, the investigation of the use of CPR empirical accelerations in the relative POD processes could yield better results in terms of accuracy since they could emulate the oscillating behaviour of the orbit position residuals that have appeared in the majority of the studied test case scenarios.

Furthermore, increasing knowledge on the feasibility of application of other inter-satellite link architecture systems would be very valuable. For instance, shedding light on the use of one-way ranging methods, generally simpler and cheaper, as well as the challenges that come along with them would also be advisable. In that regard, the minimum clock synchronization between the satellites that allow the LSQ algorithm to fit the ISL observations could be investigated. Additionally, the sensitivity of the relative orbit accuracy to the synchronization of the satellites' clocks shall also be explored. Presumably, such analysis will conclude that a very precise clock synchronization is required and therefore ways to achieve that goal should be researched.

Finally, and following one of the main challenges faced in this thesis, a follow-on study in the fixing of the cross-track component in relative navigation for satellites in co-planar orbits should be performed. The results obtained from these simulations indicate that it is not possible to control such component when applying a relative POD process by means of ISL even though GNSS observations are processed along with it. It is important to stress that placing the satellites in different orbital planes has proven to be the best approach, however it could be the case that the co-planarity of the satellites' orbits is a big requirement. In those cases, the use of relay satellites in which the optical signal would receive the signal from the main satellite and reflect it towards the secondary satellite could be an option.

Bibliography

[1] Aghav S.T., Gangal A.G. (2014) Simplified Orbit Determination Algorithm for Low Earth Orbit satellites using spaceborne GPS navigation sensor. *Artificial Satellites*, *49*(2)

[2] Alawieh, M., Hadaschik, N., Franke, N., Mutschler, C. (2016) Inter-Satellite Ranging in the Low Earth Orbit. *10th International Symposium on Communication Systems, Networks and Digital Signal Processing (CSNDSP)*. IEEE

[3] Amanor D., Edmonson W., Afghah F. (2018) Inter-Satellite Communication System based on Visible Light. *IEEE Transactions on Aerospace and Electronic Systems, 54(6)*

[4] Balakrishnan K. (2013) Inter-satellite ranging for geodesy, formation flying, and fundamental physics in space. Department of Aeronautics and Astronautics: Standford University

[5] Bauer F. H. (2015) GPS Space Service Volume (SSV). FBauer Aerospace Consulting Services (FB-ACS). *15th PNT Advisory Board Meeting*

[6] Berruti B., Banos T. (2016) Sentinel-3 satellite to Precise Orbit Determination Interface Control Document. *Ref: S3-ID-TAF-SC-01290*. Thales Alenia Space Internal Document.

[7] Berzosa J., Fernandez J. et al (2018) Copernicus POD Service: First Orbit Determination Results for Sentinel-3B. 24-29 September 2018, Ponta Delgada, Azores, Portugal.

[8] Bonnor N. (2012) A Brief History of Global Navigation Satellite Systems. *Royal Institute of Navigation: the Journal of Navigation*. DOI: 10.1017/S0373463311000506

[9] Carrou J.P. (1995) *Spaceflight Dynamics Volumes I et II*. Centre Nationale d'Études Spatiales. ISBN: 2.85428.378.3

[10] Cecconi, B., Dekkali M., Briand C., Segret B. et al (2017) NOIRE Study Report: Towards a Low Frequency Radio Interferometer in Space. *2018 IEEE Aerospace Conference* (pp. 1-19). IEEE

[11] Chapagain N.P. (2016) Ionosphere and its Influence in Communication Systems. Research Gate: Tribhuvan University, Nepal

[12] Chen L., Bai X., Liang, Y., & Li, K. (2016). Orbital Prediction Error Propagation of Space Objects. *Orbital Data Applications for Space Objects* (pp. 23-75). Springer, Singapore. doi:10.1007/978-981-10-2963-9_2

[13] Chen L., Li K., Bai X. (2017) *Orbital Data Applications for Space Objects* (p. 166). Springer: Berlin/Heidelberg, Germany.

[14] Dahl C., Baatzsch A., Dehne M., Gilles F., et al. (2016) Laser ranging interferometer on Grace follow-on. *International Conference on Space Optics*. Biarritz, France

[15] Danzmann K. (2017) Laser Interferometer Space Antenna: LISA. Albert Einstein Institute Hannover.

[16] Darbeheshti N., Wegener H., Muller V., et al. (2017) Instrument data simulations for GRACE Follow-on: observation and noise models. *Earth System Science Data Discussions.*

[17] Degnan J. (2011) The history and future of Satellite Laser Ranging. *17th International Workshop on Laser Ranging*, Bad Kotzting Germany.

[18] Dirkx, D. (2015) Interplanetary Laser Ranging. Analysis for Implementation in Planetary Science Missions. Delft University of Technology, Delft (the Netherlands)

[19] Doeleman S.S. (2017) Seeing the unseeable. *Nature Astronomy Journal*. DOI: 10.1038/s41550-017-0278-y

[20] Doornbos, E. (2012) *Thermospheric density and wind determination from satellite dynamics*. Impskemp Drukkers: ISBN 978-90-9026051-8

[21] Dwidar H.R., Owis A.H. (2013) Relative Motion of Formation Flying with Elliptical Reference Orbit. *International Journal of Advanced Research in Artificial Intelligence, Vol. 2, No. 6*

[22] Elmas Z.G., Aquino M., Marques H.A., Monico J.F.G. (2011) Higher order ionospheric effects in GNSS positioning in the European region. *Copernicus Publications on behalf of the European Geosciences Union. Volume 29, issue 8*

[23] ESA Navipedia (2018). GPS General Introduction. https://gssc.esa.int/navipedia/index.php/GPS_General_Introduction

[24] ESA Navipedia (2018). Ionospheric Models for Single Frequency Receivers. Available at https://gssc.esa.int/navipedia/index.php/Ionospheric_Models_for_Single_Frequency_Receivers
[25] ESA Navipedia (2020). Reference Systems and Frames. Available at https://gssc.esa.int/navipedia/index.php/Reference_Systems_and_Frames
[26] European Space Agency: Directorate of Operations and Infrastructure (2009) NAPEOS: Mathematical Models and Algorithms. European Space Operation Centre ESOC. *DOPS-SYS-TN-0100-OPS-GN*
[27] European Space Research and Technology Centre (2018) Statement of Work: Precise Relative Navigation in MEO to Support Science Missions. *NAVISP1-SOW-ESA-024-00001*
[28] European Union (2010) The European GNSS (Galileo) Open Service Signal in Space Interface Control Document. *OS SIS ICD, Issue 1.1*
[29] European Union (2019) European GNSS (Galileo) Open Service – Service Definition Document. *Signal in Space. Interface control document, issue 1.1*
[30] Feltens, J. (1999) Chapman Profile Approach For 3D Global Representation. ESA, European Space Operations Centre. Darmstadt, Germany
[31] Fernandez J. et al (2019) *Copernicus POD Regular Service Review Jun-Sep 2019: Copernicus Sentinel-1, -2 and -3 Precise Orbit Determination Service* (SENTINELSPOD). Version: 1.0. Date: 31/10/2019
[32] Fernandez Sanchez J., Peter H., Femenias P. (2018) The Copernicus POD Service. *COSPAR 2018, 16th July*. Pasadena, USA
[33] Fernandez, J. (2017) GNSSSim Software Report. GMV Internal Document: *GMV-GNSSSIM-SWR-001*
[34] Fernandez, L. (2010) Simulating Ionosphere Scintillation effects. Potential applications for future Earth observation missions. GMV Aerospace and Defence. Madrid, Spain.
[35] Gao Y., Liu Z. Z. (2002). Precise ionosphere modeling using regional GPSNetwork data. Journal of Global Positioning Systems. Vol. 1, No.1
[36] Global Navigation Satellite Systems Engineering, Policy and Design (2019). International Committee on GNSS-13 Focuses on PNT in High Earth Orbit and Beyond. https://insidegnss.com/international-committee-on-gnss-13-focuses-on-pnt-in-high-earth-orbit-and-beyond/
[37] GPS Basics (2001). Module 2: Global Positioning System, Lecture 9: GPS Errors and Accuracy. Available at https://nptel.ac.in/courses/Webcourse-contents/IIT-KANPUR/ModernSurveyingTech/lectureB_9/B_9_8clockbias.html
[38] Guo X., Geng J., Chen X., Zhao Q. (2019) Enhanced orbit determination for formation-flying satellites through integrated single- and double-difference GPS ambiguity resolution. *GPS Solutions, 24(1)*. doi: 10.1007/s10291-019-0932-1
[39] Hegarty C.J. (2012) GNSS signals — An overview. *IEEE International Frequency Control Symposium Proceedings*, Baltimore, MD
[40] Heinzel G. (2019) The Laser Ranging Interferometer on GRACE Follow-On. In *Geophysical Research Abstracts* (Vol. 21).
[41] How J, Lawson L. G. (1996) GPS as a Structural Deformation Sensor. Department of Aeronautics and Astronautics, Stanford University, Stanford CA.
[42] International GNSS Service (2020) IGS Antex Maps available at ftp://ftp.igs.org/pub/station/general/
[43] Jaggi A., Beutler G., Hugentobler U. (2005) Efficient Stochastic Orbit Modeling Techniques using Least Squares Estimators. In *A Window on the Future of Geodesy (pp. 175-180)*. Springer, Berlin
[44] Jakowski, N. (2005) Ionospheric GPS radio occultation measurements on board CHAMP. *GPS Solutions*, *9*(2), 88-95. DOI 10.1007/s10291-005-0137-7
[45] Jet Propulsion Laboratory (2019) Gravity Recovery and Climate Experiment Follow-On (GRACE-FO). *Level-3 Data Product User Handbook.* California Institute of Technology.
[46] Jiang F., Li J., Baoyin H. (2007) Approximate analysis for relative motion of satellite formation flying in elliptical orbits. *Celestial Mechanics and Dynamical Astronomy*, *98*(1), 31-66. doi: 10.1007/s10569-007-9067-8
[47] Jin et al., S., Cardellach E., Xie F., (2014). *GNSS Remote Sensing: Theory, Methods and Applications*. Springer.
[48] Kansowa T., Tatnall A. (2010) Earth tides and earthquake. Proc. 'Fringe 2009 Workshop'. Frascati, Italy.

[49] Kaplan E.D., Hegarty C.J.. (2006) *Understanding GPS. Principles and Applications*. Artech House: Boston, London
[50] Kazmierski K., Sośnica K., & Hadas T. (2018). Quality assessment of multi-GNSS orbits and clocks for real-time precise point positioning. *Gps Solutions, 22(1)*
[51] Kur T., Kalarus M. (2018) Exploitation of the Inter-Satellite Link in precise orbit determination. *EGU General Assembly Conference Abstracts, Vol. 20*
[52] Lee, S.S. (2009) *Dynamics and Control of Satellite Relative Motion: Designs and Applications*. Virginia Polytechnic Institute and State University.
[53] Leitinger R., Zhang M. L. Radicella S. M. (2005). An improved bottomside for the ionospheric electron density model NeQuick. *Annals of Geophysics. Vol 48, N. 3*
[54] Liu R., Liu M, Cao X., Liu Y. (2018) Optimal sliding mode tracking control of spacecraft formation flying with limited data communication. *Advances in Mechanical Engineering*, *10*(6). doi: 10.1177/1687814018782048
[55] Ma X., Tang C., Wang X. (2019) The evaluation of IRNSS/NavIC system's performance in its primary and secondary service areas-data quality, usability and single point positioning. *Acta Geodaetica et Geophysica 2019 54:55-70*. doi: 10.1007/s40328-019-00246-8
[56] McCarthy D.D., Petit G. (2003) *IERS Conventions. Chapter 6: Geopotential*. Technical Note: No.32.
[57] Memarzadeh, Y. (2009) *Ionospheric modeling for precise GNSS applications*. NCG, Nederlandse Commissie voor Geodesie.
[58] Mohr P. J., Taylor B. N., & Newell D. B. (2008). CODATA recommended values of the fundamental physical constants: 2006. *Journal of Physical and Chemical Reference Data. Vol. 80, No. 3*
[59] Montenbruck, O., Gill, E. (2000) *Satellite Orbits: Models, Methods and Applications*. Springer
[60] Mountcastle P. (2002) Monte Carlo simulation of ionospheric scintillation. *IEEE National Radar Conference*. DOI: 10.1109
[61] National Aeronautics and Space Administration & European Space Agency (2019) Laser Interferometer Space Antenna (LISA) available at https://lisa.nasa.gov/
[62] National Aeronautics and Space Administration (2019) Gravity Recovery and Climate Experiment Follow-On. Tracking Earth's Mass in Motion. available at https://gracefo.jpl.nasa.gov/
[63] Nava B., Biernat H., Putz Dr. (2012) Data Assimilation into Ionospheric Models. Karl-Franzens-University Graz, Austria
[64] Official US government about the Global Positioning System (2019): Space Segment. available at https://www.gps.gov/systems/gps/space/
[65] Otten M. (2008) ESOC Activities within the IDS ESA/ESOC. *IDS AWG Meeting*. Paris, France
[66] Pérez, J. et al. (2015) *Overview of Galileo System. GALILEO Positioning Technology*. Springer: Netherlands
[67] Poore A.B., Horwood J. T., Aristoff J. M., Armellin R. (2016) *Covariance and Uncertainty Realism in Space Surveillance and Tracking*. Numerica Corporation. Fort Collins, Colorado (USA)
[68] Radicella S.M., Zhang M. (1995). The improved DGR analytical model of electron density height profile and total electron content in the ionosphere. *Annali di geofisica, Vol. XXXVIII, N. 1*
[69] Ranieri, S. (2016) Inter-Satellite links and ARES capabilities. ARES Consortium. Available at http://www.ares-consortium.org/It/wp-content/uploads/2016/10/13.10.16-ISL-ARES-Capabilities-.pdf
[70] Revnivykh, S. (2010). GLONASS status and progress. *Proc. ION GNSS (pp. 609-633).*
[71] Sanchez Sobrino, J.A. (2010) Observables GPS. X Curso de GPS de Geodesia y Cartografia. Montevideo, Uruguay
[72] Sanz J., Juan J.M., Hernandez-Pajares M. (2013). *GNSS Data processing. Volume I: Fundamentals and Algorithms*. ESA.
[73] Schutze D., Heinzel G., Gerberding O., Danzmann K. (2014) Laser beam steering for GRACE Follow-On intersatellite interferometry. *Optics express*, *22*(20). doi:10.1364/OE.22.024117
[74] Shah, V., Patel R., Nayak, R. (2017) Short Range Inter-Satellite Link for Data Transfer and Ranging using IEEE802.11n. *International Journal of Computer Applications (0975-8887) Volume 164 – No 1.*

[75] Sheard, B.S., Heinzel G., Danzmann K., Shaddock D.A., Klipstein W.M., Folkner W.M. (2012) Intersatellite laser ranging instrument for the GRACE follow-on mission. DOI 10.1007/s00190-012-0566-3

[76] Sokolovskiy S. (2003) Effect of superrefraction on inversions of radio occultation signals in the lower troposphere. *Journal of Geodesy*, *86*(12). doi: 10.1029/200RS002728

[77] Someswar M., Rao S., Chigurukota D. (2013) Global Navigation Satellite Sustems and Thier Applications. International Journal of Software and Web Sciences. ISSN (Online): 2279-0071

[78] Sośnica, K., Thaller, D., Dach, R., Steigenberger, P., Beutler, G., Arnold, D., & Jäggi, A. (2015). Satellite laser ranging to GPS and GLONASS. *Journal of Geodesy, 89(7), 725-743*

[79] Stankov S.M., Norbert J., Heise S., Muhtarov P., Kutiev I., Warnant R. (2003) A new method for reconstruction of the vertical electron density distribution in the upper ionosphere and plasmasphere. *Journal of Geophysical Research, Vol. 108, No. A5, 1164*. doi:10.1029/2002JA009570

[80] Štěpánek P., Bezděk, A., Kostelecký, J., & Filler, V. (2016). Gravity field and ocean tides modeling for precise orbit determination of DORIS satellites. *Acta Geodyn and Geomater. Vol. 13, No.1*

[81] Stetter M., Hugentobler U., Schlicht A. (2017) Optical Inter-Satellite Links for Global Navigation Satellite Systems. *IGS Workshop 2017*: TU Munchen

[82] Sun, R., Maessen, D., Guo, J., Gill, E. (2010) Enabling Inter-Satellite Communication and Ranging for small satellites. In *9th Symposium on Small Satellites Systems and Services, Funchal, Portugal* (Vol. 31).

[83] Tang Y., Wang Y., Chen J. (2016) The Availability of Space Service for Inter-Satellite Links in Navigation Constellations. *Sensors*, *16*(8). doi: 10.3390/s16081327

[84] Tapley B., Schutz B., Born G. H. (2004) *Statistical Orbit Determination*. Elsevier Academic Press

[85] Teunissen, P., & Montenbruck, O. (2017). *Springer handbook of global navigation satellite systems*. Springer.

[86] Tuna, H., Arikan O., Arikan F., Gulyaeva T. (2013) Estimation of 3D Electron Density in the Ionosphere By Using Fusion of GPS Satellite-Receiver Network Measurements and IRI-Plas Model. *16th International Conference on Information Fusion*. Istanbul, Turkey

[87] United Nations: Office for outer space affairs (2018) *The Interoperable Global Navigation Satellite Systems Space Service Volume.* United Nations Office at Viena

[88] Visser P., van Helleputte T. (2007) GPS-Based Reduced Dynamic Orbit Determination Using Accelerometer Data. *NASA Technical Reports Server. ID: 20080012719*

[89] Wu J., Wu S., Hajj G., Bertirguer W., Lichten S. (1992) Effects of antenna orientation on GPS Carrier Phase Measurements. *Manuscripta Geodaetica*

[90] Xie, J., & Liu, T. (2013). Research on technical development of BeiDou navigation satellite system. *China satellite navigation conference (CSNC) 2013 proceedings.* Springer, Berlin, Heidelberg.

[91] Yang D., Yang J., Li G., Zhou Y, Tang CP. (2017) Globalization highlight: orbit determination using BeiDou inter-satellite ranging measurements. *GPS Solutions*, *21*(3). doi: 10.1007/s10291-017-0626-5

[92] Yang Y., Hu X., Chen G. et al (2019) Inter-Satellite Link Enhanced Orbit Determination for BeiDou-3. *The Journal of Navigation*, *73*(1). doi: 10.1017/S0373463319000523

[93] Zhang Q., Yang W., Zhang S., Yao L. (2018) Performance Evaluation of QZSS augmenting GPS and BDS Single-Frequency Single-Epoch Positioning with Actual Data in Asia-Pacific Region. *International Journal of Geo-Information*. doi:10.3390/ijgi7050186

[94] Zhou Y., Wang Y., Huang W., Yang J., Sun L. (2018) In-orbit performance assessment of BeiDou intersatellite link ranging. *GPS Solutions, vol. 22, p. 119.*

Appendix A

The Montecarlo simulations carried out to assess the impact of different error sources in the accuracy of the final absolute orbit solution were presented in section 6.3. At first, the influence of each of the error sources in the 3D accuracy was examined and then the analysis was carried out component-wise. In the latter section, the results for certain sources of error (center of mass, antenna reference point) were not presented in all components but only in the one in which the impact on the orbit solution was more representative. In this annex, the results of the 4 remaining simulations which represent the accuracy loss induced by inaccuracies in the R and W components of both centre of mass and antenna reference point expressed in the body reference frame.

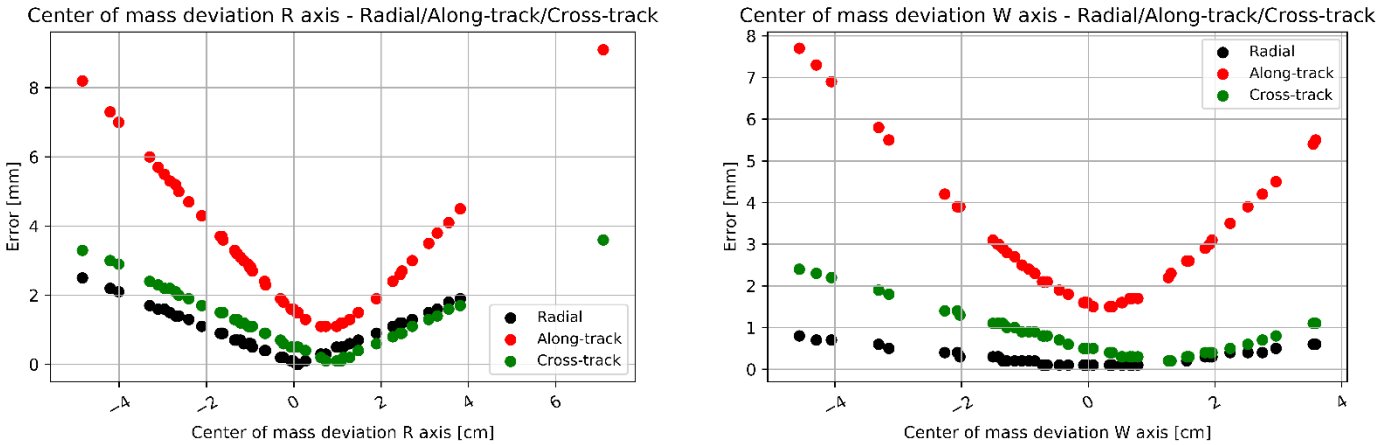

Figure A 1. Impact of deviation in R axis (left) and W axis (right) of center of mass in final orbit solution accuracy expressed in radial, along-track and cross-track components

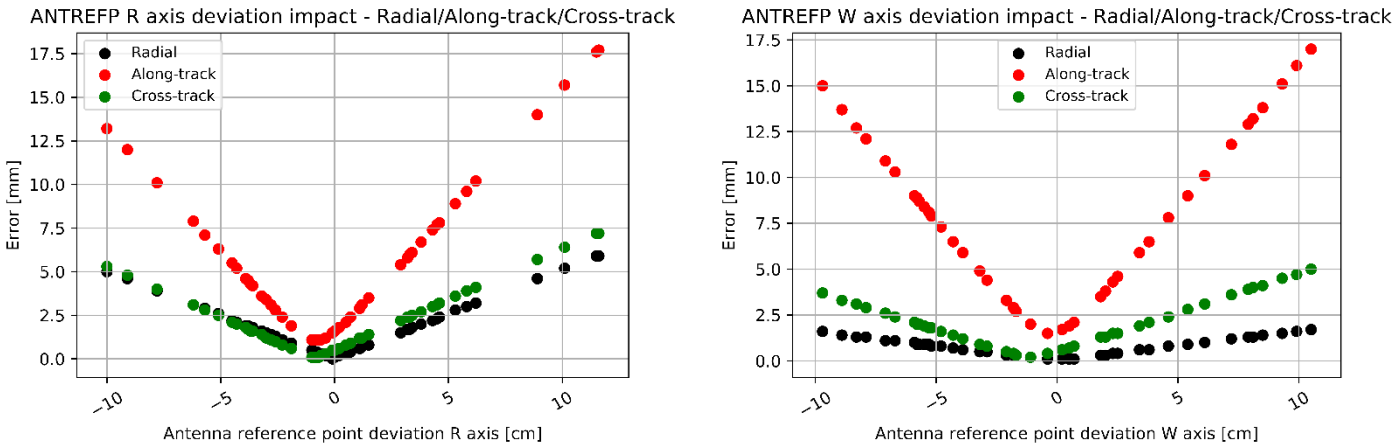

Figure A 2. Impact of deviation in R axis (left) and W axis (right) of antenna reference point in final orbit solution accuracy expressed in radial, along-track and cross-track components

Appendix B

The simulations carried out for the means of this thesis work have been performed in the framework of NAPEOS, a leading POD software tool mainly developed by ESA with the collaboration of GMV. The aim of this appendix is to give an overview of the different programs that were more relevant to the purpose of this thesis work. It is also worth mention that the computer language used in NAPEOS is Fortran90, a very antique programming language that characterizes for presenting a very high compiling speed which makes it very suitable for high-power demanding applications. Even though it is not an easy programming language to work with, there are many applications in the industry that require and make use of it.

Programs

The main programs that allow the NAPEOS software to have the functionalities previously presented have been divided into processing, simulation and comparison tools. Thus, the aim is to review such tools to get an understanding of the different blocks and steps that take part in the process of orbit determination within the specifics of NAPEOS. As it is known, the input data needed to carry out an absolute POD process are observations (pseudorange & carrier phase) and the ephemeris data of the corresponding GNSS constellation satellites. In a real case scenario, these input files are provided by the user but in this case they have all been generated.

Simulation tools

GnssSim is in charge of simulating GNSS observables. In that regard, it is able to generate both code and phase observables from any GNSS constellation (GPS, Galileo, GLONASS, BeiDou, QZSS, and IRNSS) and for any Earth's-orbiting receiver (LEO, MEO and GEO). Please note that the output file of this block is a RINEX file.

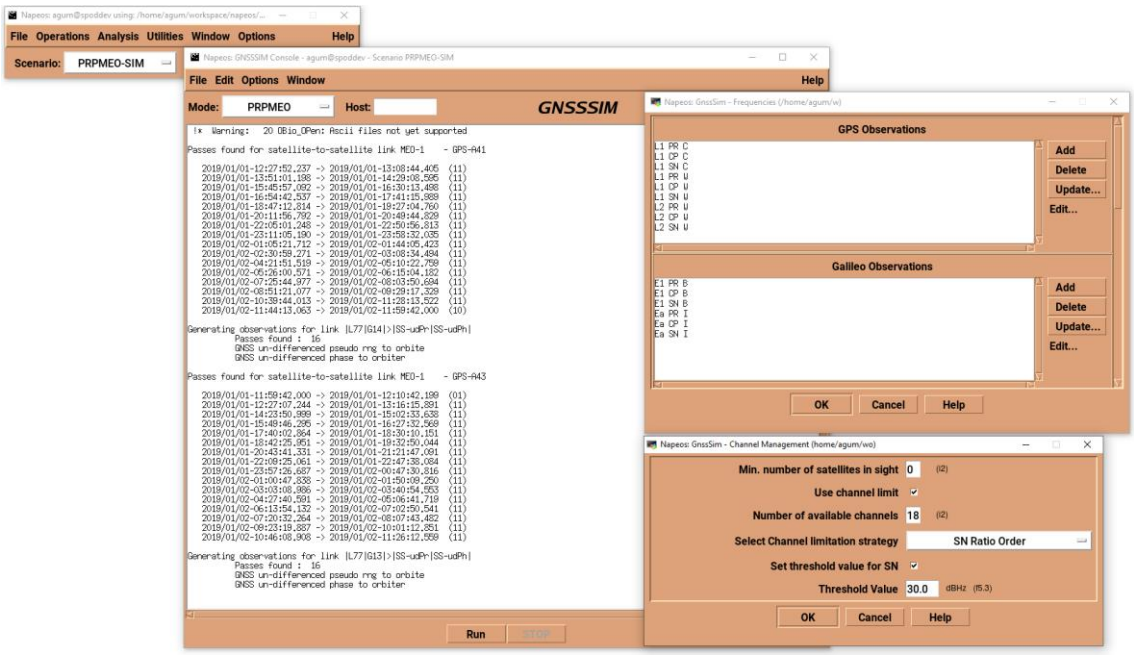

Figure B 1. Screenshot of NAPEOS graphical user interface showing different passes of GPS satellites in sight with MEO-1 satellite

The program *Propag* is an orbit propagator. Given the initial conditions either in Keplerian or Cartesian coordinates and a time range, the program generates the corresponding orbit. In this

program, the different perturbations that model the motion of the satellite in orbit may be enabled or disabled. Moreover, the level of complexity of such perturbations can also be modified from their predetermined values (for instance order and degree of the gravity model).

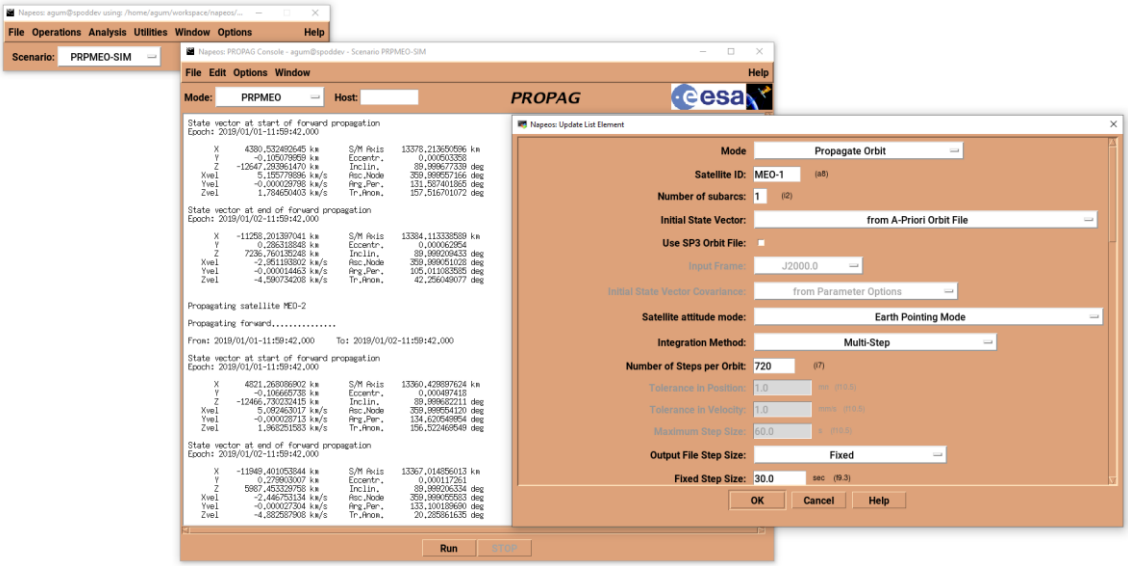

Figure B 2. Screenshot of the NAPEOS graphical user interface showing start of forward and backward state vectors of MEO-1 satellite

The program TrackSim is a very powerful generator of a very wide spectrum of signals. In this thesis work it has been used to generate the inter-satellite link ranging observations between the satellites. To do so, the considered-as-real orbits of both user satellites (generated by means of propagation) were needed as input to obtain the real true geometric range between the satellites. Then, white Gaussian noise was included to the set of measurements to make them more realistic. The order of magnitude of the inserted noise will determine the accuracy level of the measurements and can be varied depending on the nature of the technique assumed to generate the observations in reality.

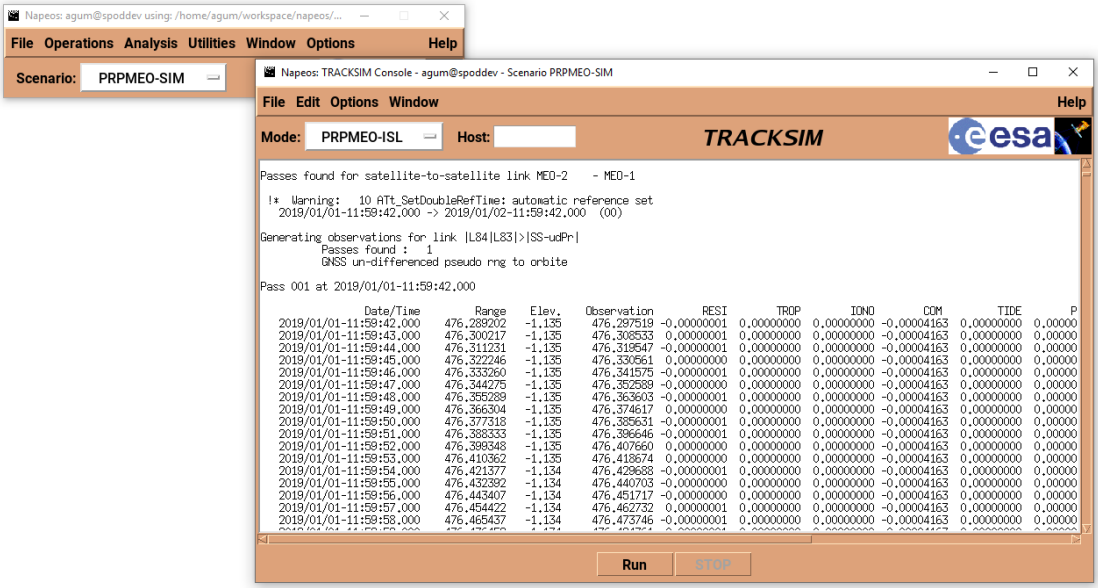

Figure B 3. Screenshot of the NAPEOS graphical user interface showing the generation of ISL observations between the MEO satellites

The tool *ClockGen* allows the user to generate clock biases, that can be used later to add this contribution to the GNSS or ISL observables. The main clock parameters to be determined are: stability (Allan deviation), initial offset drift and frequency drift.

Processing tools

GnssObs is the GNSS pre-processing module of NAPEOS. Its main function is to read the GNSS measurements from a RINEX file and process them so that they can be used later on by the main POD block. The preprocessing consists of outlier elimination, identify cycle slips and calculate preliminary clocks of the receiver.

The main POD program is known as *Bahn* and it is in charge of solving the normal equations of the least squares that yields the orbit result that best fits the observations. The settings to be configured in this program are mainly related to the different weights given to the observations and state variables and also the number of fixed iterations that the normal equations have to be solved.

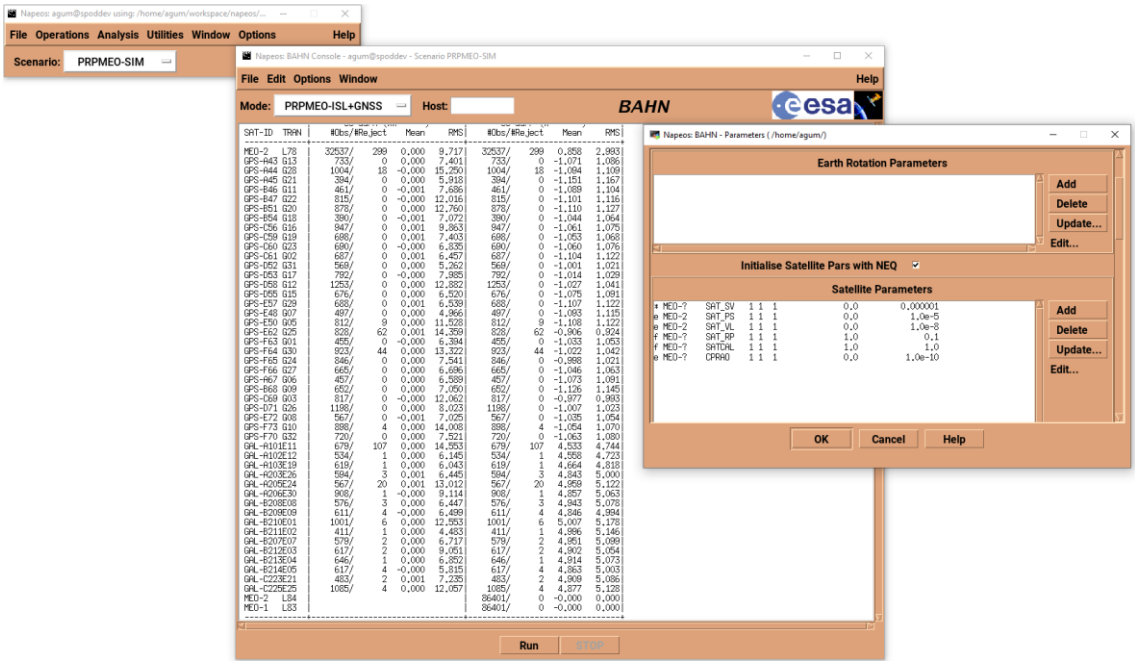

Figure B 4.Screenshot of the NAPEOS graphical user interface showing GNSS and ISL residuals from a relative POD process (MEO-1 fixed orbit, MEO-2 re-estimated orbit)

Comparison tools

In this block, both a clock and orbit comparison programs are found: *ClockComp* and *OrbComp*. Their functioning is very similar even though they actually compare two completely different things. Indeed, both programs require two different input files: the one generated by means of the POD process and a reference one (that is considered as reality). Therefore, the programs are in charge of making an evaluation of how the results (both clock and orbit) obtained in the POD process are similar to the reference ones. To do so, in both cases an output file is generated in which an extended analysis is presented. When running *OrbComp* a set of residuals are generated in the along-track, cross-track and radial components at all epochs for which the state has been propagated. Furthermore, a residuals statistic analysis from the whole arc is also provided to get an understanding of the general fit of the estimated orbit by means of POD with respect to the reference ideal one. *ClockComp* compares two different sets of clock biases from RINEX files. As in *OrbComp*, the comparison is computed per epoch.

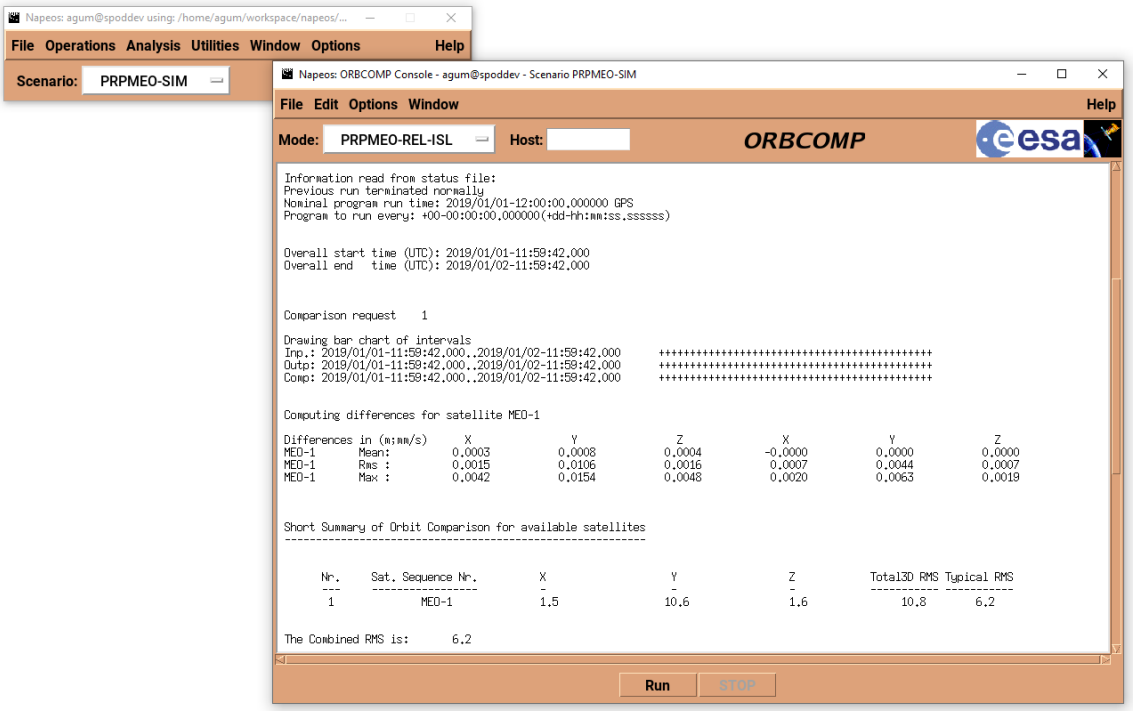

Figure B 5. Screenshot of NAPEOS graphical user interface showing the comparison of relative accuracy after processing the ISL observations